Improved Aggregation Techniques for Electromagnetic Transient Simulation of Wind Farms Considering Windspeed Variability

by

Iman Kaffashan

A Thesis submitted to the Faculty of Graduate Studies of
The University of Manitoba
in partial fulfilment of the requirements of the degree of

DOCTOR OF PHILOSOPHY

Department of Electrical and Computer Engineering
University of Manitoba
Winnipeg

Abstract

A foreseeable relatively high wind power penetration of global electricity demand will be reached in the near future. This research aims to improve aggregation modeling techniques for large wind farms considering the effect of local windspeed variations.

A new structurally complete dynamic model of a doubly-fed induction generator (DFIG) consisting of an induction machine, a back to back converter, and a step-up transformer are developed in a compact state-space form. A structure-preserving aggregation method to select the model's parameters so that the major collective dynamic characteristics of a group of DFIGs is closely approximated. The proposed aggregation method maintains the same steady-state results compared with the original unreduced model. It also preserves the major collective dynamic responses of the clustered DFIGs. A particular three-winding transformer model with current magnifying functions is developed to realize the DFIGs aggregation for Electromagnetic Transient (EMT) simulations.

Furthermore, the impact of the wake effect and varying wind speed within a wind farm on the aggregated model is investigated. Although complex models can estimate and simulate wind interaction with high accuracy, a simpler model is needed for system level simulations. First, Jensen's model is used to estimate the local windspeeds at each generator location from the ambient windspeed. Next, the aggregation algorithm generates a single representative windspeed for a cluster of generators for use in the DFIG dynamic model.

The mechanism responsible for loss of synchronization following ac faults for a DFIG is identified in the thesis. A dq frame theoretical model for the DFIG and its phase locked

loop (PLL) is developed which identifies positive and negative feedback mechanisms involved in synchronization. This is combined with a large signal plot of the synchronizing signal (proportional to measured q axis voltage V_{mq}) and a signal dependent on the PLL's output phase angle. The plot shows the largest allowable swing for V_{mq} before a point of no-return is reached. A 'stability indicator index' is introduced to indicate the likelihood of the system to experience synchronization failure.

Next, a detailed more realistic model of the DFIG is simulated on an EMT simulator (PSCAD) to show the impacts of PLL parameters and DFIG rotor speed on the grid synchronizing stability of DFIG for a remote and 3-phase fault applied to the point of common coupling (PCC). It is shown that decreasing the rotor side converter PLL integration gain or increasing/decreasing rotor speed can help increase the stability degree of wind turbine.

Use of Copyright Material

I would like to acknowledge the use of the following publications in the preparation of this thesis.

©2022 IEEE. Reprinted, with permission, from Wei Li, Iman Kaffashan, Aniruddha M. Gole and Yi Zhang, "Structure Preserving Aggregation Method for Doubly-Fed Induction Generators in Wind Power Conversion," in IEEE Transactions on Energy Conversion, vol. 37, no. 2, pp. 935-946, June 2022, doi: 10.1109/TEC.2021.3126571.

©2019 IEEE. Reprinted, with permission, from W. Li, A. M. Gole, M. K. Das and I. Kaffashan, "Research on Wind Farms Aggregation Method for Electromagnetic Simulation Based on FDNE," 2019 IEEE PES Innovative Smart Grid Technologies Europe (ISGT-Europe), Bucharest, Romania, 2019, pp. 1-5, doi: 10.1109/ISGTEurope.2019.8905666.

©2024 IEEE. Reprinted, with permission, from I. Kaffashan, W. Li, A. M. Gole, "The Loss of Synchronization Mechanism for Doubly-fed Induction Generator Integration to Weak Networks" (Accepted for 2024 IEEE Power & Energy Society General Meeting).

In reference to IEEE copyrighted material, which is used with permission in this thesis, the IEEE does not endorse any of University of Manitoba's products or services. Internal or personal use of this material is permitted. If interested in reprinting/republishing IEEE copyrighted material for advertising or promotional purposes or for creating new collective

Acknowledgments

I would like to extend my deepest gratitude to my supervisor, Prof. Ani Gole, for his invaluable guidance, support, and encouragement throughout my research and the preparation of this thesis. His insights have been instrumental in shaping my work.

I am also grateful to my university colleague, Dr. Wei Li, and my advisory committee members, Prof. Joydeep Mitra, Prof. Carl Ho, and Prof. Matt Khoshdarregi, for their thoughtful feedback and constructive comments, which significantly contributed to the improvement of my research.

My sincere appreciation extends to my managers and colleagues at PSC Consulting and Stantec/Teshmont, with special acknowledgment to Dr. Jenny Zhou, whose support and encouragement have greatly influenced my professional journey.

A special thanks goes to my beloved wife, Reyhaneh Ababzadeh, whose support and encouragement have been my constant source of strength and inspiration. Her love and belief in me have illuminated my path to success. I would also like to express my heartfelt thanks to my son, Ilya Mahdi, whose joyful presence and beautiful smile have been a source of energy and motivation.

I am deeply thankful to my entire family, particularly my mother, Sima, my father, Mohammad, my mother-in-law, Fereshteh, and my father-in-law, Amir, for their enduring support throughout these years.

Contents

List of Tables

List of Figures

List of Symbols

Z	Impedance
Y	Admittance
ω	Angular Frequency (rad/s)
f	Frequency (Hz)
$A_{mi}, \omega_i, \alpha_{mi}$	Amplitude, frequency and angle modulation indices of GSC
$A_{mo}, \omega_o, \alpha_{mo}$	Amplitude, frequency and angle modulation indices of RSC
C, V_{dc}	Back-to-back converter dc link capacitor and its voltage
i_{di}, i_{qi}	GSC d and q-axis component current
i_{dr}, i_{qr}	Rotor d and q-axis component current
i_{ds}, i_{qs}	Stator d and q-axis component current
L_{ls}, L_{lr}, L_m	Stator leakage, rotor leakage and mutual inductances of induction machine
L_{sg}, R_{sg}	GSC side inductor and resistor
L_{sr}, R_{sr}	RSC side inductor and resistor
r_r, r_s	Rotor and stator resistances of induction machine
R, X	equivalent impedance resistance and reactance
T_m, T_e	Prime mover and electromagnetic torque
V_H, V_L, V_T	Three-winding transformer high, low and tertiary winding rating voltage
$V_0,\ \theta_r$	PCC bus voltage magnitude and angle
ω_r, ω_s	Rotor and synchronous angular velocity
$\lambda_{dr}, \lambda_{qr}$	Rotor d and q-axis component flux linkage
$\lambda_{ds}, \lambda_{qs}$	Stator d and q-axis component flux linkage

List of Acronyms

EMT	Electromagnetic Transient
WTG	Wind Turbine Generator
WF	Wind Farm
DFIG	Doubly Fed Induction Generator
PMSG	Permanent Magnet Synchronous Generator
PCC	Point of Common Coupling
RSC	Rotor-Side Converter
GSC	Grid-Side Converter
PLL	Phase-Locked Loop
SS	Small Signal
SCR	Short Circuit Ratio

Chapter 1

Introduction

1.1 Background and Literature Review

The utilization of wind power is rapidly increasing worldwide and is projected to meet a substantial portion of global electricity demand in the near future [1]. The two most widely used wind energy conversion systems worldwide have been the doubly-fed induction generator (DFIG) and the permanent magnet synchronous generator (PMSG) [2]. The DFIG system, which operates at variable speeds, has higher efficiency compared to fixed-speed systems and has become the most widely utilized in large-scale wind farms due to its various benefits, such as improved energy conversion efficiency, larger unit capacity, and reduced mechanical stress from wind gusts [3]-[6]. The main drawback is the need for a power converter interface to control the rotor speed in order to capture the maximum power from the wind. The converter adds cost and complexity to the energy conversion system [7]. Despite this, the power converter decouples the induction machine from the grid, enabling control of grid-side active and reactive power [8]. The converter only needs to process approximately 30% of the generator's full rated power, referred to as slip power in the rotor circuits [9]. With hundreds of wind turbine generators in a large-scale wind farm, the system's order can reach thousands, making wind farm simulations computationally impractical when the host power grid is also very large [10]. Therefore, efficient and accurate aggregation is crucial to make the simulation tractable.

To study the collective impact of wind farms on the power system, wind farms can be viewed as an external system and the remainder of the power system as the internal system [11]. The size of the external system can be reduced through aggregation. One of the most commonly used reduction methods in traditional ac networks is the coherency aggregation-based approach [12]-[14], which groups synchronous generators with synchronized rotors into a single generator. However, the term "coherency" is less meaningful for wind turbine power conversion system, since the induction machine is an asynchronous machine and can have different rotational speeds compared to other generators in the network [15]. A single-machine wind farm aggregation method (also called FAM in other references see page 56), where it is assumed that the entire wind farm operates at a single wind speed and all generators have the same power output, has been reported in literature [16]-[18]. This method, however, fails to account for wind farm wake effects and the differences in individual wind turbine generators (WTGs), leading to inaccuracies when wind farms are located over a large area [19]. To overcome these drawbacks, the multi-machine method has been proposed [20]-[23], where WTGs within a wind farm are grouped into different clusters based on similarities in operating conditions and represented by an equivalent model as a coherent group [24]. It is getting more and more attention from industries.

A clustering algorithm for DFIG-based wind turbines is introduced in [82], and [83] presents a method for selecting key parameters based on sensitivity indices while considering crowbar actions. However, these approaches overlook the capacity limits of DFIG-based wind turbines and the accurate representation of collector networks, leading to significant errors in loss and reactive power flows. Reference [84] and [85] propose a wind speed combination model and an analytical expressions-based model, respectively, to characterize low voltage ride through (LVRT) behavior, particularly during voltage sags. Nevertheless, these methods do not account for wind direction and wake effects, critical aspects for developing an accurate equivalent generic dynamic model of a large wind farm [81].

Despite their popularity in literature, the current aggregation methods have numerous disadvantages. As input wind speed of each turbine is continuously changing within a wind farm, the composition of the coherent group could change [25]. Therefore, the aggregated results and the original unreduced model do not match very well for the transient process.

This research aims to develop a computationally fast aggregation model of a wind farm considering wake effect which cause different input wind speed for each turbine and use that model in large network studies for EMT simulation analysis.

1.2 Research Motivation

Nowadays, the presence of large wind farms and growing dependence on wind energy raises concerns of reliability and security of power supply in the power system. The complexity of the generation schemes which also include significant number of power-electronic converter arrangements in renewable energy-based generation, demands the use of electromagnetic transients (EMT) simulations. However, performing EMT simulations, considering the detailed model of wind turbines, is impractical due to the high calculation burden. In fact, in several instances, the EMT algorithm is used in real-time simulation makes the problem even more serious. Larger wind farms are anticipated to encompass numerous wind turbines, which would result in excessively long simulation times if each turbine were to be individually modeled. One of the measures to solve this problem can be using aggregation modeling that can reduce the order and complexity of the wind farm model. By employing this technique, it enables the quick simulation of wind condition variations within a wind farm and reduces the calculation process for the instantaneous output power and voltage response. However, within a large wind farm, wind turbines experiencing varying wind speeds due to wake effects [39], thus yielding disparate power outputs.

The lack of aggregation model of a wind farm for reducing the order of system for real-time simulation purposes that can have an accurate transient response when implemented in an EMT-type simulator is the main motivation behind this research. In addition, considering the effect of turbines on the speed of other turbines due to the wake effect and wind speed variation within a wind farm is investigated in this work.

1.3 Desired Outcomes and Objectives

Simplification of wind farms is an area of considerable interest. The wind generation modeling group of the Western Electricity Coordinating Council (WECC) has published a guide on wind power plant (WPP) modeling [42]. The National Renewable Energy Laboratory (NREL) of the USA developed a method to represent a WPP by an equivalent model with an equivalent collector system [19], [21]. An exhaustive simulation study was performed to validate the adequacy of the equivalencing method promoted by NREL for modeling WPP using single- and multiple-machine equivalents. The results suggest that the aggregation technique is adequate for load flow, stability, and electromagnetic transient studies with limitations [20]. Some other literature put forward a reduced model of wind farms, which captures the main dynamics of the original higher order system. The applicability and effectiveness of different order reduction methods are contrasted [10], [52]. However, the majority of previous research on aggregation model development has focused on the dynamics of the wind farm without considering wind speed variation and wake effects within a wind farm. Wind farms are typically situated across a very wide area, and considering the same wind speed for all wind turbines is not accurate due to the fact that wind speed is continuously changing stochastically. Such complexity may imply excessive computational requirements. The detailed model of a wind farm with hundred turbines implemented in EMT-based software can take an excessively long simulation time to execute which may be impractical. The problem is even more severe on a real-time simulation. Therefore, a new aggregation method is required that allows taking in to account each turbine’s input wind speed within a wind farm while decreasing the computational burden for EMT-type simulations. The main objectives and motivation of this research are listed below:

a) Development of a dynamic model for a wind turbine which allows applying different wind speeds and includes the representation of the electrical and mechanical behavior.

b) Development of an aggregation method to find the equivalence model of wind farm while maintaining acceptable accuracy considering different wind speed for each turbine within a wind farm.

   It should be noted that the model is not intended for designing the wind turbine or generator. Rather it is an aggregated representation that permits the study of how the windfarm interacts with the external network, which is modelled on an EMT program. Example applications could involve performance under network faults, power supply into the network as affected by wake conditions and wind speed changes, and oscillation between other elements in the network and the windfarm.

c) Validation of the reduced-order model comparing its results with a detailed EMT model of the unreduced system.

d) Investigating the performance of aggregated model for various conditions including: 1- Under changing input wind speeds, 2- With non-identical wind turbines, 3- With different loadings of individual wind turbine, 4- With a large wind farm to compare computational saving.

e) Investigating the accuracy of existing models for calculating wake effect considering real case data.

f) Development of a dq frame theoretical model for the DFIG and its phase locked loop (PLL) which identifies positive and negative feedback mechanisms involved in synchronization.

g) Investigation into the impacts of PLL parameters and DFIG rotor speed on the grid synchronizing stability of DFIG for a short circuit fault applied to the point of common coupling (PCC). A 'stability indicator index' introduced to show the likelihood of a system including a DFIG to experience synchronization failure.

1.4 Thesis Organization

This thesis consists of six chapters. After the introduction in Chapter 1, Chapter 2 discusses the findings of the literature survey on wake effect, mathematical formulations, and modeling approaches for simulation. In Chapter 3, the state-space model of a DFIG is discussed, and a complete model of a DFIG using a combination of components is proposed. The new aggregation model for a wind farm is developed in Chapter 4, and the accuracy of the model is investigated against a time-domain model using EMT simulation is developed. Chapter 5 describes the loss of synchronization mechanism for a DFIG, and proposes an improved method for achieving robustness of stability, in DFIG connected to weak ac networks. Chapter 6 outlines the contributions of the thesis, reaches conclusions, and provides suggestions for future research.

Chapter 2

Wind Speed Distribution on the Turbine-generators in a Wind Farm

2.1 Introduction

This chapter discusses variable wind speed, gusts and wake within a wind farm. It will be followed up with different models to consider the wake effect. Then, an appropriate model will be introduced, and a comparison will be performed between the result from a real wind farm and calculated results based on the selected model.

2.2 Wake Phenomenon

The wake effect refers to the phenomenon where the aerodynamic wake generated by one wind turbine affects the performance of neighboring turbines in a wind farm. When wind flows through a wind farm, the first turbine in the direction of the wind creates a wake region behind it, characterized by a decrease in wind speed and increased turbulence. This wake region can extend for several rotor diameters downstream, which means for subsequent turbines in the same wind farm located in the wake of a leading turbine, they experience reduced wind speeds compared to a freestream condition.

The principle of energy conservation states that energy cannot be created or destroyed, only transformed. The wake effect is primarily caused by two factors: the extraction of kinetic energy by the turbine blades and the physical obstruction of the turbine tower and blades. As the blades rotate and capture energy from the wind, they slow down the wind speed in their vicinity, creating an area of lower pressure immediately behind the turbine. As the wake propagates downstream, the slower-moving air mixes with the surrounding wind, causing a decrease in wind speed and changes in wind direction. This can have significant effects on the performance and efficiency of downstream wind turbines in the same wind farm, which is referred to as the wake.

The wake effect can result in reduced power output and increased fatigue on the downstream turbines. Turbines positioned in the wake of others experience lower wind speeds, which leads to decreased energy generation. This wake can be seen in Figure 2-1 [26].

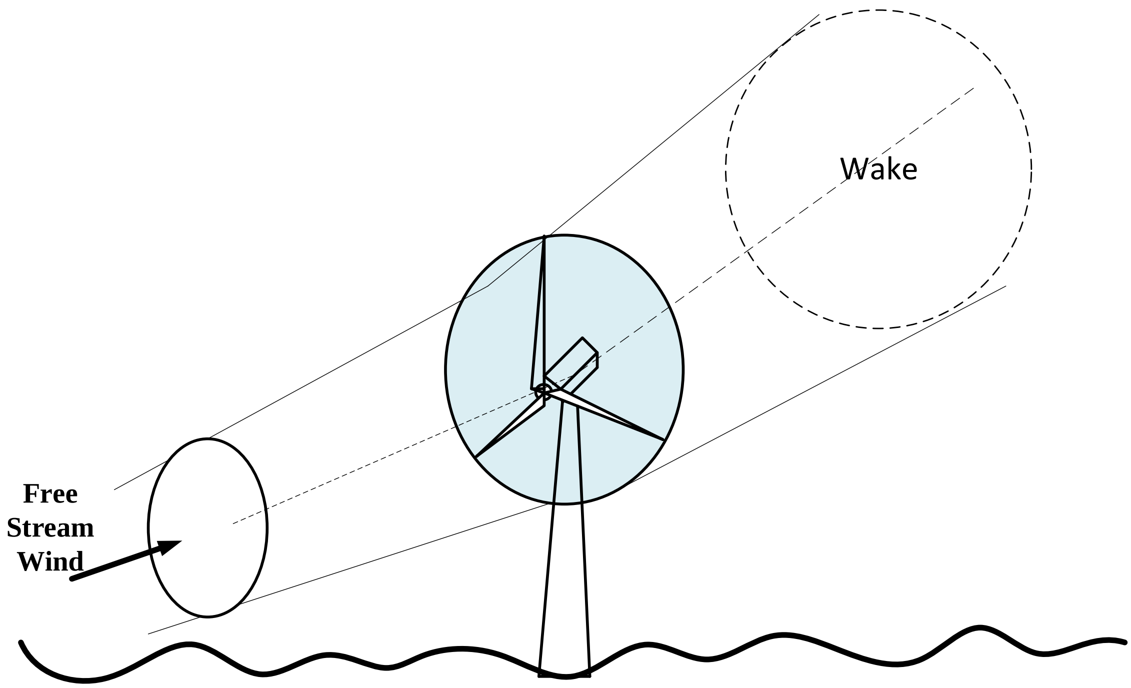

Figure 2-1 Wake Behind a Wind Turbine

The wake affected region of the wind, known as the stream tube, expands behind a wind turbine as a result of decreased wind speed and static pressure [26]. The wake has two components: i) near-wake region and ii) far-wake region. The near wake region in a wind farm refers to the immediate region (i.e., about few meters downstream) behind a wind turbine, demands a comprehensive model of the rotor [27], [28]. In the near wake region, the flow is highly turbulent and characterized by intense mixing of air. The vortices generated by the wind turbine blades are relatively large and irregular. This turbulence can have a significant impact on the performance of downstream turbines in the same wind farm. The presence of the near wake can cause reduced wind speeds, increased turbulence, and uneven wind direction, which can affect the efficiency and output of downstream turbines. The far-wake region is the area of interest when examining the impact of wind turbines when they are placed in close proximity, such as in wind farms. The far wake region in a wind farm refers to the region that extends further downstream from the wind turbine, away from the immediate wake disturbance. As the flow moves away from the turbine, the vortices in the near wake gradually dissipate, and the flow becomes more organized. In this thesis, the far-wake region is the focus, where the flow tends to become more uniform and less turbulent compared to the near wake region. If the flow of the wake is not obstructed, the stream tube will continue to expand far downstream, and the wake will eventually revert back to free-stream wind conditions.

As illustrated in Figure 2-2, there are two groups for far wake models: 1) Kinematic wake models 2) Field and wake edded turbulence models [29], [30].

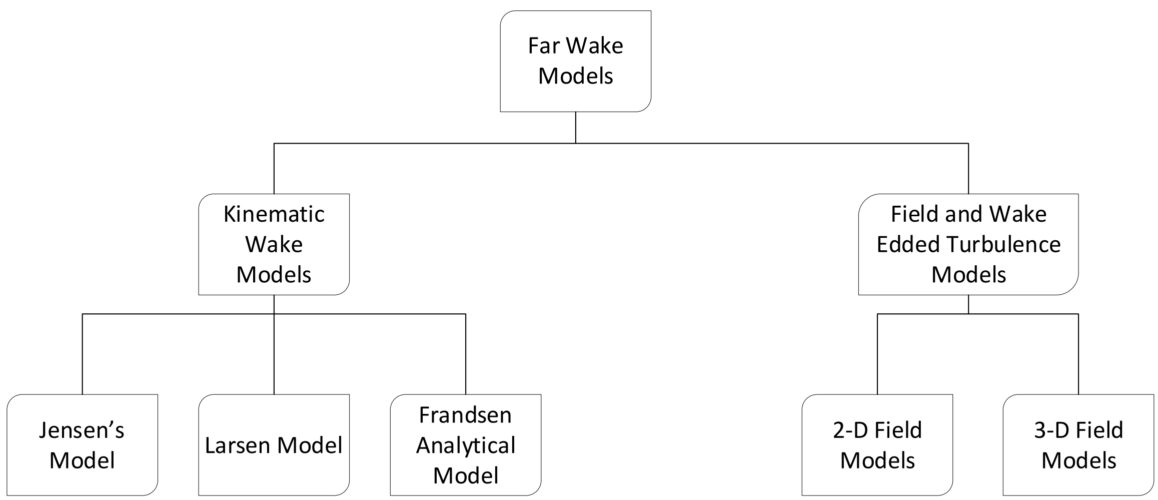

Figure 2-2 Far Wake Models

Wind farm operators use existing wake models to understand how the wake affects power production. However, these models typically provide fixed outputs for a specific wind condition, ignoring the dynamic nature of wind flow within the wind farm. The interaction between the wind and turbines leads to changes in wind speed and turbulence within the wake. While some models account for the reduced wind speed, they often neglect the turbulent nature of the flow, which can influence the power output of the turbines.

Other methods of simulation such as Finite Element Modeling, Navier-Stokes equations, and Computational Fluid Dynamics (CFD) can be used to simulate the wind flow in a wind farm, but they are often complex and time-consuming to implement, and the results can vary greatly based on the computing power available [31]-[33].

2.3 Jensen’s Wake Model

Jensen's wake model, also known as the Jensen's Cosine model, is a widely used analytical model in wind energy that estimates the wake effect caused by a wind turbine in a wind farm. It is a simplified mathematical representation aimed at reducing input requirements and computational effort [34], [35]. Jensen's wake model assumes that the wind flow in the wake of a turbine can be represented by a cosine-shaped profile. The model considers a turbine as a point source of turbulence, and the wake is assumed to expand downstream in a conical shape. The key assumptions of the Jensen's wake model are:

1- Wake Expansion: The wake expands downstream as a conical shape, and the diameter of the wake increases with the distance from the turbine.

2- Wake Deficit: The wind speed within the wake is reduced compared to the undisturbed wind speed. The reduction in wind speed is assumed to follow a cosine-shaped profile, with the maximum deficit occurring at the centerline of the wake.

3- No Lateral Expansion: The model assumes that the wake expands only in the downstream direction, with negligible lateral spreading.

The wake is depicted as expanding linearly with distance x_0, while its dispersion exhibits a Gaussian distribution, commonly referred to as a top-hat distribution. The rate of the wake's expansion is determined by the entrainment constant (k), with values of 0.075 found for onshore sites and 0.04 for offshore sites [35]. Jensen's wake model provides a simple and computationally efficient way to estimate the impact of wake on wind turbine performance in a wind farm. However, it is important to note that the model's assumptions may not fully capture the complex wake behavior, especially in more complex wind farm layouts or under certain atmospheric conditions, where more advanced models are required. When compared to actual wake measurements, the model appears to provide accurate results. The Jensen model is widely used in software such as WAsP and WindPro for simulating wake impacts and calculating wind farm output [34], [36], [37].

2.4 Detailed Wake Effect Modeling

The impact of wake on wind turbine performance is influenced by several factors, including the incoming wind velocity and direction, as well as the arrangement of turbines within a wind farm. The spatial arrangement of turbines, including the inter-turbine distance, is crucial in determining the wake effect. To accurately model the wake effect, a comprehensive model is employed that considers the single, partially overlapped, and multiple wakes within a wind farm, taking into account important parameters such as the rotor radius, thrust coefficient, and the expansion of the stream tube [76].

2.4.1 Single Wake Model

The presence of a single wake is when the rotor of one turbine lies entirely within the shadow of another turbine, as shown in Figure 2-3. This type of wake is analyzed using Jensen's kinematic wake model. According to this model, the wake behind a single turbine expands in accordance with equation (1), which describes the relationship between the wake radius (r_w), distance (x_0), the entrainment constant (k) and the radius of the wind turbine rotor (r_0).

$$r_w = r_0 + kx_0 \tag{1}$$

Equation (2) represents the mean wind speed in the wake of a single turbine is dependent on the free-stream wind speed (u) and the thrust coefficient (C_t) of the turbine, at a distance x_0 [76].

$$v_1 = u[1 - \left(\frac{r_0}{r_0 + kx_0}\right)^2 (1 - \sqrt{1 - C_t})] \tag{2}$$

The expansion of the wake behind a wind turbine is represented in Figure 2-3.

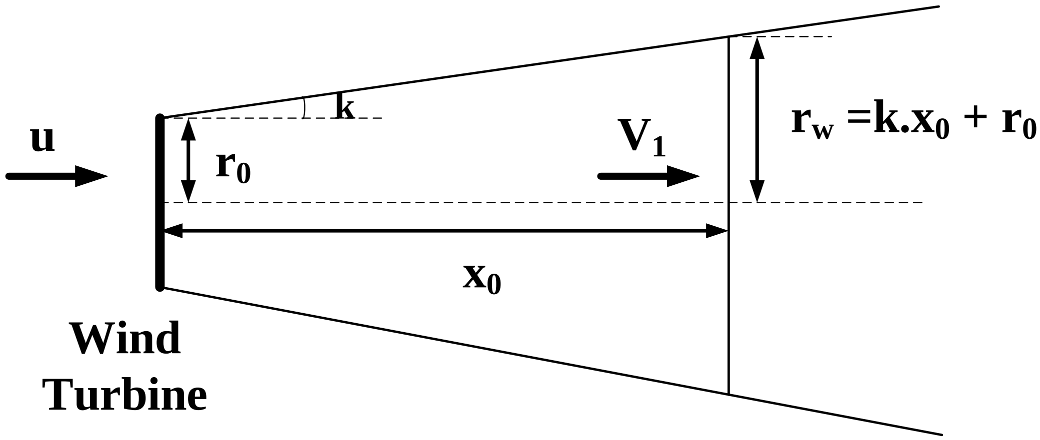

Figure 2-3 Single Wake Expansion Behind the Wind Turbine [38]

2.4.2 Partial and Multiple Wake Model

Partial wake conditions typically occur when the spacing between the turbines is relatively large, allowing for some degree of recovery and mixing of the wake before reaching the downstream turbines. The wake of the upstream turbine may not fully cover the rotor of the downstream turbine, resulting in a partial overlap of the wakes, as shown in Figure 2-4. In this scenario, only a portion of the downwind rotor is under the influence of the wake, while the rest of the rotor operates in free-stream conditions. The impact of partial wakes on the power output of the downwind turbine is more complex and less predictable than that of a single wake, as it depends on the relative position and size of the upwind turbines. To model partial wakes, more sophisticated models that take into account the interaction between the wakes of multiple turbines are required.

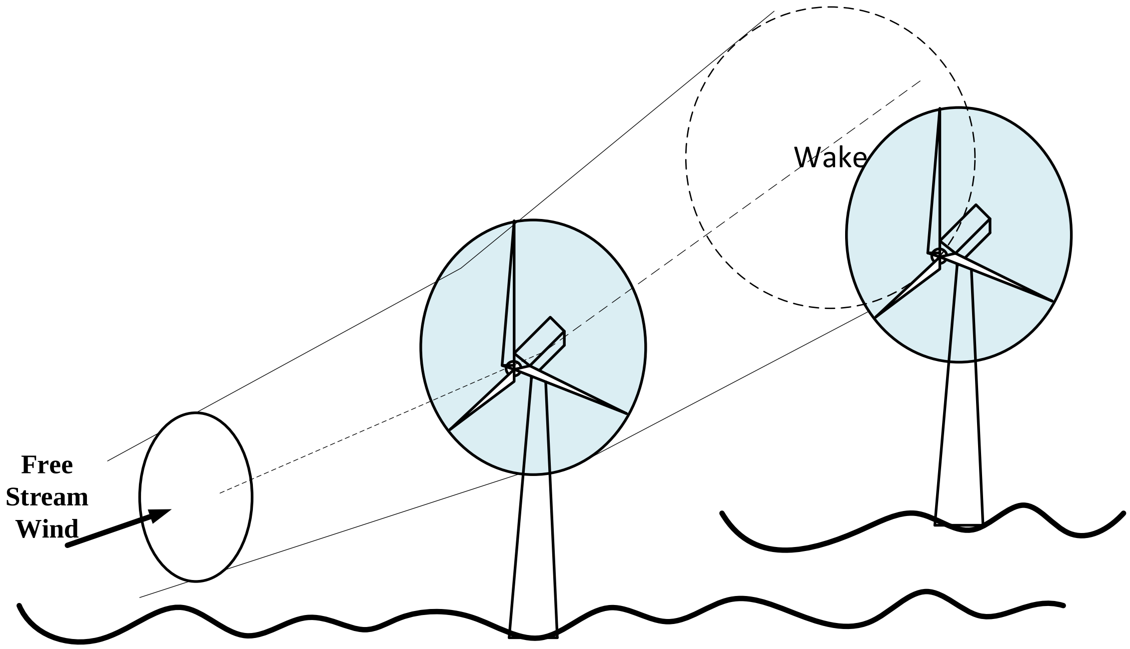

Figure 2-4 Partially Shaded Rotor Disk of a Turbine Downwind [38]

The performance of a downstream wind turbine in a wind farm can be impacted by multiple upstream wind turbines that cast shadows on it. This phenomenon is referred to as the multiple wake effect and is shown in Figure 2-5. The wind speed at a specific wind turbine (j) is influenced not just by the directly upwind turbine (i) but also by other upwind turbines such as 1, 2 and 3. This is due to the interaction of the wakes created by these turbines, as shown by the direction of the undisturbed wind speed (u) in Figure 2-5 [30].

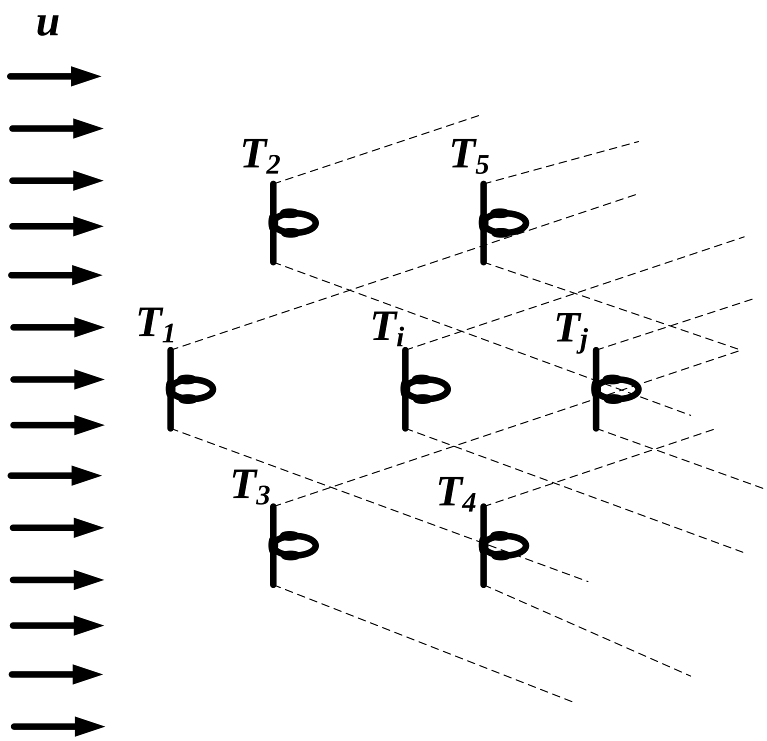

Figure 2-5 The Effect of Turbines in a Wind Farm on Each Other

To accurately model the effect of multiple wakes in a wind farm with multiple turbines, it is necessary to consider the overlap of the wakes cast by each upstream turbine on a downstream turbine. This overlap, or shadowing, is calculated by comparing the area of the shadow cone (A_{shadow}, i) of the upstream turbine to the area swept by the rotor disk (A_0) of the downstream turbine. An example of which is depicted in Figure 2-6.

There are four different shadowing scenarios, including full shadowing, nearly full shadowing, partial shadowing, and no shadowing. If the wind turbines have the same diameter, the area of the shadowed rotor disk can be determined using basic trigonometric calculations, as described in equation (3) and (4) [39].

$$A_{shadow,i} = \left[r_i(x_{ij})\right]^2 \cos^{-1}\left(\frac{L_{ij}}{r_i(x_{ij})}\right) + r_0^2 cos^{-1}\left(\frac{d_{ij} - L_{ij}}{r_i(x_{ij})}\right) - d_{ij}z_{ij} \tag{3}$$

$$v_j(x_{ij}) = v_i[1 - \sum_{i=1}^{n}\left(1 - \sqrt{1 - C_t}\right)\left(\frac{r_0}{r_i(x_{ij})}\right)^2 \frac{A_{shadow,i}}{A_0}] \tag{4}$$

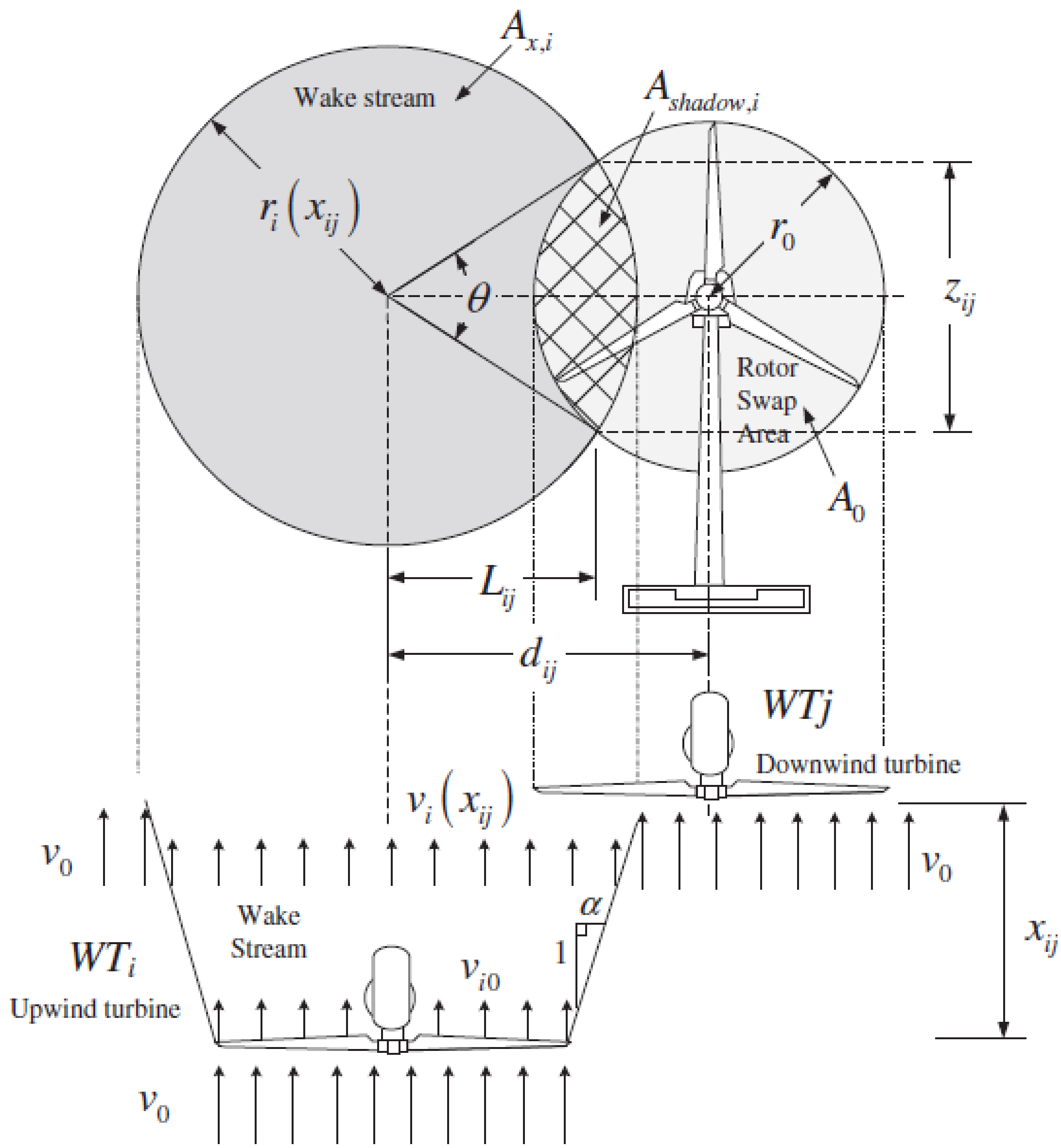

Figure 2-6 A Detailed Example of Partial Shadowing [39]

The production of energy by a downstream wind turbine can be impacted by wakes generated by multiple upstream wind turbines. This, combined with the fluctuating wind speed, makes the calculation of wind speed deficit even more complicated. This situation is depicted in Figure 2-7, which shows the impact of multiple wake interaction and wind speed variation. This illustration shows that determining the wind speed deficit in the presence of multiple wakes and varying wind speeds will require the application of both superposition and decision-making techniques to solve the issue effectively.

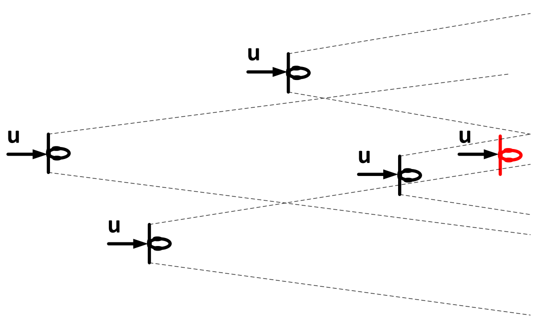

(a)

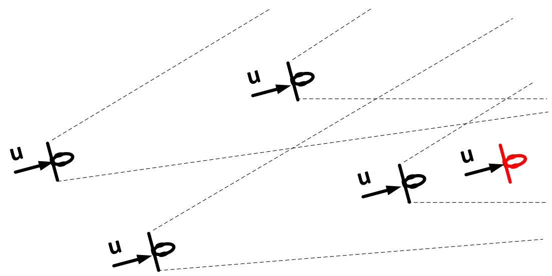

(b)

Figure 2-7 Schematic of Multiple Wakes: (a) Wind Direction from West to East. (b) Wind Direction from Southwest to Northeast

2.5 Case Study: Horns Rev 1 Wind Farm

The Horns Rev 1 is a historic offshore wind farm that was the first of its kind in the North Sea. With a capacity of 160 MW, the project was built in three stages, Horns Rev 1 being the first to be completed in 2002, followed by Horns Rev 2 in 2009, and finally Horns Rev 3 in 2019. The Horns Rev 1 segment encompassed the installation of 80 Vestas V80-2.0 MW Doubly Fed Induction Generator (DFIG) wind turbines, executed by A2SEA, a Danish provider of offshore wind farm services. The turbines were all put into operation on December 11, 2002. They are arranged in an oblique rectangle shape and spaced 560 meters apart in both horizontal and vertical directions, with 8 rows of turbines running horizontally and 10 rows running vertically [40].

2.5.1 Real Measurements from Horns Rev 1 Wind Farm

In 2005, a comprehensive dataset capturing a year's worth of data was acquired from the Horns Rev wind farm under an agreement with DONG Energy A/S. This dataset offers intricate insights, including the 10-minute average power output, nacelle position, pitch angle, and yaw misalignment for each individual wind turbine. Additionally, it provides information on wind speeds and directions, obtained from three nearby meteorological masts. The dataset covers a complete operational year, during which the park demonstrated a commendable level of availability [41].

The flow cases in the data set depict three different wind turbine spacings, which are a crucial factor in assessing the wake deficit. These spacings are determined by the layout of the wind farm and cannot be altered. As a result, three basic flow cases are established, each featuring uniform inflow that represents a long velocity fetch distance, as tabulated in Table 2-1 [41].

Table 2-1 Three Different Cases for Measurements

Case	Spacing *(m)*	Wind direction *(Degrees)*	Speed at the hub of the turbine (V_{hub}) *(m/s)*

1	$7 \times D$[1]	270	6, 8, 10
2	$9.4 \times D$	221	6, 8, 10
3	$10.4 \times D$	312	6, 8, 10

2.5.2 Horns Rev 1 Wind Farm Layout

The Horns Rev 1 wind farm is a matrix of 80 wind turbines arranged in 8 rows and 10 columns, forming a parallelogram shown in Figure 2-8. The spacing between each turbine in both the rows and columns is 560 meters (7 times the diameter of the turbine (D)). The spacing between the turbines along the southwest to northeast diagonal is 750 meters ($9.4 \times D$), and along the northwest diagonal is 840 meters ($10.4 \times D$), as indicated in Figure 2-8. Wind turbine number 7 (wt07) is the reference wind turbine which is shown in red in Figure 2-8.

[1] D is diameter of the turbine.

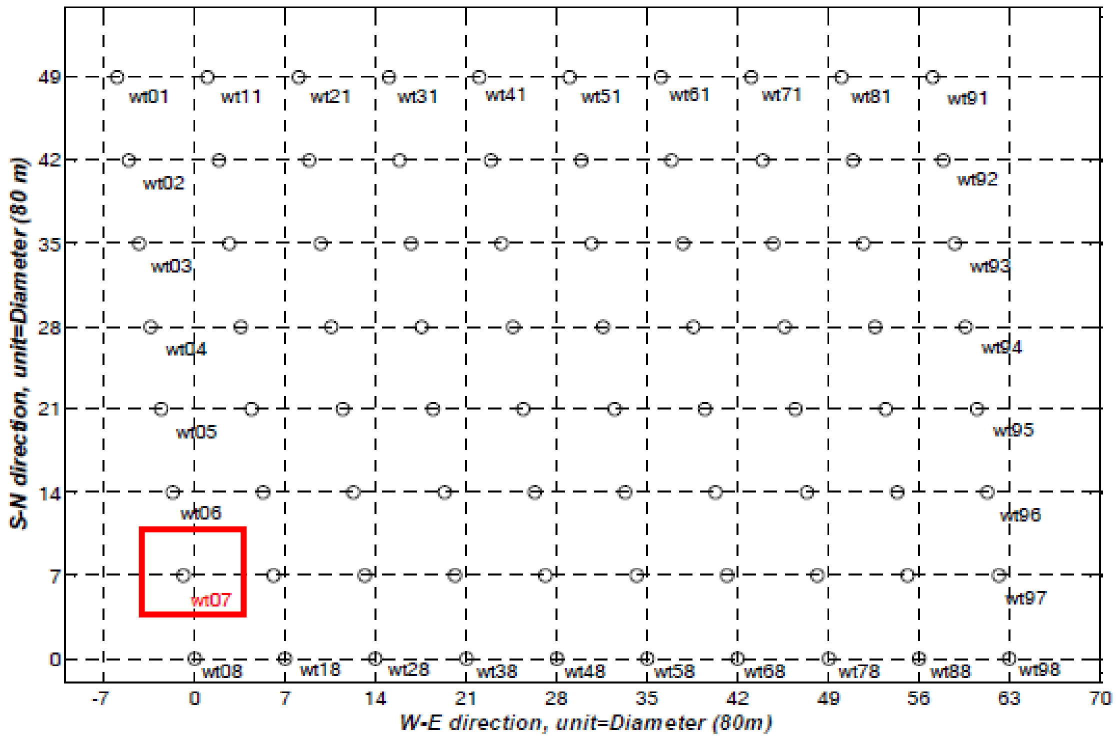

Figure 2-8 Horns Rev 1 Wind Farm Layout [41]

2.5.3 Data Screening for the Wind Farm

The Horns Rev 1 wind farm data set includes detailed information on the performance of each wind turbine, collected over the course of one full year. This comprehensive dataset offers details, including precise 10-minute average measurements such as power generation, turbine pitch angle, wind speed and direction at the nacelle, nacelle position, and the cumulative operating hours of each turbine. This invaluable dataset serves as a rich source of insights into the performance of each wind turbine, facilitating the identification and implementation of optimization strategies to enhance their efficiency and overall performance.

2.5.4 Power and Thrust Coefficient of Turbines

The power and thrust coefficient for all identical Vestas V80-2.0 MW wind turbines used in Horns Rev 1 are considered based on Table 2-2 information.

Table 2-2 Wind Turbine Power and Thrust Coefficient for Different Wind Speed [41]

Wind speed	Power *(kW)*	Thrust coefficient (C_t)
4	66.6	0.818
5	154	0.806
6	282	0.804
7	460	0.805
8	696	0.806
9	996	0.807
10	1341	0.793
11	1661	0.739
12	1866	0.709
13	1958	0.409
14	1988	0.314
15	1997	0.249
16	1999	0.202
17	2000	0.167
18	2000	0.140
19	2000	0.119
20	2000	0.102
21	2000	0.088
22	2000	0.077
23	2000	0.067

Wind speed	Power *(kW)*	Thrust coefficient *(C_t)*
24	2000	0.060

2.5.5 Flow profiles for case 1

According to Table 2-1, wind speed direction assumed for case 1 is 270 degrees. The wind speed data in the dataset is divided into different categories, or "bins," based on wind speed. For a wind speed bin at 6 m/s, there are 120 measurement periods distributed across 8 rows. This amounts to approximately 2 hours of collected data along each row, spanning a 2-degree sector. The average wind speed deficit along a row, relative to the distance between upwind and downwind turbines for each case, is depicted in Figure 2-9 and Figure 2-10. The error bars in these figures indicate the standard deviation of the mean row deficits, derived from the data collected from the 8 rows [41].

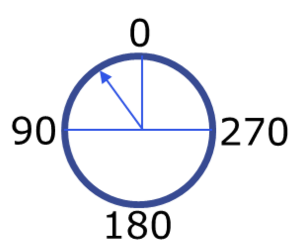

Figure 2-9 Wind Direction Angle

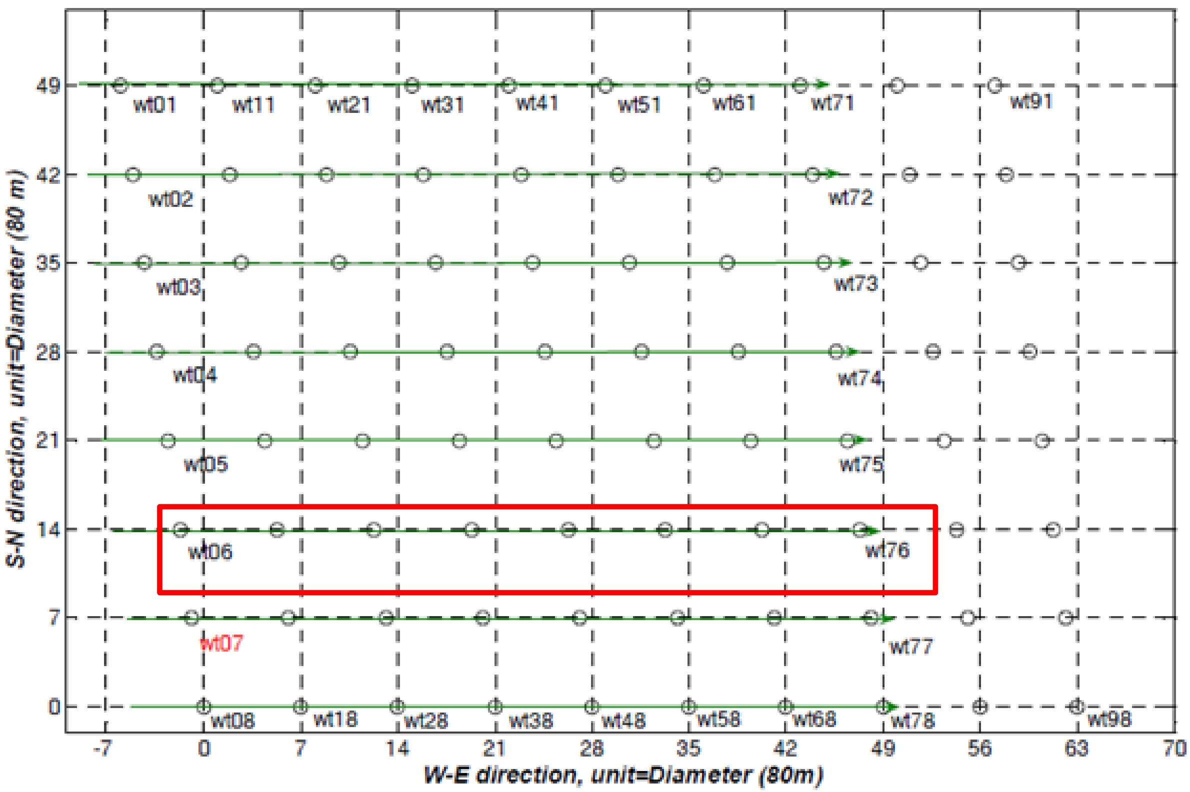

Figure 2-10 Wind Turbine Layout Considering Wind Speed Direction of 270 Degrees

In Figure 2-11, wind speed and power deficit of each turbine in row 7 including wt07, wt17, wt27, …, wt77 are illustrated. There is a significant reduction in wind speed between the wt07 and wt17 which are the first and second wind turbine facing free wind. Accordingly, the output power of the second wind turbine (wt17) will be reduced by about 32% since the output power is proportional to $(wind\ speed)^3$.

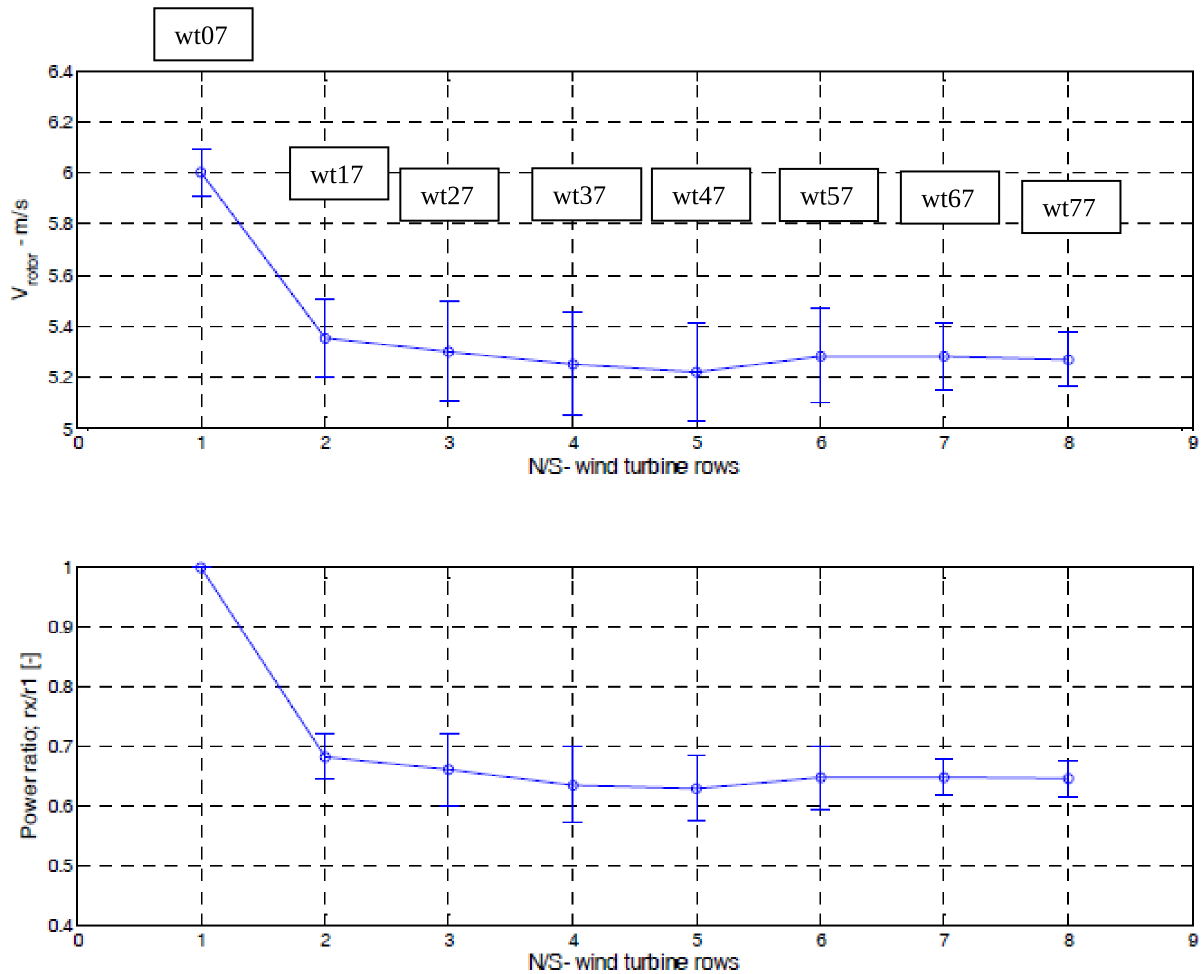

Figure 2-11 Wind Speed and Power Deficit of Wind Turbines in Row Number 7 (Wind Direction=270 and Free Wind Speed = 6 m/s) [41]

2.5.6 Flow profiles for case 2

The flow direction for case 2 is 221 degrees along rows of 5 wind turbines with $9.4 \times D$ spacing, where 5 turbines in each row are included in the wake deficit determination. The green arrows in Figure 2-12 show the wind direction [41].

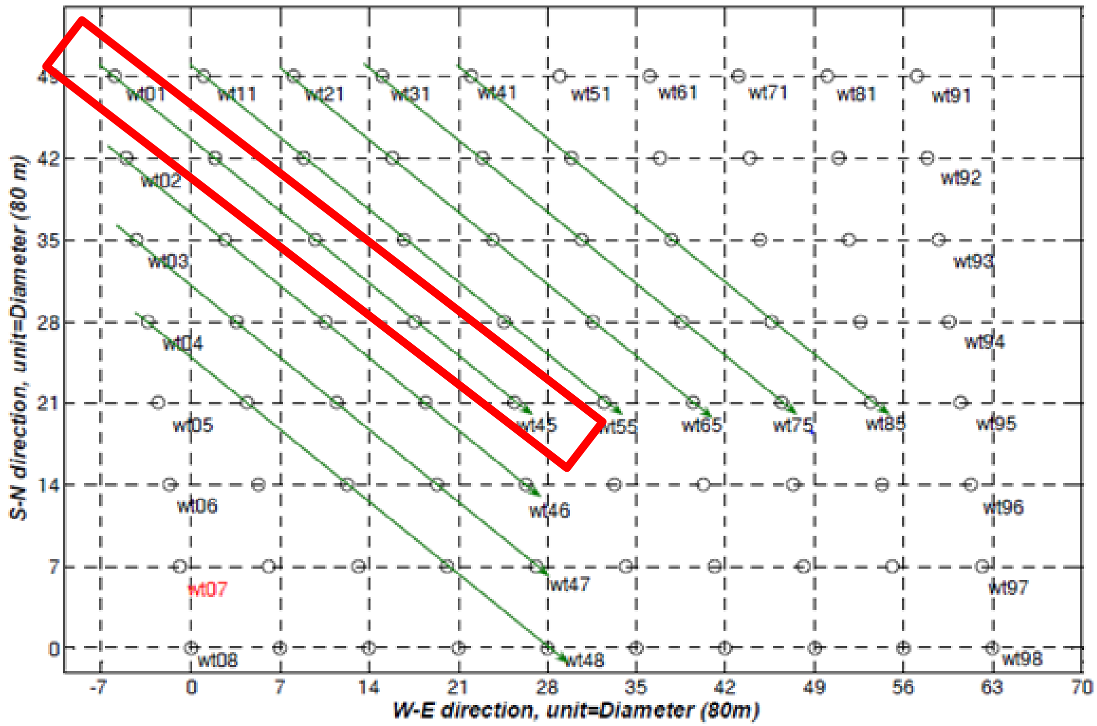

Figure 2-12 Wind Turbine Layout Considering Wind Speed Direction of 221 Degrees

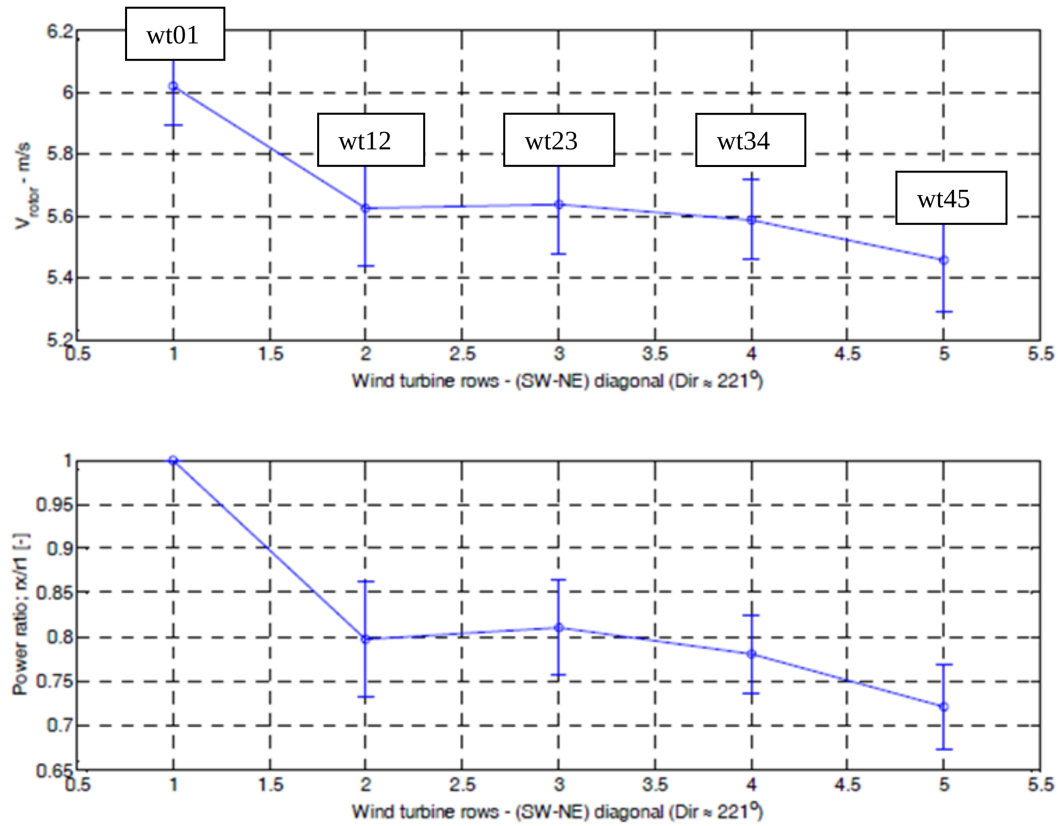

Figure 2-13 Wind Speed and Power Deficit of Wind Turbines in the Same Diagonal Row (Wind Direction=221 and Free Wind Speed = 6 m/s) [41]

2.5.7 Flow profiles for case 3

In this case, wind direction is 312 degrees with $10.4 \times D$ spacing between wind turbines. The mean wind speed deficit along a row is presented in Figure 2-15 as a function of the distance between upwind and downwind turbines [41].

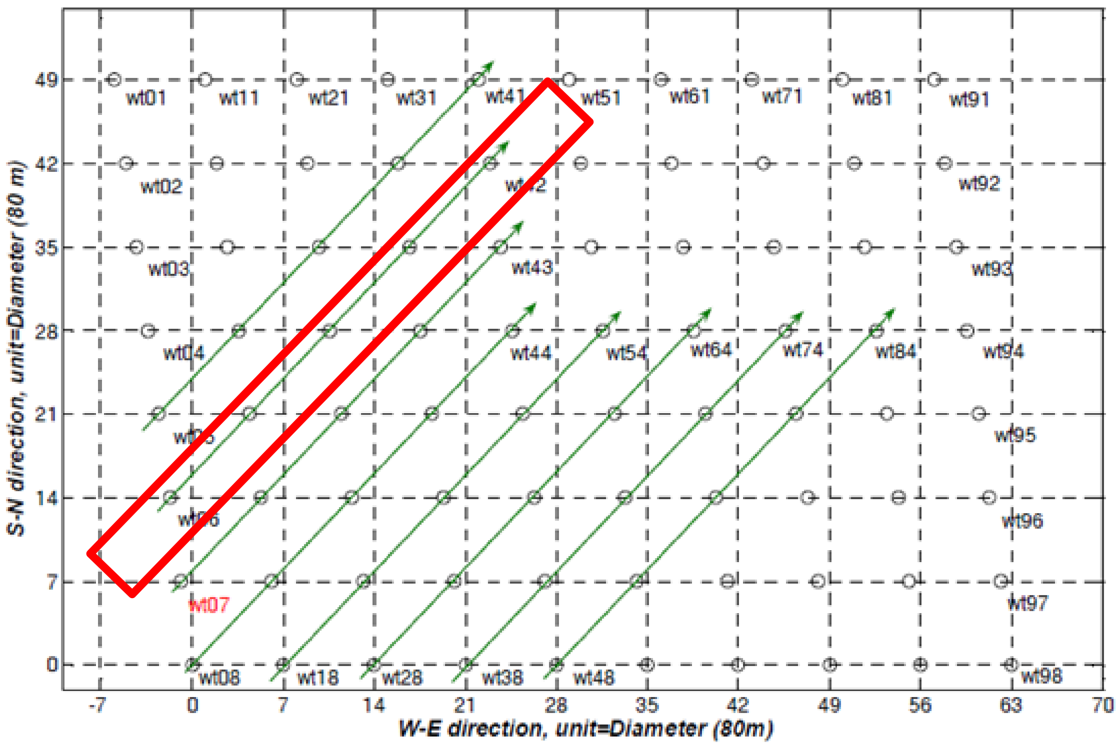

Figure 2-14 Wind Turbine Layout Considering Wind Speed Direction of 312 Degrees

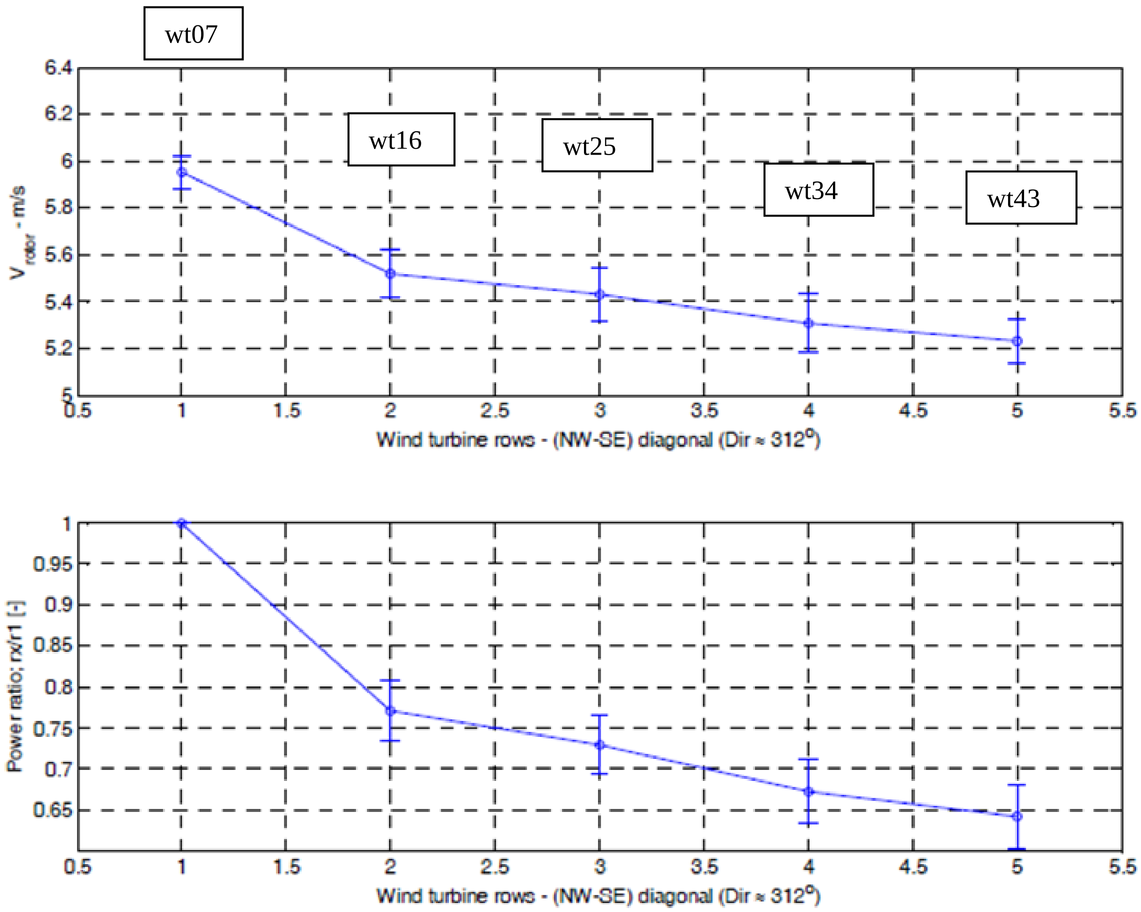

Figure 2-15 Wind Speed and Power Deficit of Wind Turbines in the Same Row (Wind Direction=312 Degrees and Free Wind Speed = 6 m/s) [41]

2.6 Comparing Real Measurements with Jensen's Model

To compare the results from Jensen's model with those from real-life data, a wind farm layout with 9 turbines was proposed. This layout is shown in Figure 2-17, with the locations of the nine turbines highlighted in the Horns Rev 1 wind farm layout in Figure 2-16. The nine turbines, named G1A, G1B, G1C, G2A, G2B, G2C, G3A, G3B, and G3C, are located at the positions of wt06, wt16, wt26, wt07, wt17, wt27, wt08, wt18, and wt28 in the Horns Rev 1 wind farm, respectively. To compare the results from Jensen's model with the real measurements from the Horns Rev 1 wind farm, wind speeds of turbines were calculated for three different cases, which were based on the three cases from the Horns Rev 1 wind park.

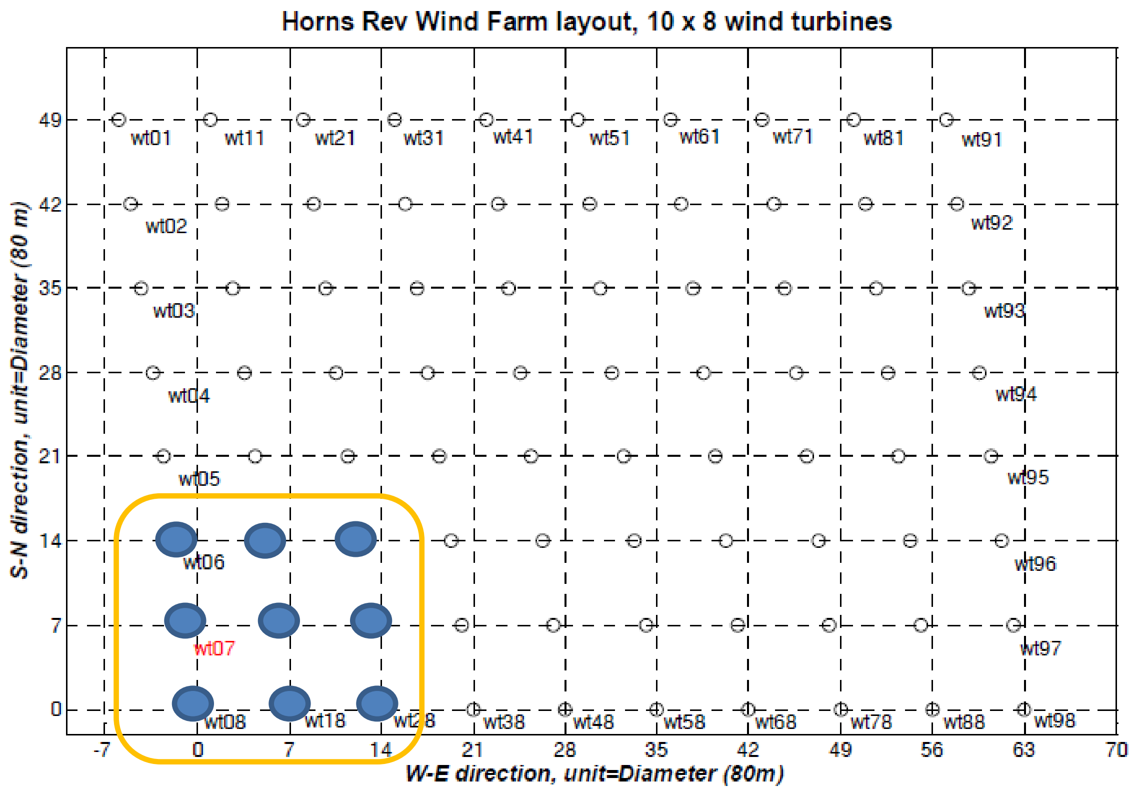

Figure 2-16 Location of 9 Turbines Considered as a Case Study to Compare Results in Horns Rev 1 Layout

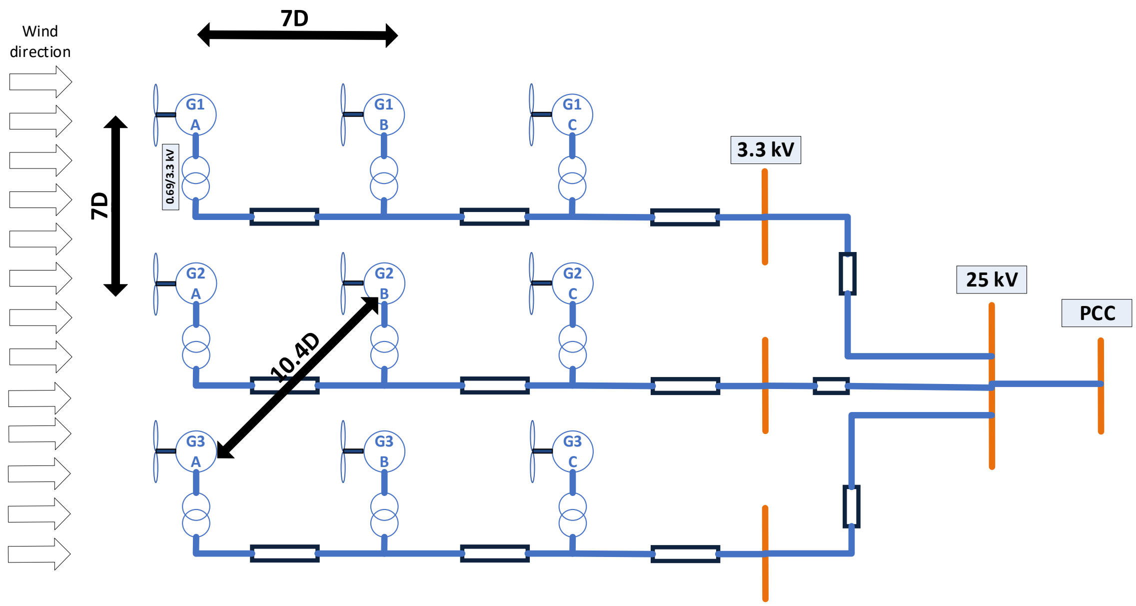

Figure 2-17 Wind Farm Layout for Case 1 with Wind Direction of 270 Degrees

Based on the wind farm layout in Figure 2-17, and considering free wind speed equal to 6 m/s, the wind speed of each turbine has been calculated by using Jensen's model. According to Table 2-3, there is about 13.5 percentage error between the value, which is calculated based on Jensen's model and the mean actual wind speed of G1B and G2B. There is not any error for G1A, G2A, and G3A as they are facing free wind directly. For G1C, G2C, and G3C, this error is 16.39%.

Table 2-3 Case 1: Wind Direction 270 Degrees ($V_0 = 6\ m/s$)

Wind Turbine	Calculated wind speed (m/s) based on Jensen's model	Mean actual wind speed (m/s) based on Horns Rev1 wind farm measurements	Percentage Error (%)
G1A	6	6	0
G1B	4.62	5.35	13.5
G1C	4.43	5.3	16.4
G2A	6	6	0
G2B	4.62	5.35	13.5

G2C	4.43	5.3	16.4
G3A	6	6	0
G3B	4.62	5.35	13.5
G3C	4.43	5.3	16.4

In Figure 2-18, the wind direction is considered as 221 degrees for case 2. As it is illustrated in Figure 2-18, wind speed of G1A, G1B, G1C, G2A, and G3A are all equal to free wind speed from outside, which is 6 m/s. The results of that are collected in Table 2-4.

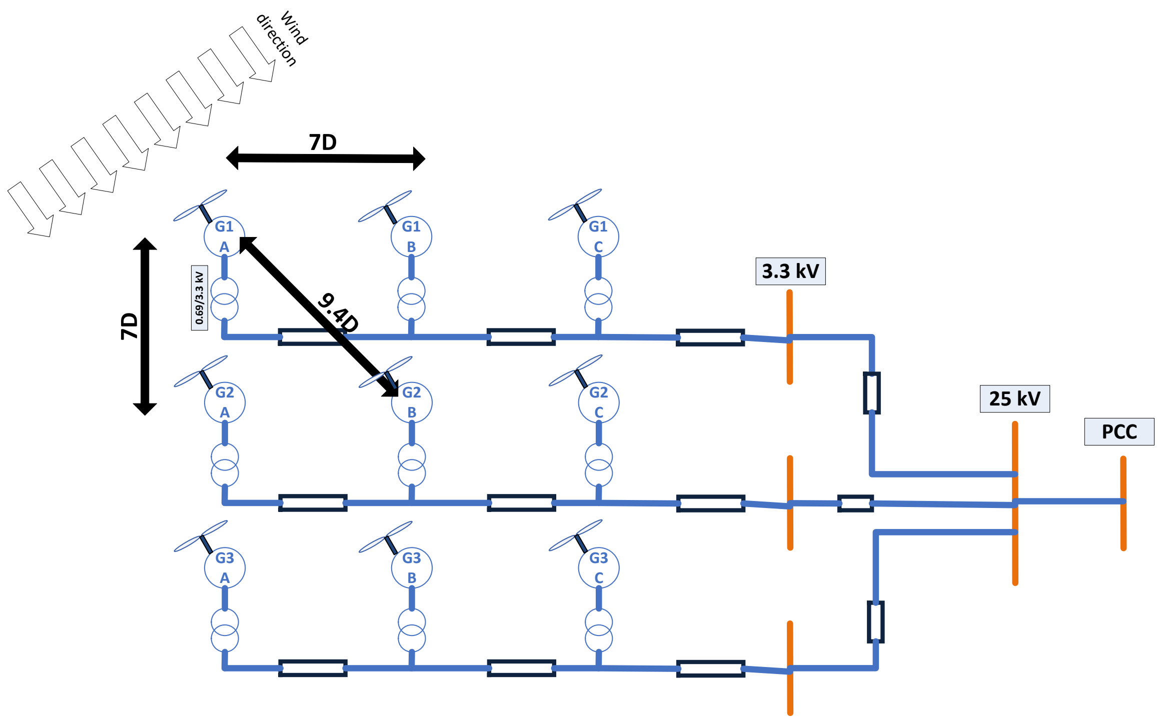

Figure 2-18 Wind Farm Layout for Case 2 with Wind Direction of 221 Degrees

Table 2-4 Case 2: Wind Direction 221 Degrees ($V_0 = 6\ m/s$)

Wind Turbine	Calculated wind speed (m/s) based on Jensen's model	Mean actual wind speed (m/s) based on Horns Rev1 wind farm measurements	Percentage Error (%)
G1A	6	6	0
G1B	6	6	0
G1C	6	6	0
G2A	6	6	0
G2B	4.91	5.62	12.6
G2C	4.91	5.62	12.6
G3A	6	6	0
G3B	4.91	5.62	12.6
G3C	4.78	5.65	15.3

In case 3, we are going to calculate the wind speed of each turbine when the wind direction is 321 degrees. The wind turbine layout is depicted in Figure 8.

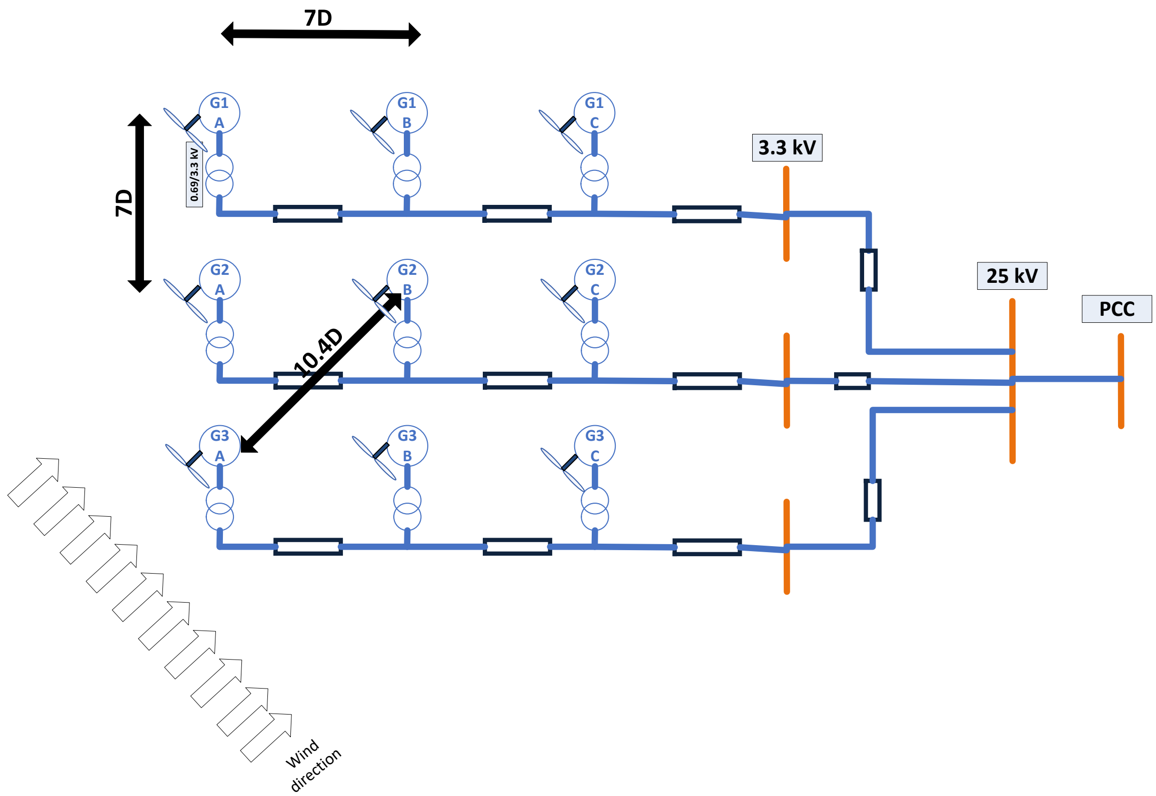

Figure 2-19 Wind Farm Layout for Case 3 With Wind Direction of 312 Degrees

Table 2-5 Case 2: Wind Direction 312 Degrees ($V_0 = 6\ m/s$)

Wind Turbine	Calculated wind speed (m/s) based on Jensen's model	Mean actual wind speed (m/s) based on Horns Rev1 wind farm measurements	Percentage Error (%)
G1A	6	6	0
G1B	5.00	5.5	8.5
G1C	4.89	5.4	9.3
G2A	6	6	0
G2B	5.00	5.5	8.5
G2C	5.00	5.5	8.5
G3A	6	6	0
G3B	6	6	0
G3C	6	6	0

The results from Table 2-3, Table 2-4, and Table 2-5 demonstrate that the maximum error of Jensen's model is around 17%, and in some cases, it is as low as 8.5%. These findings suggest that this method can be considered a suitable option for taking into account the wake effect in large wind farms, as it provides an acceptable level of accuracy while also reducing computational requirements.

2.7 Chapter Summary

This chapter gave a brief overview of reasons for variation in wind speeds, in wind farms. One reason for the variation is simply gusts in wind speed or varying wind speeds in different regions of the wind farm. However, even when one considers the wind farm to be geographically small, so that the ambient wind speed could have been considered uniform, the wake of existing windmills majorly affects the individual windspeeds seen by individual turbines. Jensen's model was examined mathematically for various types of wakes. The results of the model were compared with real-world data from a wind farm to evaluate its accuracy. In later chapters, aggregation methods will be developed that can handle variable wind speeds at different windmills and Jensen’s model can be implemented to find local speed of each wind turbine which will be used in the proposed aggregate model.

Chapter 3

DFIG State Space Dynamic Model

3.1 Introduction

The DFIG is a variable-speed wind turbine generation system, which can capture wind power with higher efficiency compared with fixed-speed systems [3], [4]. With the rapid development of DFIG technology, it has become one of the most widely used wind turbine generation system in large scale wind farms.

DFIG wind power conversion system includes an induction machine, a back-to-back converter, and a three-winding transformer [42]. Figure 3-1 shows a DFIG wind power conversion system. The state space dynamic model of each component of the electrical components is presented in this section. A simple mechanical system is also included in the model but is not described below due to space limitation. Using a generalized combination method, these models are combined to yield the structurally complete dynamic model which is explained in section 4.

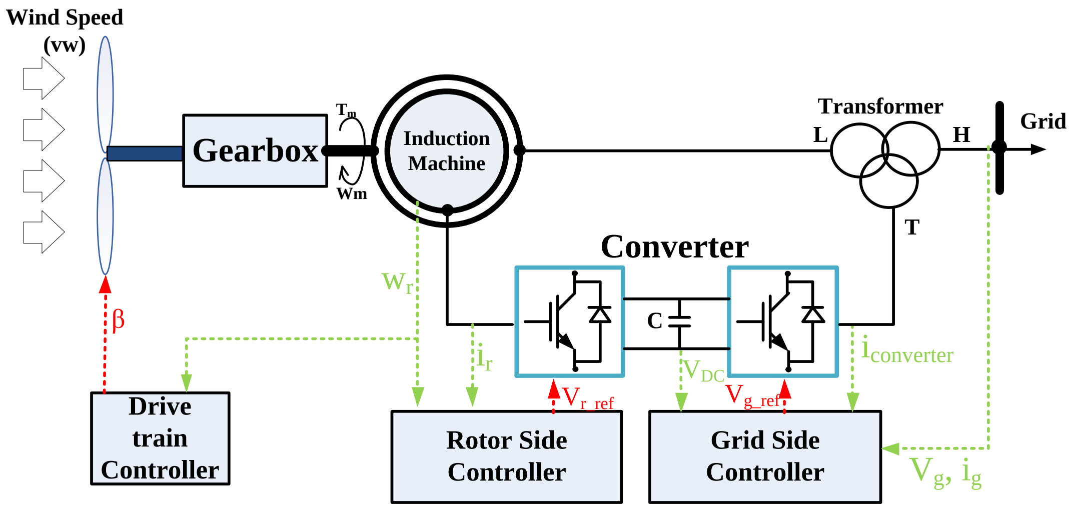

Figure 3-1 Schematic Structure of a DFIG [51]

3.2 Induction Machine Dynamic Model

The induction machine is used in a wide variety of applications as a means of converting electric power to mechanical work. The winding arrangement for a two-pole, three-phase, wye-connected, symmetrical induction machine is shown in Figure 3-2. The stator windings are identical, sinusoidally distributed windings, displaced 120°, with N_s equivalent turns and resistance r_s. The rotor windings will also be considered as three identical sinusoidally distributed windings, displaced 120°, with N_r equivalent turns and resistance r_r .

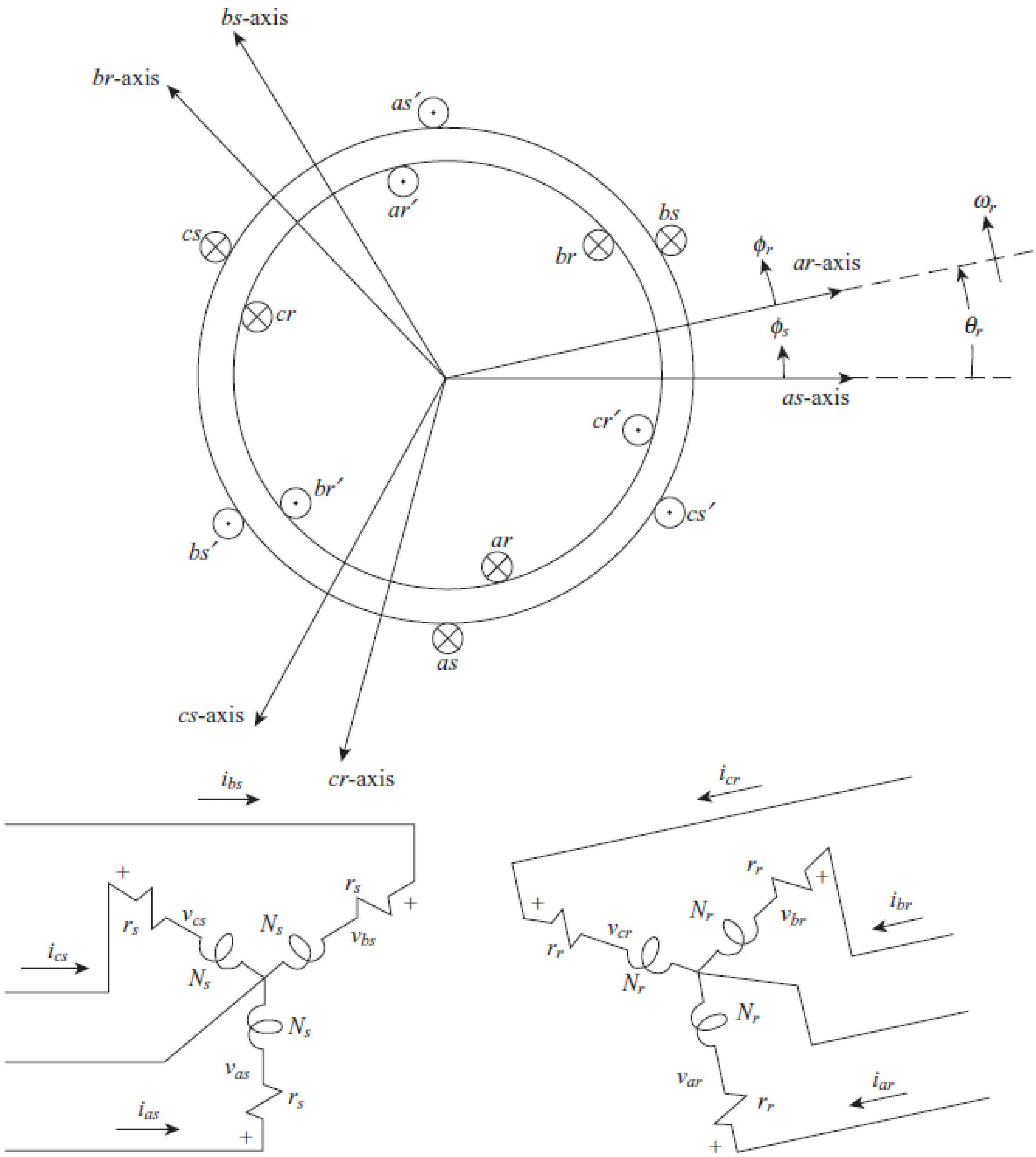

Figure 3-2 Two-Pole, Three-Phase, Wye-Connected Symmetrical Induction Machine [44]

The voltage equations in machine variables may be expressed as equations (5) and (6).

$$V_{abcs} = r_s i_{abcs} + \dot{\lambda}_{abcs} \tag{5}$$

$$V_{abcr} = r_r i_{abcr} + \dot{\lambda}_{abcr} \qquad (6)$$

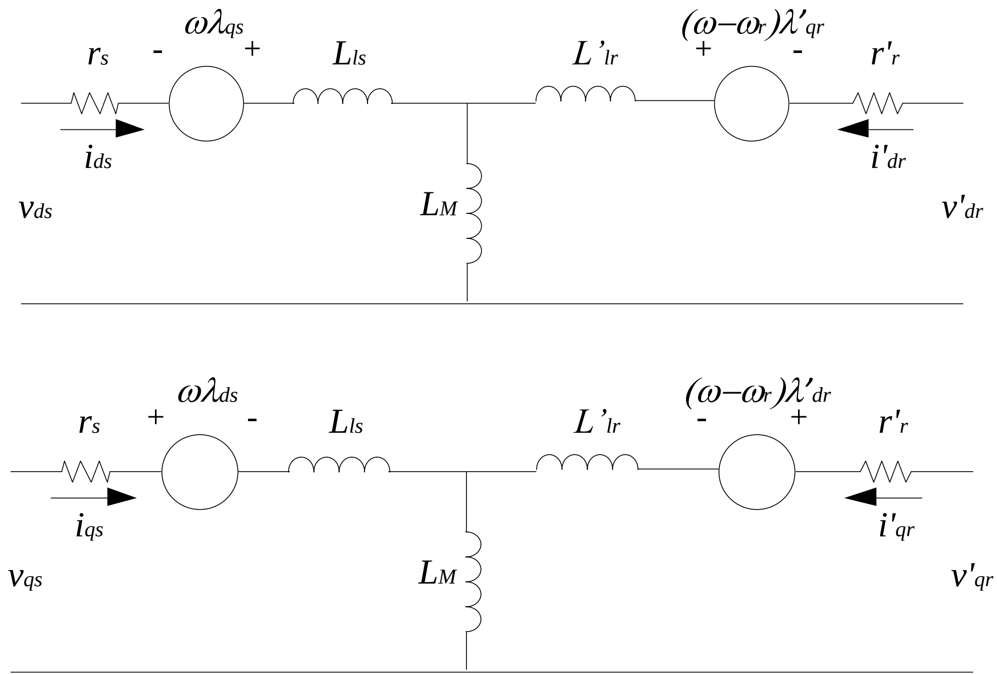

Figure 3-3 Arbitrary Reference-Frame Equivalent Circuits for a Three-Phase, Symmetrical Induction Machine [44]

The induction machine is the core of the DFIG wind power conversion system. Figure 3-3 shows the equivalent circuit for a three-phase induction machine in an arbitrary reference frame [44]. Ignoring the zero sequence, the dynamic equations of the IG in the synchronous rotating (d-q) reference frame are as in (7)-(10) [51].

Stator voltage equations:

$$\begin{cases} V_{ds} = r_s i_{ds} - \omega_s \lambda_{qs} + \dot{\lambda_{ds}} \\ V_{qs} = r_s i_{qs} + \omega_s \lambda_{ds} + \dot{\lambda_{qs}} \end{cases} \tag{7}$$

Rotor voltage equations:

$$\begin{cases} V_{dr} = r_r i_{dr} - (\omega_s - \omega_r)\lambda_{qr} + \dot{\lambda_{dr}} \\ V_{qr} = r_r i_{qr} + (\omega_s - \omega_r)\lambda_{dr} + \dot{\lambda_{qr}} \end{cases} \tag{8}$$

where, ω_r , ω_s are the rotor and synchronous rotating angular velocity, respectively. i_{dr} , i_{qr} , i_{ds} , i_{qs} are the rotor and stator d and q axis current, respectively. λ_{dr} , λ_{qr} , λ_{ds} , λ_{qs} are the rotor and stator d and q axis flux, respectively.

Fluxes equations:

$$\begin{cases} \lambda_{ds} = L_{ls} i_{ds} + L_m (i_{ds} + i_{dr}) = L_s i_{ds} + L_m i_{dr} \\ \lambda_{qs} = L_{ls} i_{qs} + L_m \left(i_{qs} + i_{qr}\right) = L_s i_{qs} + L_m i_{qr} \\ \lambda_{dr} = L_{lr} i_{dr} + L_m (i_{ds} + i_{dr}) = L_m i_{ds} + L_r i_{dr} \\ \lambda_{qr} = L_{lr} i_{qr} + L_m \left(i_{qs} + i_{qr}\right) = L_m i_{qs} + L_r i_{qr} \end{cases} \tag{9}$$

where, L_{ls} , L_{lr} , L_m are the stator leakage inductance, rotor leakage inductance and mutual inductance, respectively. And $L_s = L_{ls} + L_m$, $L_r = L_{lr} + L_m$.

By using equations (7), (8) and (9), the circuit dynamic equations can be derived as (10).

$$\begin{bmatrix} V_{ds} \\ V_{qs} \\ V_{dr} \\ V_{qr} \end{bmatrix} = \begin{bmatrix} r_s & -L_s\omega_s & 0 & -L_m\omega_s \\ L_s\omega_s & r_s & L_m\omega_s & 0 \\ 0 & -L_m(\omega_s-\omega_r) & r_r & -L_r(\omega_s-\omega_r) \\ L_m(\omega_s-\omega_r) & 0 & L_r(\omega_s-\omega_r) & r_s \end{bmatrix} \begin{bmatrix} i_{ds} \\ i_{qs} \\ i_{dr} \\ i_{qr} \end{bmatrix} + \frac{d}{dt} \begin{bmatrix} L_s & 0 & L_m & 0 \\ 0 & L_s & 0 & L_m \\ L_m & 0 & L_r & 0 \\ 0 & L_m & 0 & L_r \end{bmatrix} \begin{bmatrix} i_{ds} \\ i_{qs} \\ i_{dr} \\ i_{qr} \end{bmatrix} \tag{10}$$

Rotor mechanical dynamic equations:

$$T_J \frac{d\omega_r}{dt} + D.\omega_r = T_m - T_e \tag{11}$$

$$T_e = \lambda_{ds} i_{qs} - \lambda_{qs} i_{ds} = L_m(i_{qs} i_{dr} - i_{ds} i_{qr}) \tag{12}$$

where, T_J is the inertia moment of the rotor, T_m , T_e are the prime and electromagnetic torque, respectively.

In the proposed model, the induction machine dynamic model is established according to equations (10), (11), and (12).

Based on the dynamic equations of the induction machine, the electromagnetic torque can be derived as (13)[2].

$$T_e = 3P \frac{L_m}{L_s} \,.\, \mathrm{Im}\{\lambda_s . I_r^*\} = 3P \frac{L_m}{\sigma L_r L_s} \,.\, \mathrm{Im}\{\lambda_r^* . \lambda_s\} \tag{13}$$

where, P is the magnet pairs of induction machine, and $\sigma = 1 - \frac{L_m^2}{L_s L_r}$. From the torque expression, the machine can operate in bi-direction as a motor or a generator according to

[2] Im{} is defined as imaginary part of {}.

the phase relations between stator and rotor fluxes. Furthermore, the stator and rotor active power expression yield to (14) and (15)[3], respectively.

$$P_s = 3.\mathrm{Re}\{\mathrm{V}_s I_s^*\} = \mathrm{R_s}|I_s|^2 + 3.\mathrm{Re}\{j\omega_s L_m I_r . I_s^*\} \tag{14}$$

$$P_r = 3.\mathrm{Re}\{\mathrm{V_r} I_r^*\} = \mathrm{R_r}|I_r|^2 + 3.\mathrm{Re}\{j\omega_s L_m I_s . I_r^*\} \tag{15}$$

By neglecting the copper power losses in the stator and rotor resistances, the relation between the stator and rotor power is achieved by Eq. (16).

$$\begin{cases} P_r = T_e(\omega_r - \omega_l) \\ P_s = T_e\omega_l \\ P_{mech} = T_e\omega_r \end{cases} \tag{16}$$

Therefore, rotor active power can be written as (17) in terms of induction machine slip (s). The equation for rotor active power indicates that DFIG's rotor side can inject or absorb power from the back-to-back converter depending on the slip s.

$$P_r = -s.P_s \tag{17}$$

where $s = \frac{\omega_l - \omega_r}{\omega_l}$.

An induction machine with typical parameters operates at generation mode with $s < 0$. Its power flow schematic is shown in Figure 3-4.

[3] Re{} is defined as real part of {}.

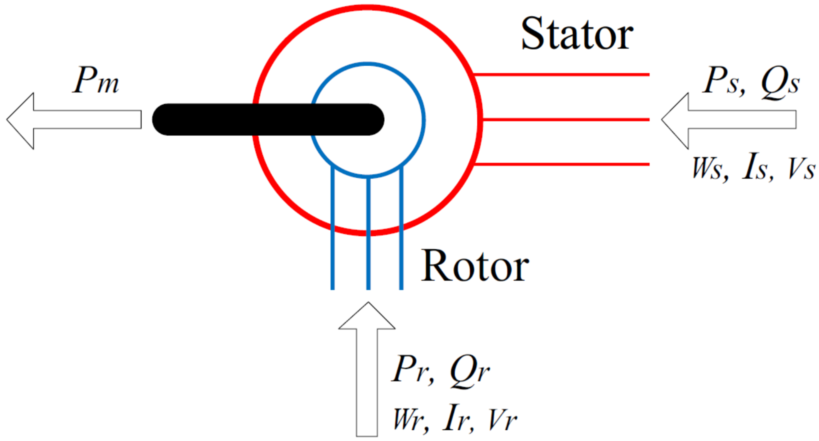

Figure 3-4 Schematics of Power Balance for an Induction Machine at Generation Mode

3.2.1 Interfacing the wake/wind mechanical model of chapter 2

In Chapter 2, each turbine's wind speed is calculated considering wake effect, and in the model for induction machine, it is considered as ω_r. Similarly, the electrical torque (T_e) calculated in (13) is fed back to the mechanical model. The only input variable is the prime torque (T_m) from the drivetrain system, which supposed to be different because of the different incident wind speeds.

3.3 Back-to-back converter dynamic model

The proposed aggregation method is designated to obtain the aggregated parameters of the wind turbine generator and the main circuit parameters of the whole wind farm. Therefore, the average model of VSC is employed in developing the dynamic model of back-to-back converter, in which the IGBT is taken as ideal switching with neglecting switching losses [45]. Figure 3-5 shows a schematic diagram of the grid side VSC (GSC) and the rotor side VSC (RSC) that interface the step-up transformer tertiary winding with the induction machine rotor terminal [51].

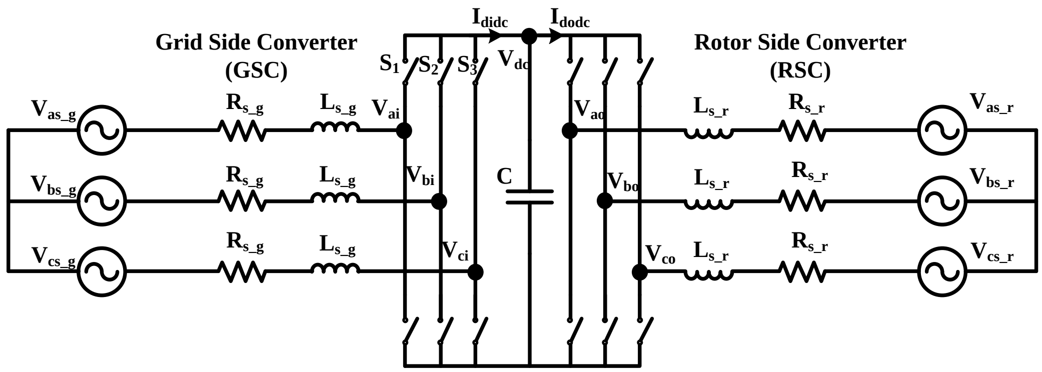

Figure 3-5 Schematic representation of a back-to-back converter [51]

It should be noted that in Figure 3-5 the frequency of voltages and currents on the grid side is the grid frequency ω_s (nominally 50 Hz or 60 Hz in the steady state), and on the rotor side is $\omega_s - \omega_r$.

In this thesis, the converter dynamic model is derived in the abc frame using switching functions and then transformed from that to an appropriate dq0 frame [48].

The ac terminal voltages of the VSCs can be expressed as functions of dc voltage V_{dc} and modulation signals. Taking S_1, S_2, S_3 as the switching functions of the GSC module, the GSC generated ac side fundamental frequency voltages $v_{abc_g} = [v_{a_i}, v_{b_i}, v_{c_i}]^T$ are:

$$\begin{cases} v_{ai} = \frac{1}{2} v_{dc} \cdot S_1 \\ v_{bi} = \frac{1}{2} v_{dc} \cdot S_2 \\ v_{ci} = \frac{1}{2} v_{dc} \cdot S_3 \end{cases} \tag{18}$$

The corresponding switching functions of the converter module are as in (19).

$$\begin{cases} S_1(t) = \frac{1}{2} A_{mi}\, sin(\, \theta_{mi}(t)) \\ S_2(t) = \frac{1}{2} A_{mi}\, sin(\, \theta_{mi}(t) - \frac{2\pi}{3}) \\ S_3(t) = \frac{1}{2} A_{mi}\, sin(\, \theta_{mi}(t) + \frac{2\pi}{3}) \end{cases} \tag{19}$$

where, $\theta_{mi}(t) = \omega_i t + \alpha_{mi}$. Similar expressions as in (7) apply to the RSC voltages $v_{abc_r} = [v_{ao,} v_{bo,} v_{co}]^T$.

Assuming V_{msi} and α_i are amplitude and phase-angle of the voltage source phase-a, gives the GSC and RSC equations in abc frames as below.

$$\begin{cases} v_{abcs_g} = R_{s_g} i_{abc_i} + L_{s_g} \frac{d}{dt}\left(i_{abc_i}\right) + v_{abc_g} \\ v_{abcs_r} = R_{s_r} i_{abc_o} + L_{s_r} \frac{d}{dt}\left(i_{abc_o}\right) + v_{abc_r} \end{cases} \tag{20}$$

Equation (20) is transformed to dq0 coordinates giving (21). Choosing the initial angle of the dq0 transformation as α_i, results in the q component of voltage being 0. This gives the dynamic model of back-to-back converter as in (21) and (25).

$$\begin{bmatrix} L_{s_g} & 0 & 0 & 0 \\ 0 & L_{s_g} & 0 & 0 \\ 0 & 0 & L_{s_r} & 0 \\ 0 & 0 & 0 & L_{s_r} \end{bmatrix} \frac{d}{dt} \begin{bmatrix} i_{qi} \\ i_{di} \\ i_{qo} \\ i_{do} \end{bmatrix} = \begin{bmatrix} -R_{s_g} & -L_{s_g}\omega_i & 0 & 0 \\ L_{s_g}\omega_i & -R_{s_g} & 0 & 0 \\ 0 & 0 & -R_{s_r} & -L_{s_r}\omega_o \\ 0 & 0 & L_{s_r}\omega_o & -R_{s_r} \end{bmatrix} \begin{bmatrix} i_{qi} \\ i_{di} \\ i_{qo} \\ i_{do} \end{bmatrix} \tag{21}$$

$$+\begin{bmatrix} 0.5A_{mi}\,sin(\alpha_i-\alpha_{mi}) \\ -0.5A_{mi}\,cos(\alpha_i-\alpha_{mi}) \\ -0.5A_{mo}\,sin(\alpha_o-\alpha_{mo}) \\ 0.5A_{mo}\,cos(\alpha_o-\alpha_{mo}) \end{bmatrix} v_{dc}$$

$$+\begin{bmatrix} 0 \\ V_{msi} \\ 0 \\ -V_{mso} \end{bmatrix}$$

The capacitor voltage dynamic equation is as below.

$$C\frac{d}{dt}[v_{dc}] = i_{didc} - i_{dodc} \tag{22}$$

The capacitor charging currents i_{didc} and i_{dodc} are:

$$\begin{aligned} i_{didc} &= \frac{3}{4}A_{mi}\left[i_{qi}\,sin(\alpha_{mi}-\alpha_i) + i_{di}\,cos(\alpha_{mi}-\alpha_i)\right] \\ i_{dodc} &= \frac{3}{4}A_{mo}\left[i_{qo}\,sin(\alpha_{mo}-\alpha_o) + i_{do}\,cos(\alpha_{mo}-\alpha_o)\right] \end{aligned} \tag{23}$$

The GSC is used to maintain the dc capacitor voltage and control the reactive power of the DFIG. The RSC is tasked with controlling the rotor terminal voltage and the induction machine's active power [45]. For any wind speed, the maximum power point tracking (MPPT) characteristic determines the optimal power and rotor speed settings which are implemented by the drive train system. The controller schematics are as in Figure 3-6 and Figure 3-7. Other controls including crowbar and fault ride through controls are present but not shown [51].

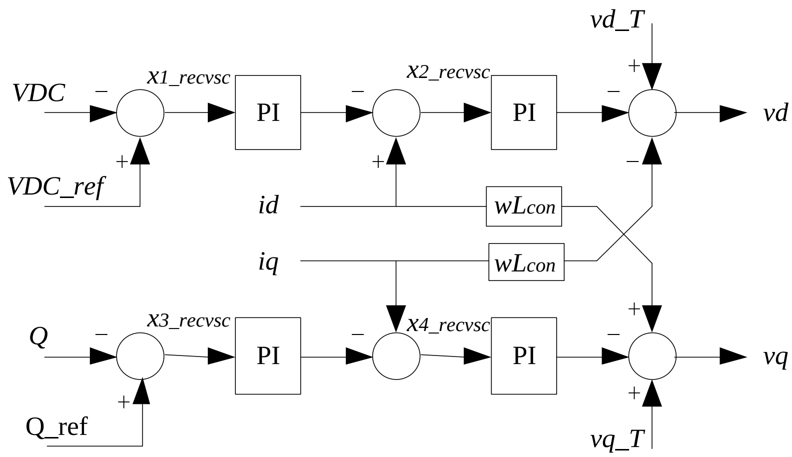

Figure 3-6 GSC Controller Schematic [51]

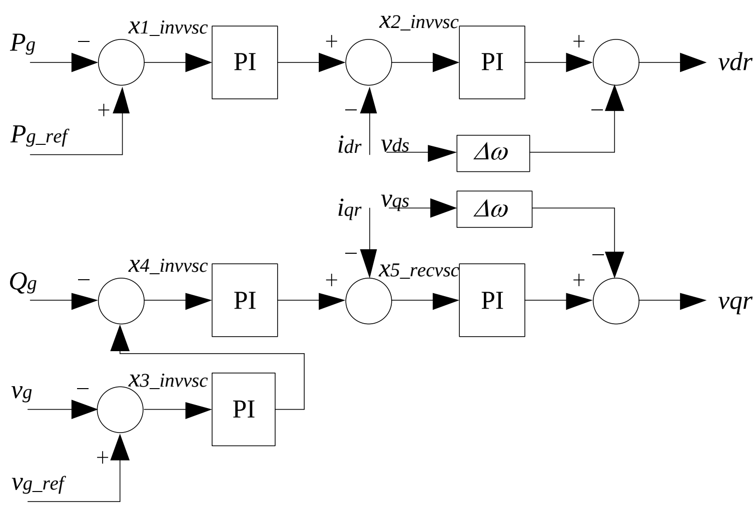

Figure 3-7 RSC Controller Schematic [51]

3.4 Transformer model

The three-winding transformer in Figure 3-8 is used to match the different voltage levels on the rotor and stator sides of the IG and then to step up the stator voltage to a medium voltage level for connecting to the grid. Neglecting the magnetizing branch, it is modelled as in Figure 3-8, (with per-unit leakage impedances X_1, X_2 and X_3), in which, the high voltage (H) terminal is connected to the wind farm collector system, (L) terminal is connected to induction machine stator, and terminal (T) is connected to the grid side VSC.

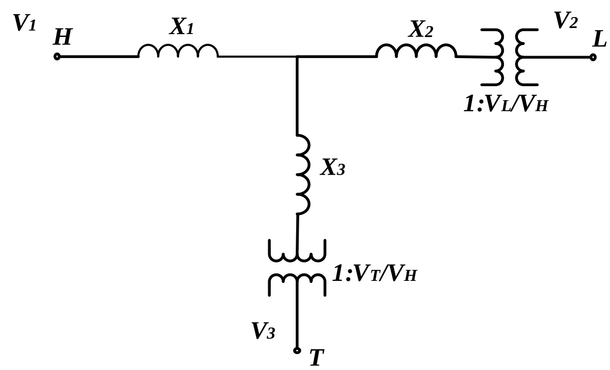

Figure 3-8 Three-Winding Transformer Equivalent Circuit [51]

The current-voltage relationship is as in (24) [47], [48].

$$\frac{d}{dt}\begin{bmatrix} I_1 \\ I_2 \\ I_3 \end{bmatrix} = \frac{1}{LL}\begin{bmatrix} L_2 + L_3 & -a_{12}L_3 & -a_{13}L_2 \\ -a_{12}L_3 & a_{22}(L_1 + L_3) & -a_{23}L_1 \\ -a_{13}L_2 & -a_{23}L_1 & a_{33}(L_1 + L_2) \end{bmatrix}\begin{bmatrix} V_1 \\ V_2 \\ V_3 \end{bmatrix} \tag{24}$$

where,

L_1, L_2, L_3 are the inductors, taking L_1as an example,

$L_1 = \frac{V_1^2 \cdot X\%}{\omega \cdot MVA}$ (in p.u.)

$LL = L_1 \cdot L_2 + L_2 \cdot L_3 + L_3 \cdot L_1$

$$a_{12} = \frac{V_H}{V_L}, a_{22} = \left(\frac{V_H}{V_L}\right)^2, a_{13} = \frac{V_H}{V_T}, a_{23} = \frac{V_H^2}{V_L V_T}, a_{33} = \left(\frac{V_H}{V_T}\right)^2$$

3.5 Complete dynamic model of DFIG

In the previous section, the dynamic models for individual components were established separately. The individual components are connected at their terminals, which creates additional boundary constraints. The boundary voltages cannot be taken as separate inputs any longer when combining the two components as one complete system. A component combination method is put forward here to assemble all individual components into the full dynamic model [51].

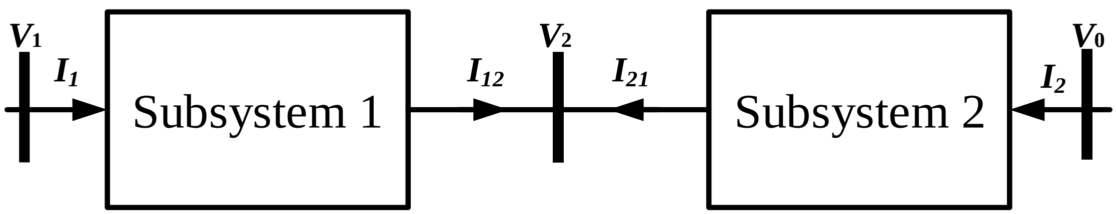

Figure 3-9 Schematic Representation of Two Series-Connected Components [51]

As an example, consider a system as in Figure 3-5, where Subsystem 1 connects to Subsystem 2 at the common boundary bus with voltage V_2. The subsystems equations are as in (25) and (26) which share the same voltage V_2 as the rotor terminal voltage. The current I_{12} $(= -I_{21})$ is also common to the two.

Subsystem 1:

$$\frac{d}{dt}\begin{bmatrix} I_1 \\ I_{12} \end{bmatrix} = \begin{bmatrix} A_{c11} & A_{c12} \\ A_{c21} & A_{c22} \end{bmatrix}\begin{bmatrix} I_1 \\ I_{12} \end{bmatrix} + \begin{bmatrix} B_{c11} \\ B_{c12} \end{bmatrix} V_1 + \begin{bmatrix} B_{c21} \\ B_{c22} \end{bmatrix} V_2 \tag{25}$$

Subsystem 2:

$$\frac{d}{dt}\begin{bmatrix} I_2 \\ I_{12} \end{bmatrix} = \begin{bmatrix} A_{m11} & A_{m12} \\ A_{m21} & A_{m22} \end{bmatrix}\begin{bmatrix} I_2 \\ I_{12} \end{bmatrix} + \begin{bmatrix} B_{m11} \\ B_{m12} \end{bmatrix} V_0 + \begin{bmatrix} B_{m21} \\ B_{m22} \end{bmatrix} V_2 \tag{26}$$

The common voltage V_2 is eliminated to give:

$$\frac{d}{dt}\begin{bmatrix} I_1 \\ I_{12} \\ I_2 \end{bmatrix} = \begin{bmatrix} A_{comb11} & A_{comb12} & A_{comb13} \\ A_{comb21} & A_{comb22} & A_{comb23} \\ A_{comb31} & A_{comb32} & A_{comb33} \end{bmatrix} \begin{bmatrix} I_1 \\ I_{12} \\ I_2 \end{bmatrix} + \begin{bmatrix} B_{comb11} & B_{comb12} \\ B_{comb21} & B_{comb22} \\ B_{comb31} & B_{comb32} \end{bmatrix} \begin{bmatrix} V_0 \\ V_1 \end{bmatrix} \quad (27)$$

The elements $A_{comb11} \cdots B_{comb11}$ etc., are linear algebraic combinations of the original parametersA_{c11}, A_{c12} ... etc. in (25) and (26). The derivations of the elements in equation (27) are not described here in detail since they are just linear algebraic calculation procedures which is done by using MATLAB software. After the two subsystems are combined, the remaining constituent subsystems can be recursively added to the structure one by one in a similar manner culminating in the state space model of the entire DFIG. Finally, the dynamic model of the DFIG is obtained in the form $\dot{x} = Ax + Bu$, with a matrix A of dimension (19×19) having a structure (excluding the mechanical drivetrain) as in Figure 3-10. The drivetrain system model outputs the prime mover torque to the induction generation with wind speed as its input.

$A =$

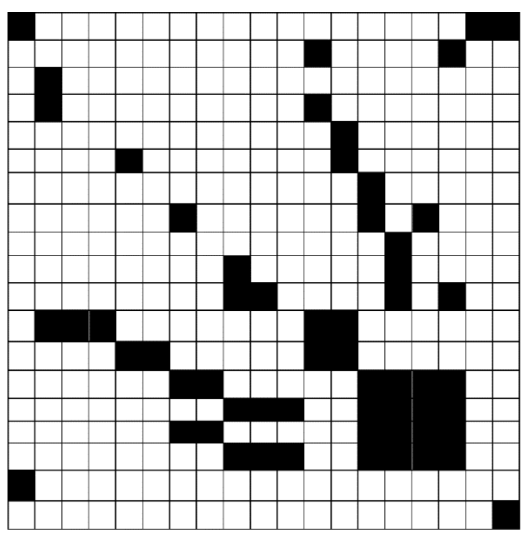

Figure 3-10 Distribution Values of State Matrix A of the DFIG Model [51]

(Note: The Black Blocks are Non-Zero Elements – For Values See Table 3-1)

The 19th order state vector is x = [ω_r, v_{dc}, x_{1_recvsc}, x_{2_recvsc}, x_{3_recvsc}, x_{4_recvsc}, x_{1_invvsc}, x_{2_invvsc}, x_{3_invvsc}, x_{4_invvsc}, x_{5_invvsc}, $i_{di}, i_{qi}, i_{ds}, i_{qs}, i_{dr}, i_{qr}$, $x_{1\_\omega con}$, $x_{2\_\omega con}$]^T. State variables x_{1_invvsc}, x_{2_invvsc}, x_{3_invvsc}, x_{4_invvsc}, x_{5_invvsc} are states associated with the voltage control and active power control of RSC. State variables x_{1_recvsc}, x_{2_recvsc}, x_{3_recvsc}, x_{4_recvsc} are states associated with the capacitance voltage control and reactive power control of GSC and are as marked on the controller diagrams in Figure 3-6 and Figure 3-7. Similarly, $x_{1\_\omega con}$, $x_{2\_\omega con}$ are the states of the machines speed controller. The state variables ω_r, v_{dc}, $i_{di}, i_{qi}, i_{ds}, i_{qs}, i_{dr}, i_{qr}$ are as in (5) to (22) [51].

Table 3-1 Non-Zero Entries of Matrix *A* [51]

Element	value	Element	value	Element	value
$A_{1,1}$	-0.16668	$A_{1,18}$	0.166667	$A_{1,19}$	-16.6667
$A_{2,12}$	0.0075	$A_{2,16}$	-0.00061	$A_{2,17}$	0.09375
$A_{3,2}$	-10	$A_{4,2}$	-250	$A_{4,12}$	-50
$A_{5,13}$	-15	$A_{6,5}$	100	$A_{6,13}$	-250
$A_{7,14}$	1.5	$A_{8,7}$	50	$A_{8,14}$	1.5
$A_{8,16}$	-50	$A_{9,15}$	0.15	$A_{10,9}$	0.2
$A_{10,15}$	0.06	$A_{11,9}$	0.1	$A_{11,10}$	0.02
$A_{11,15}$	0.03	$A_{11,17}$	-0.02	$A_{12,2}$	-6.19195
$A_{12,3}$	1.23839	$A_{12,4}$	1.031992	$A_{12,12}$	-1.69247
$A_{12,13}$	2	$A_{13,5}$	2.063983	$A_{13,6}$	1.031992
$A_{13,12}$	-2	$A_{13,13}$	-5.61404	$A_{14,7}$	-3.11192
$A_{14,8}$	-1.24477	$A_{14,14}$	-0.2078	$A_{14,15}$	3.19123
$A_{14,16}$	3.369591	$A_{14,17}$	3.099414	$A_{15,9}$	-15.5596
$A_{15,10}$	-3.11192	$A_{15,11}$	-1.24477	$A_{15,14}$	-3.19123
$A_{15,15}$	-4.78233	$A_{15,16}$	-3.09941	$A_{15,17}$	3.369591
$A_{16,7}$	3.153909	$A_{16,8}$	1.261563	$A_{16,14}$	0.175527
$A_{16,15}$	-2.22079	$A_{16,16}$	-3.41505	$A_{16,17}$	-2.14123
$A_{17,9}$	15.76954	$A_{17,10}$	3.153909	$A_{17,11}$	1.261563
$A_{17,14}$	2.220793	$A_{17,15}$	4.811773	$A_{17,16}$	2.14123
$A_{17,17}$	-3.41505	$A_{18,1}$	-1	$A_{19,19}$	-100

3.6 Chapter Summary

In this chapter, the state space equations for a Type-3 WTG (DFIG) consisting of an induction machine, a back-to-back converter, and a three-winding transformer in dq0 frame were developed. To achieve this, a series combination method was used in order to combine the three main components of each DFIG into a single DFIG. Finally, the structurally complete dynamic model of DFIG is modeled in MATLAB software, and the state-space model and matrices are extracted. This model will be extended in chapter 4, which discusses the aggregation of multiple WTGs was accomplished by iteratively combining two WTG models at a time.

Chapter 4

Model Structure Preserving Aggregation Method

4.1 Introduction

The modeling approach for wind farms depends on the purpose of investigations to be performed. For investigations of the internal behavior of WTGs within a wind farm, it is required that the wind farm is modeled with all WTGs modelled individually in detail. The detailed model can also be used to represent the collective impacts of a wind farm on large scale power systems for transient stability studies. However, for a wind farm with a large number of WTGs, the whole simulation model will be a very high order system, and therefore, the simulation requires large computation time. To reduce the complexity of the wind farm model during simulation of a large power system, an aggregated or equivalent model with acceptable performances is required.

In this work, two aggregation methods for the electromagnetic simulation model of a wind farm are investigated to speed up the exhaustive computation performances compared with the detailed model. In the first method, wind speed for all wind turbines within a wind farm is considered to be similar. However, in the second method, a new aggregation modeling is proposed based on the state-space model of wind turbines with different wind speeds.

4.2 Wind Farm Aggregation Methods

In the aggregation approach, the wind turbines (WTs) within the farm, each equipped with its internal electrical network, are unified into a single equivalent WT or a multi-machine equivalent. This unified model is designed to deliver the overall response of the entire wind farm at the point of common coupling (PCC). This unification reduces the system's complexity and computational time. However, it should be noted that the performance of WTs in the farm is strongly influenced by varying wind speeds. Given the variability of wind conditions within the farm, the choice of aggregation methods becomes crucial, and this leads to a discussion of various aggregation approaches including full aggregated model (FAM), semi aggregated model (SAM), and multi machine model (MMM). In [77], a comparison was made between all three methods and a detailed model (DM), leading to the conclusion that the MMM demonstrates a superior capability in capturing the impact of various wind speeds and delivering a more comprehensive collective response compared to the SAM. Therefore, in Section 4.6, the results of the MMM are contrasted with those of the proposed model.

The wind generation modeling group of the Western Electricity Coordinating Council (WECC) has published a guidance on wind power plant (WPP) modeling [42]. National Renewable Energy Laboratory (NREL) developed a method to represent a WPP by an equivalent model with an equivalent collector system [19], [21]. An exhaustive simulation study was performed to validate the adequacy of the equivalencing method promoted by NREL for modeling WPP using single- and multiple-machine equivalents. The results suggest that the aggregation technique is adequate for load flow, stability, and electromagnetic transient studies with limitations [20]. Some other literature put forward a reduced model of wind farms, which is developed to capture the main dynamics of high order system. The applicability and effectiveness of different order reduction methods are contrasted [10], [52].

4.3 Wind Farm Dynamic Aggregation Method Considering Uniform Wind Speed

In this section, a wind farm dynamic aggregation method for electromagnetic simulation is interpreted in detail including aggregation theoretical basis.

4.3.1 Dynamic system aggregation theoretical basis

The aggregation process is first described considering a system of two wind turbines. For the entire windfarm, additional wind turbines can be sequentially added, using the same process. Two wind turbines which are connected to the same medium voltage bus as two separate dynamic systems are defined as (28) and (29). By using (27) in Chapter 3, A matrix for each wind turbine is achieved.

$$\dot{x}_1 = A_1 x_1 + B_1 u_1 \tag{28}$$

$$\dot{x}_2 = A_2 x_2 + B_2 u_2 \tag{29}$$

Model aggregation is shown in equation (30) as a process of combining separate dynamic systems.

$$\dot{x}_{12} = A_{12} x_{12} + B_{12} u_{12} \tag{30}$$

where, $x_{12} = [x_1 \quad x_2]^T$, $u_{12} = [u_1 \quad u_2]^T$, $A_{12} = \begin{bmatrix} A_1 & 0 \\ 0 & A_2 \end{bmatrix}$, $B_{12} = \begin{bmatrix} B_1 & 0 \\ 0 & B_2 \end{bmatrix}$.

Aggregating is a process of reducing multiple separate subsystems into one equivalent (i.e., aggregated model). The process is performed using the following transformation matrices [49].

$$X x_{12} = x_e \tag{31}$$

$$U u_{12} = u_e \tag{32}$$

where, the matrices X and U are for aggregation process. The aggregated equivalent model is expressed below.

$$\dot{x}_e = A_e x_e + B_e u_e \tag{33}$$

For the aggregated model, $A_e = X A_{12} X^{-1}$, $B_e = X B_{12} U^{-1}$.

If the two subsystems are exactly the same, the aggregated equivalent model in (33) become the same by aggregating the two subsystems with aggregation matrix as $X = \frac{1}{2}(I \quad I), U = \frac{1}{2}(I \quad I), and\ X^{-1} = 2(I \quad I)^T,\ U^{-1} = 2(I \quad I)^T$

where I is an identity matrix. In this case, the two subsystems can be aggregated as equation (33), and the aggregated matrix as below.

$$\begin{cases} x_e = \frac{1}{2}(x_1 + x_2) \\ A_e = A_1 + A_2 \\ B_e = B_1 + B_2 \end{cases} \tag{34}$$

Equation (34) indicates that if the subsystems are the same, the aggregated model state values are the average of x_1 and x_2, and the model's gains multiply the same number of subsystems [50].

Within a wind farm, if the WTGs are of identical types with equal parameters, and the wind speeds are assumed to be the same, then they can be aggregated together as illustrated in Figure 4-1 and Figure 4-2. Based on the aggregation method if the WTGs type and wind speeds are the same, they can be aggregated together accurately by amplifying the number of WTGs (considered as n).

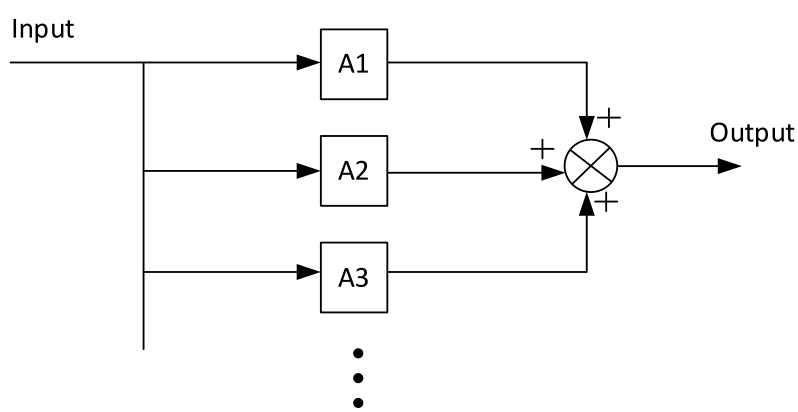

Figure 4-1 Equivalent System Diagram [52]

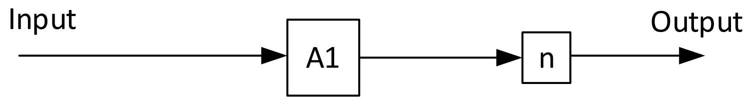

Figure 4-2 Aggregated System [52]

4.3.2 Wind farm electromagnetic simulation aggregation method

In an accurate aggregation, the power flow must be the same between the original and aggregated models. At the same time, the electromagnetic responses must be relatively close. The proposed aggregated model is depicted in Figure 4-3.

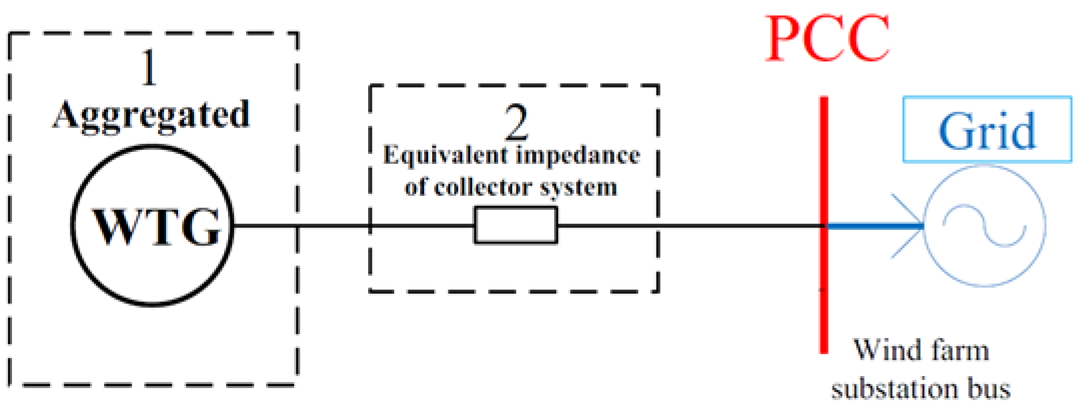

Figure 4-3 Wind Farm Aggregation Model Structure [52]

The aggregated model includes two parts: (i) Aggregated WTG having the same output power, (ii) The equivalent impedance of the collector system to capture the same power loss.

To guarantee the power flow of the original detailed model and the aggregated one are the same, the aggregated WTG must generate the same amount of power with the same wind speed. According to the aggregation method proposed above, within a wind farm, the same type WTGs connected to the same feeder with the same wind speed will be divided as one group and be aggregated as one equivalent WTG. The aggregation can be realized using a current amplifier to amplify an individual WTG's power. The current amplifier is derived as Figure 4-4.

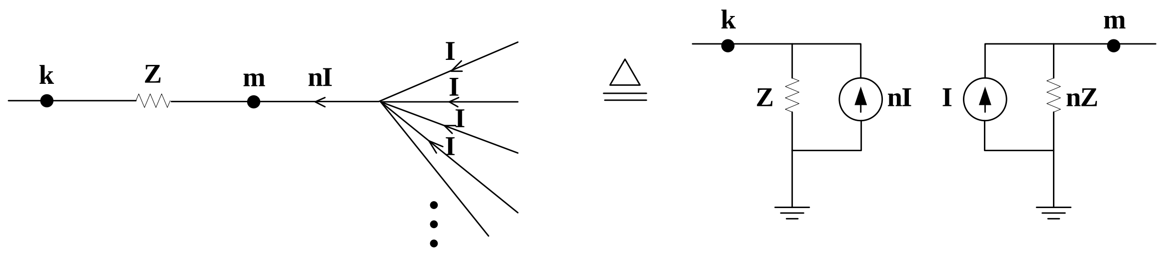

Figure 4-4 Current Amplifier Model: (a) Current Source Model (b) Current Amplifier Model [52]

Based on the current source model for WTGs, the k node in Figure 4-4 (a) is taken as a constant voltage bus, which is reasonable for connecting to the grid. The voltage of node m can be derived as (35).

$$u_m = u_k + Z(nI) = u_k + nZ(I) \tag{35}$$

So, the current amplifier can be modeled as Figure 4-4(b) to guarantee the power monitored at node k, and the same voltage monitored at bus m as the original detailed model.

The equivalent impedance is added to capture the power loss and voltage drop caused by the collector system. Based on the assumption that the aggregated WTGs with short distances connected to the same feeder have the same wind speed and terminal voltage, the terminal currents are almost the same. So, the equivalent impedance (Z_{equ}) can be derived as (36).

$$Z_{equ} = \frac{\sum_{i=1}^{n}(i^2 Z_i)}{n^2} \tag{36}$$

where, n is the number of WTGs to be aggregated, Z_i is the i_{th} impedance connected to the i_{th} WTG.

4.4 Wind Farm Dynamic Aggregation Method with Different Local Wind Speeds

As previously discussed, it is very important to consider variations of wind speed at different turbine locations within a wind farm with a large number of wind turbines. Therefore, a novel aggregation method is proposed in this work based on the wind turbine state-space models. This method is applicable for a cluster of WTGs of identical structures, but with various parameters and input wind speed. The developed approach and its validation were conducted using MATLAB/Simulink ® and PSCAD software.

As mentioned in the previous section, the aggregated model is constructed recursively by combining two DFIG state space representations at a time and equivalencing it to the state space representation of a single DFIG, ensuring that they both have identical steady state responses. It may not be possible to equivalence the entire wind farm to a single equivalent WTG. However, large numbers of WTGs could be so aggregated to create a model with only a few representative WTGs, thereby greatly reducing the overall model size.

4.4.1 Equivalencing the Collector System Impedance

The impedances of cables connecting the DFIGs to the wind farm collector system cause voltage reduction and power losses. This thesis puts forth a more general method based on power flow for finding a single equivalent impedance which is different from that reported in previous work [19], [21]. This equivalent impedance is designed so that the total generated power, the power received at the PCC bus and the PCC bus voltage are the same as in the detailed model.

Consider the case of two DFIGs in parallel with connecting impedances Z_1 and Z_2 as in Figure 4-5(a), the DFIG terminal bus is taken as a PQ node with generating powers as ordered by the converter control system corresponding to the turbine's incident wind speed.

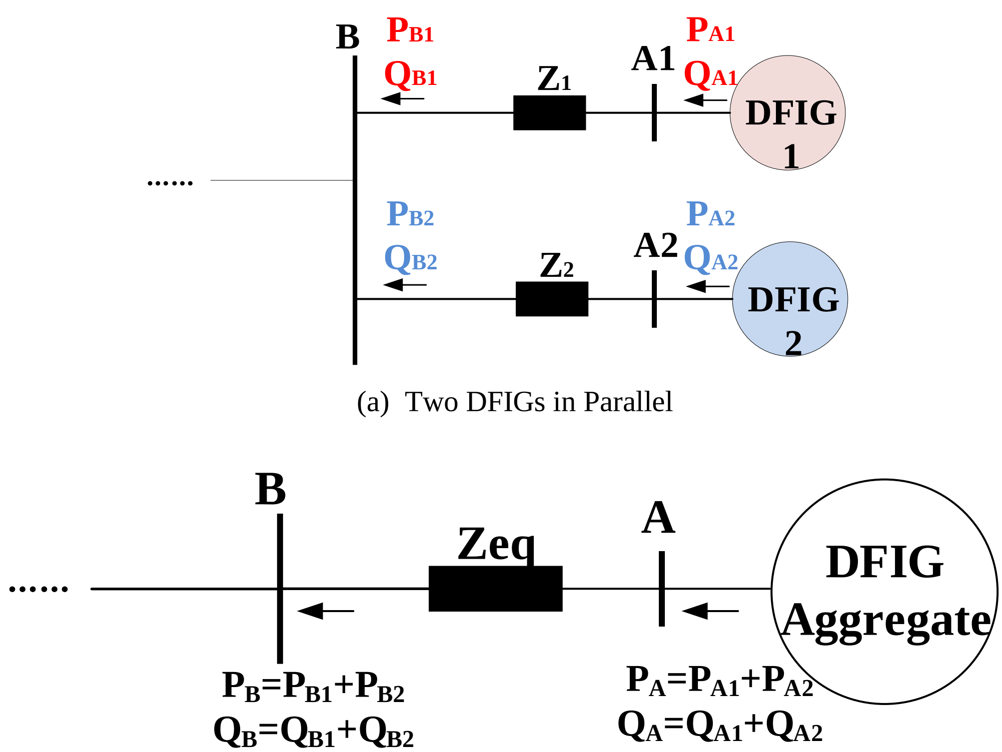

(b) Aggregate Model with Equivalent Impedance Z_{eq}

Figure 4-5 Equivalencing the Individual DFIG Connecting Impedances in Parallel

The wind generator power flows ($P_{A1}, Q_{A1}, P_{B1}, Q_{B1}, P_{A2}$,…,etc.) and voltages ($V_{A1}\angle\theta_{A1}, V_{A2}\angle\theta_{A2}$ and $V_B\angle\theta_B$) can be calculated using commercial software or, as is the case in this thesis, by a user developed program. From these, the equivalent impedance $Z_{eq} = R + jX$ of the collector system is calculated numerically by solving the following algebraic equations using the Newton-Raphson method in unknowns R, X, V_A and θ_A.

$$\begin{cases} P_A = \dfrac{XV_AV_B\,sin(\theta_A - \theta_B) + RV_A^2 - RV_AV_B\,cos(\theta_A - \theta_B)}{R^2 + X^2} \\ Q_A = \dfrac{XV_A^2 - XV_AV_B\,cos(\theta_A - \theta_B) - RV_AV_B\,sin(\theta_A - \theta_B)}{R^2 + X^2} \\ P_B = \dfrac{XV_AV_B\,sin(\theta_A - \theta_B) - RV_B^2 + RV_AV_B\,cos(\theta_A - \theta_B)}{R^2 + X^2} \\ Q_B = \dfrac{-XV_B^2 + XV_AV_B\,cos(\theta_A - \theta_B) - RV_AV_B\,sin(\theta_A - \theta_B)}{R^2 + X^2} \end{cases} \tag{37}$$

where, $P_A = P_{A1} + P_{A2}$, $Q_A = Q_{A1} + Q_{A2}$, $P_B = P_{B1} + P_{B2}$,$Q_B = Q_{B1} + Q_{B2}$ are for this two DFIGs in parallel.

This approach is applicable to machines directly connected to the PCC through impedances $Z_1, Z_2, \dots, Z_n$. However, windfarms may have different connection arrangements. For example, a typical configuration of WTGs in a wind farm is shown in Figure 4-6 with the DFIGs connected in a string configuration. The DFIGs in the same string are connected to the wind farm substation bus (PCC bus) via a feeder. In this case a recursive procedure can be used. We start with $DFIG_1$ with impedance $Z_1 = Z_{12}$ and $DFIG_2$ with $Z_2 = 0$. Using the above procedure, they can be combined to form an equivalent impedance Z_{eq1} and equivalent generator $DFIG_{e1}$. In the next step, this can be combined with $DFIG_3$, again taking the first impedance as $Z_{eq1} + Z_{23}$, and the second as

$Z_3 = 0$. This process is continued till a single equivalent impedance Z_{eq} is obtained. The equivalent impedance produces the same power losses and PCC voltage as the detailed model and ensures the same power flow seen from PCC bus.

The resulting equivalent system is shown in Figure 4-7, and consists of a single equivalent generator connected to the PCC with an equivalent impedance as calculated above. The next section will show how the aggregate generator model is developed. The other strings can be made into similar equivalents. All these equivalents may be combined into a single DFIG with equivalent connecting impedance.

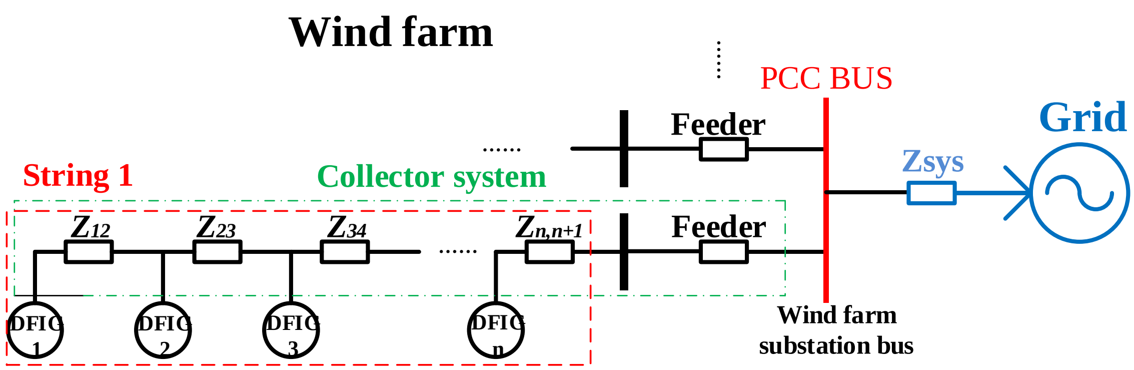

Figure 4-6 Typical Configuration of WTGs in a Wind Farm

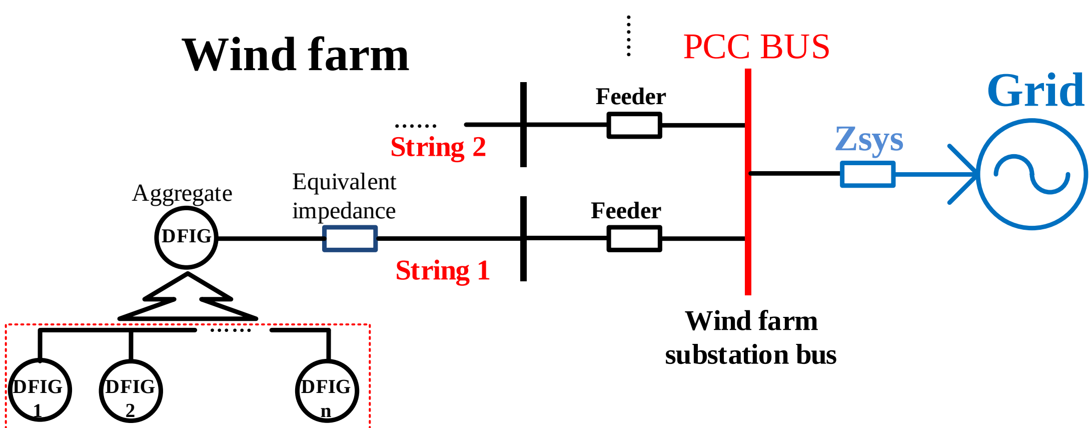

Figure 4-7 DFIGs in Parallel with the Equivalent Impedance of String 1

4.4.2 Combining the State Space Representations of Two DFIGs

Many EMT programs model the machine as a current source which injects the calculated current from them [53]. Thus, an aggregation method is proposed, which combines the current generation from all the DFIGs with a similar block structure in the aggregate into a single equivalent DFIG of the same structure.

The output current of the equivalent generator is the sum of the currents of all the DFIGs in the string.

The aggregation of the DFIGs can be performed recursively with two units at a time, so that n-1 aggregation procedures are performed for n DFIGs in the string, as in [54], [55]. The state equations for DFIG 1 and 2 are considered as in (38) and (39) respectively.

$$\begin{cases} \dot{x}_1 = A_1x_1 + B_1u_1 = A_1x_1 + B_{1vdq}[v_d, v_q]^T + B_{1Tm}[T_{m1}] \\ y_1 = i_{dq1} = C_1x_1 \end{cases} \tag{38}$$

$$\begin{cases} \dot{x}_2 = A_2x_2 + B_2u_2 = A_2x_2 + B_{2vdq}[v_d, v_q]^T + B_{2Tm}[T_{m2}] \\ y_2 = i_{dq2} = C_2x_2 \end{cases} \tag{39}$$

The outputs in s domain can be expressed as in (40).

$$\begin{cases} i_{dq1} = C_1(sE - A_1)^{-1}\left(B_{1vdq}[v_d, v_q]^T + B_{1Tm}[T_{m1}]\right) \\ i_{dq2} = C_2(sE - A_2)^{-1}\left(B_{2vdq}[v_d, v_q]^T + B_{2Tm}[T_{m2}]\right) \end{cases} \tag{40}$$

The outputs y_1 and y_2 are the injected currents i_d and i_q (in d-q coordinate) from these DFIGs which are states in the dynamic model, and hence the absence of the 'D' matrix in

(38) and (39). The C matrix only picks out the d and q components of stator current, so the remaining entries are zero. Thus:

$$C_1 = C_2 = \begin{bmatrix} 0 & 0 & 0 & 0 & 0 & 0 & 0 & 0 & 0 & 0 & 0 & 0 & 1 & 0 & 0 & 0 & 0 & 0 & 0 \\ 0 & 0 & 0 & 0 & 0 & 0 & 0 & 0 & 0 & 0 & 0 & 0 & 0 & 1 & 0 & 0 & 0 & 0 & 0 \end{bmatrix} \quad (41)$$

With identical parameters for transformer and converter and with data as in Table 4-3 and Table 4-4, matrices B_1 and B_2 are:

$$B_1 = B_2 = \begin{bmatrix} 0 & 0 & 0 & 0 & 0 & -1 & -1 & 0 & 0 & 0 & 0 & 0 & 0.062 & 0 & -0.063 & 0 & 0 & 0 & 0 \\ 0 & 0 & 0 & 0 & 0 & 0 & 0 & 0 & 0 & 0 & 0 & 0 & 1.761 & 0 & -1.245 & 0 & 0 & 0 & 0 \\ 0 & 0 & 0 & 0 & 0 & 0 & 0 & 0 & 0 & 0 & 0 & 0 & 0 & 1.761 & 0 & -1.245 & 0 & 0 & 0 \end{bmatrix}^T \quad (42)$$

Converting to the Laplace (s) domain, the aggregate model is obtained by summing y_1 and y_2 as in (43).

$$\begin{aligned} i_{dqC} &= i_{dq_1} + i_{dq_2} \\ &= C_1(sE - A_1)^{-1}\left[B_{1dq}v_{dq1} + B_{1T_m}T_{m1}\right] + C_2(sE - A_2)^{-1}\left[B_{2dq}v_{dq2} + B_{2T_m}T_{m2}\right] \\ &= C[(sE - A_1)^{-1}Bu_1 + (sE - A_2)^{-1}Bu_2] \end{aligned} \quad (43)$$

where, E is identity matrix, s is Laplace operator. The inputs u_1 and u_2 typically include the components of the grid terminal voltage v_{d1}, v_{q1} and v_{d2}, v_{q2}, and prime mover torques T_{m1} and T_{m2}. The input matrix B can be further simplified if the grid side voltages are assumed the same for all DFIGs in the string, which is reasonable since the impedances Z_{12}, Z_{23} etc., are small. However, the prime mover torque inputs can be different because of different incident wind speeds. Taking k as the ratio between the torques $k = \frac{T_{m2}}{T_{m1}}$, (43) becomes (44). Note that in (44), A_1 and A_2 have the same order, and hence the orders of matrices $(sE - A_1)^{-1}$and $(sE - A_2)^{-1}$are the same which makes it feasible to construct an equivalent of the same state space structure as of the individual DFIGs.

$$\begin{aligned} i_{dqC} &= i_{dq_1} + i_{dq_2} \\ &= C[(sE - A_1)^{-1}Bu_1 + (sE - A_2)^{-1}Bku_1] \\ &= (1+k)C\left[\frac{1}{1+k}(sE - A_1)^{-1} + \frac{k}{1+k}(sE - A_2)^{-1}\right]Bu_1 \end{aligned} \tag{44}$$

At this stage, the order of the state equations will be typically twice that of an individual DFIG as two DFIGs are being combined. For the final implementation, this must be reduced to the order of a single DFIG. This is described below.

4.4.3 Recursive Aggregation Procedure

Comparing (38) with (44), the matrices A_1, B_1 and C_1 are replaced by the terms $A_a'(s)$, B_a, and C_a as in (45).

$$\begin{aligned} A_a'(s) &= sE - \left[\frac{1}{1+k}(sE - A_1)^{-1} + \frac{k}{1+k}(sE - A_2)^{-1}\right]^{-1} \\ B_a &= B \\ C_a &= (1+k)C \end{aligned} \tag{45}$$

For a representation that preserves the structure of a single DFIG, we need $A_a'(s)$ to be a constant matrix (not a function of *s*). To get a single DFIG to represent the two DFIGs, it is observed that the steady state outputs must match, so setting $t = +\infty$ i.e., $s = 0$, in (45) gives matrix $A_a = \left(\frac{1}{1+k}(A_1)^{-1} + \frac{k}{1+k}(A_2)^{-1}\right)^{-1}$. Once A_a is known, and using B_a and C_a from (45), the equivalent system is formed in state variable form as in (46).

$$\begin{cases} \dot{x} = A_a x + B_a u \\ y = C_a x \end{cases} \tag{46}$$

Once these matrices are known, the parameters of the equivalent DFIG are determined and included in any EMT simulator as a single DFIG. Additional DFIGs can be added one at a time to this aggregate until all machines are included. The procedure automatically guarantees identical steady state response to the detailed model. Model validation will show that it also gives an accurate transient response.

4.4.4 Modified Transformer Representation to Magnify Current

The step-up transformer can be used to scale the single DFIG's current to that of the two DFIGs in accordance with the output matrix C_a by multiplying the currents from the 'H' terminal in Figure 3-1 by a scale factor (1+*k*). This is achieved by multiplying the first row of the inductance matrix in (24) by (1+*k*) to give (47).

$$\frac{d}{dt}\begin{bmatrix} I_{1C} \\ I_2 \\ I_3 \end{bmatrix} = \frac{1}{LL}\begin{bmatrix} (1+k)(L_2+L_3) & -(1+k)a_{12}L_3 & -(1+k)a_{13}L_2 \\ -a_{12}L_3 & a_{22}(L_1+L_3) & -a_{23}L_1 \\ -a_{13}L_2 & -a_{23}L_1 & a_{33}(L_1+L_2) \end{bmatrix}\begin{bmatrix} V_1 \\ V_2 \\ V_3 \end{bmatrix} \tag{47}$$

The resulting DFIG can be treated as a single unit and combined with other DFIGs in the string in a recursive manner to eventually generate the entire aggregate equivalent. It should be noted that the aggregated model can be implemented as a single DFIG in any EMT simulation software, as it does not require modification of existing models in the software, merely an appropriate selection of the parameters.

4.5 Model Validation for Proposed Aggregated Model

The proposed DFIG aggregation method is validated by comparing EMT simulation results for the case of all DFIGs modelled separately, with the aggregated DFIG. PSCAD/EMTDC is used as the EMT simulation tool. Initially two simple examples are used to demonstrate that the aggregation procedure works with changing wind speeds or different parameters for each DFIG. Next, a demo wind farm case with 10 identical DFIGs represented in Figure 4-8 is investigated considering different input wind speed for wind turbines due to wake effect discussed in Chapter 2.

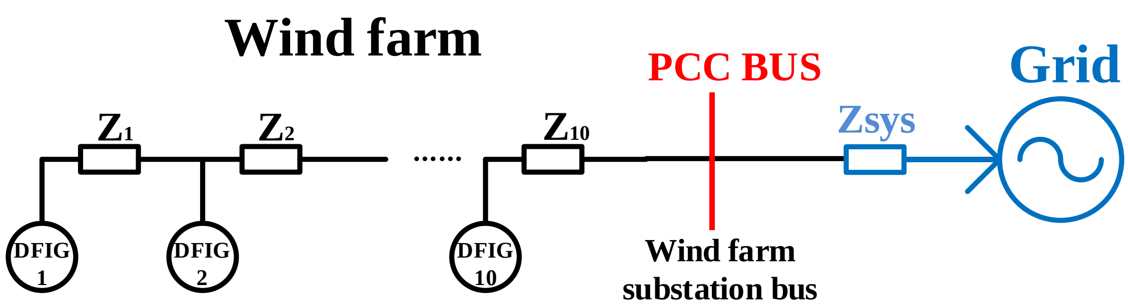

Figure 4-8 Wind Farm Consisting of 10 DFIGs

Data for the DFIG and feeder impedances are given in Table 4-1 to Table 4-6. The turbine model is as in [56] with parameters as in Table 4-1. The mechanical power of the wind turbine obtained from the wind energy can be calculated using several different forms for C_p that are available in literature. The thesis examples use the form in [78] based on the following formula.

$$P = \frac{\rho}{2} \times A_r \times V_W^3 \times C_p(\lambda, \theta)$$
$$C_p = C_p(\theta, \lambda) = C_1 \left(\frac{C_2}{\lambda_i} - C_3\theta - C_4\right) e^{-\frac{C_5}{\lambda_i}} + C_6\lambda \quad (48)$$

where:

$\lambda_i = \frac{1}{\lambda + 0.08\theta} - \frac{0.035}{\theta^3 + 1}$

$C_1 = 0.5176, C_2 = 116, C_3 = 0.4, C_4 = 5, C_5 = 21, C_6 = 0.0068$

ρ is the air density

A_r is the area swept by the rotor blades

V_W is the wind speed

C_p is the power coefficient, a function of λ and θ

λ is the tip speed ratio

θ is the pitch angle

Table 4-1 Wind Turbine Parameters

Parameter	Value
Rated active power	5MW
Turbine radius	68.5 m
Air density	1.225 kg/m3
Base wind speed	11 m/s

Table 4-2 Induction Generator Parameters

Parameter	value
Rated power	5.6 MVA
Rated voltage (L-L)	0.9 kV
Base angular frequency	60 Hz
Stator/rotor turns ratio	0.391
Angular moment of inertia	6 s

Parameter	value
Mechanical damping	0.0001 p.u.
Stator resistance	0.0054 p.u.
Wound rotor resistance	0.00607 p.u.
First squirrel cage resistance	0.298 p.u.
Second squirrel cage resistance	0.018 p.u.
Magnetizing inductance	4.5 p.u.
Stator leakage inductance	0.10 p.u.
Wound rotor leakage inductance	0.11 p.u.

Table 4-3 Step-Up Transformer Parameters

Parameter	value
3 Phase MVA	5.833 MVA
Base operation frequency	60 Hz
Winding 1 Line-to-Line voltage (H in Figure 3-1)	33 kV
Winding 2 Line-to-Line voltage (T in Figure 3-1)	0.69 kV
Winding 3 Line-to-Line voltage (L in Figure 3-1)	0.9 kV
Winding 1/2/3 type	Y/Y/Y
Positive sequence leakage reactance (#1-#2)	0.025 p.u.
Positive sequence leakage reactance (#1-#3)	0.013 p.u.
Positive sequence leakage reactance (#2-#3)	0.013 p.u.
No load losses	0.002 p.u.
Copper losses	0.005 p.u.
Magnetizing current	2.0 %

Table 4-4 VSC Parameters and Control Schemes

Parameter	value
3-Phase MVA	2.15 MVA
Dc Capacitor	75000 μF
Capacitor nominal voltage	1.45 kV
Grid-side Line-to-Line voltage	0.69 kV

Table 4-5 Wind Farm Impedance Parameters

Parameter	Value
Z_1, Z_3, Z_5, Z_7, Z_9	0.046 Ω+0.000097609 H
Z_2, Z_4, Z_6, Z_8, Z_{10}	0.092 Ω+0.00019522 H
Z_{sys} (SCR = 5)	0.560 Ω+0.01039865 H

The MPPT characteristic in per-unit is shown in Figure 4-9 and is used to determine the mechanical power and hence torque, from the wind at any rotor speed. The power base P_m for per-unitizing is the induction machine's rated power and the base wind speed is 11 m/s.

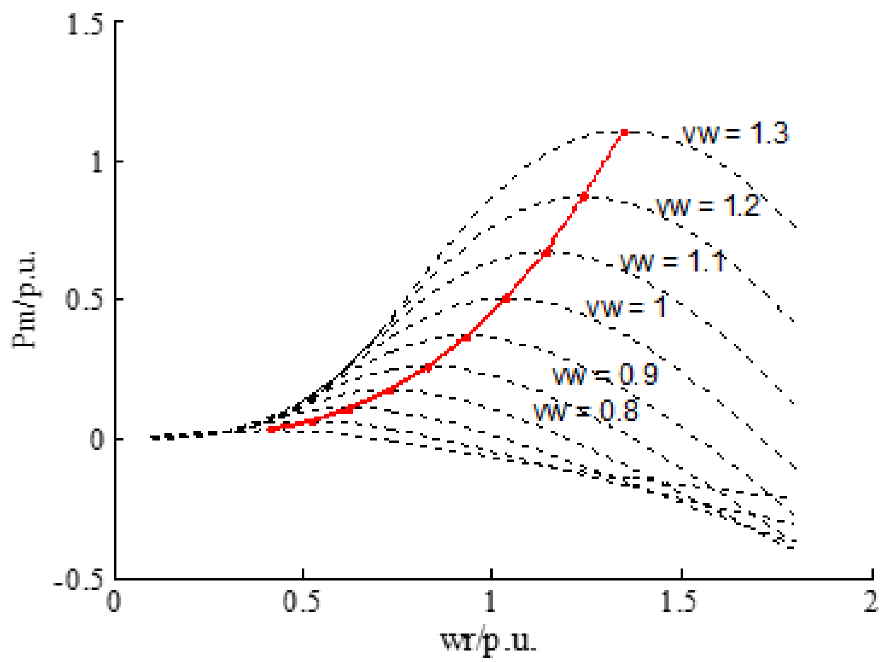

Figure 4-9 MPPT Curve of a Typical Wind Turbine

4.5.1 Performance of Aggregate Model under Changing Wind Speeds

A model consisting of 3 identical DFIGs in a string is used to investigate the method's applicability to simulate conditions with varying wind speeds. The parameters are considered to be as in Section 4.5. Figure 4-10 shows the PSCAD simulation results when individual wind velocities range from 10.93 m/s to 13.86 m/s, which is typical for a wind farm. In order to demonstrate the ability of the model to handle wind gusts, the wind velocities are ramped from 12.61 m/s to 13.86 m/s at t = 1 s for DFIG 1, and then decreased to 11.34 m/s starting at t = 5 s. The ramp rate is ± 2.5 m/s^2. Note that as all the windmills are in the same windfarm, the range of variation is relatively small. Similarly, the wind speed for DFIG 2 goes from 12.15 m/s to 13.37 m/s at t = 2 s, and then to 10.93 m/s at t = 6 s. The individual wind speeds are used to calculate the equivalent wind speed for the aggregated model (blue curve). The real and reactive power plots in Figure 4-10 confirm that the aggregate model can still retain the same steady state total power as the detailed model.

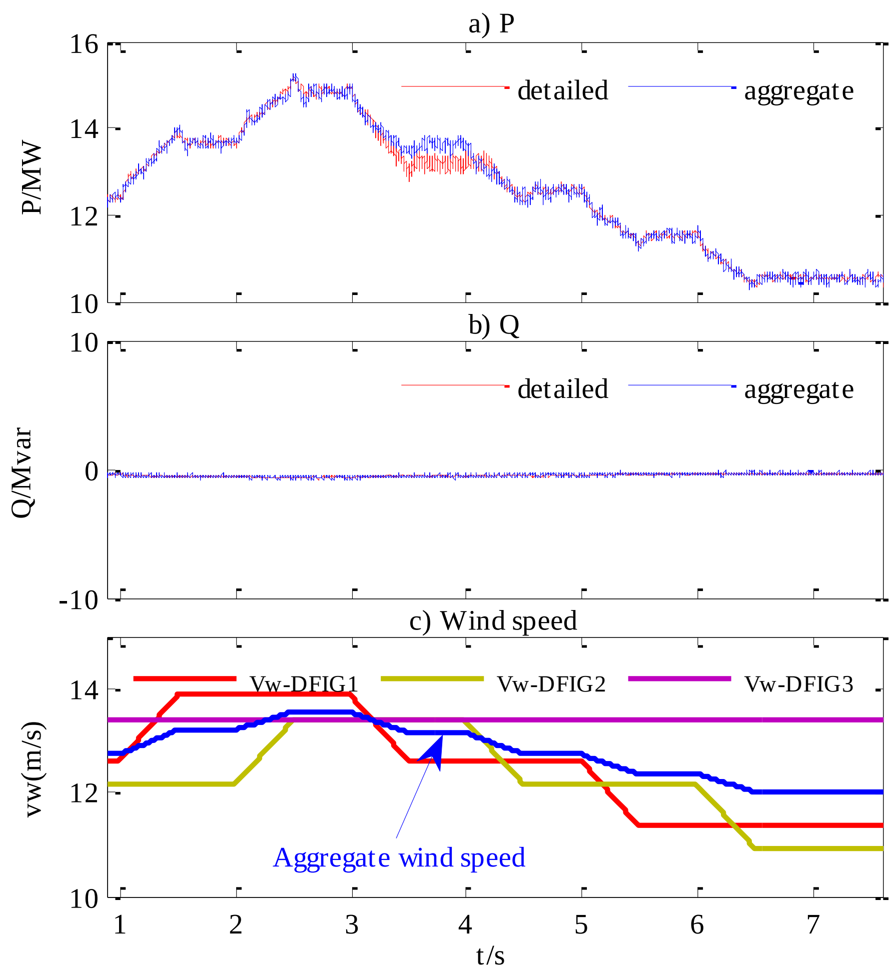

Figure 4-10 Simulation Results for Varying Wind Velocities

4.5.2 Performance of Aggregate Model with Non-identical DFIGs

A two machines case with one machine having 20% larger leakage impedances as in Table 4-6 and consequently different state matrices A for each DFIG is considered below.

Table 4-6 Two DFIG System: Parameters and Operating Points for $V_w = 1.18\ pu$ (Wind Speed Base = 11 m/s) $P_{base} = 5.6\ MW$

DFIG #	Rotor angular speed at max. power ω_r (p.u.)	Prime power P_m (pu) at ω_r	Rotor leakage inductance L_{rl} (p.u.)	Stator leakage inductance L_{sl} (p.u.)	Impedance Z (Ohm)
DFIG1	1.1	0.76	0.11	0.1	0.1+j0.376
DFIG2	1.1	0.76	0.132	0.12	0.3+j1.131

Figure 4-11 shows a comparison of the transient responses for the 2-machine case from the detailed model, proposed aggregate model and the model in references [16], [17] (referred to as 'one-equivalent'). The disturbance is a 10 ms short circuit which causes the terminal voltage to temporarily drop to zero. The active power (P) and relative errors between models are shown in Figure 4-11 (a) and (b) respectively, and the reactive power and errors in Figure 4-11 (c) and (d).

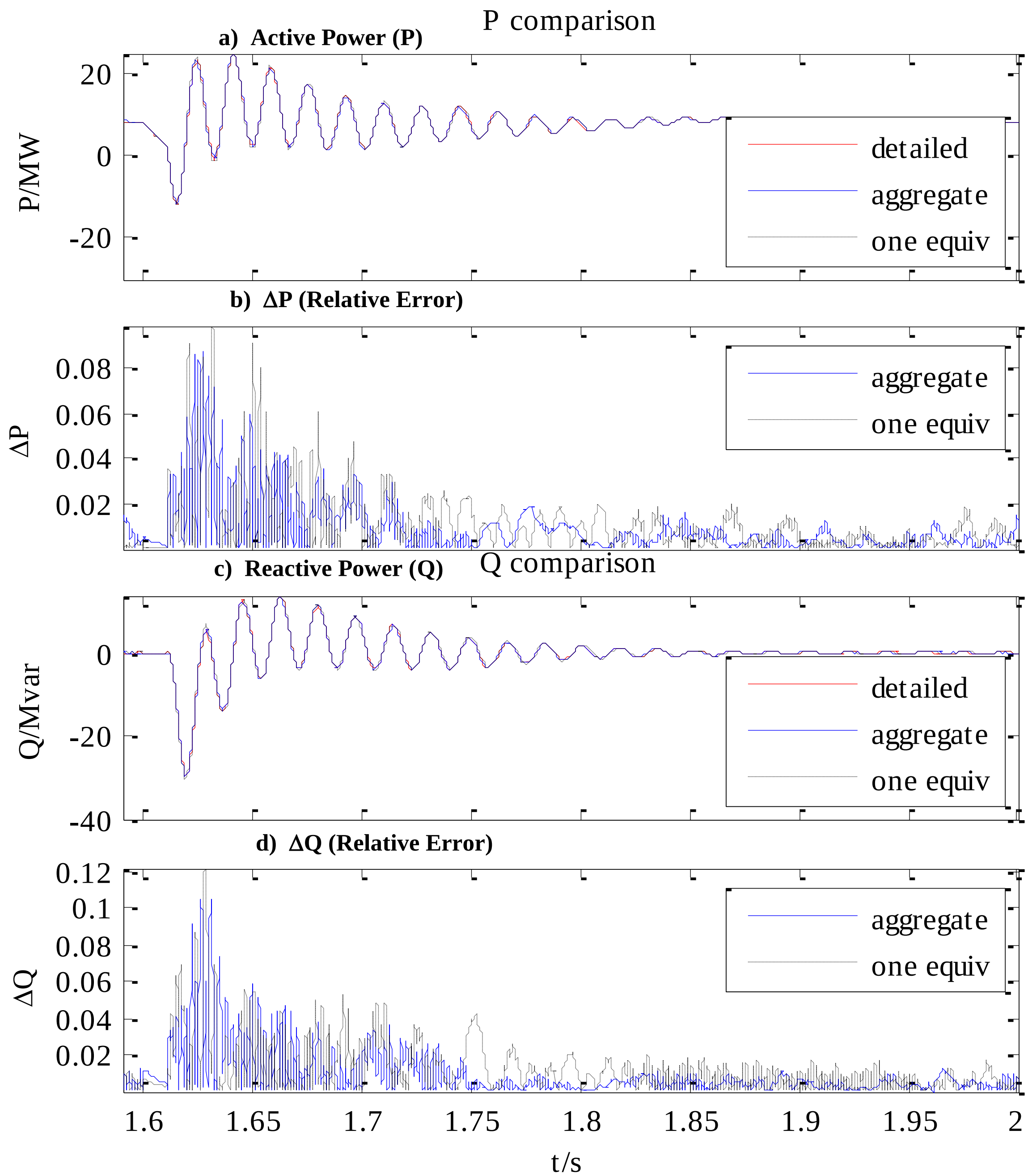

Figure 4-11 Comparison Simulation Results Between Detailed and Aggregated Model of 2 DFIGs of Different Parameters

Table 4-7 gives the root mean square relative error (RMSE) from Figure 4-11 for the proposed aggregate model and one- equivalent model when compare with the detailed model. The RMSE is calculated below as in (49). Here, $t_1$is the start instant of the transient, and t_2 is the end time of the transient. In this case, $t_1 = 1.6\ s$ and $t_2 = 2.0\ s$, and $S = \sqrt{P^2_{steady-state} + Q^2_{steady-state}}$.

$$RMSE_P = \left[\frac{\int_{t_1}^{t_2}\left(\frac{P_{aggregate} - P_{det\,ailed}}{S}\right)^2 dt}{t_2 - t_1}\right]^{\frac{1}{2}}$$

$$RMSE_Q = \left[\frac{\int_{t_1}^{t_2}\left(\frac{Q_{aggregate} - Q_{det\,ailed}}{S}\right)^2 dt}{t_2 - t_1}\right]^{\frac{1}{2}} \tag{49}$$

Table 4-7 Comparison of Simulation Errors

	Active power P_RMSE	Reactive power Q_RMSE
Aggregate model	1.5 %	1.7%
One-equivalent model	1.8%	1.92%

The comparison results suggest that the detailed model and the aggregate model have close transient responses with similar oscillation frequency and damping and reach the same steady state after the transients. There are minor differences giving an RMSE of 1.5% and 1.7% for P and Q, due to the aggregation approximation. Here the one-equivalent model from previous literature also gives fairly accurate results, with the error being only marginally larger.

4.5.3 Performance of Aggregate Model with Different Loadings of Individual DFIGs

Now consider the case in Table 4-8 where the two identical DFIGs have different incident wind speeds (1.07 pu and 0.88 pu), and consequently different rotor speeds ω_r and different power levels P_m according to the MPPT curve from Figure 4-9.

Table 4-8 The Operating Points of the DFIGs ($V_w\ base\ =\ 11\ m/s,\ P_{base}\ =\ 5.6\ MW$)

DFIG #	Wind speed Vw (pu)	Rotor angular speed ω_r (p.u.)	Prime mover power P_m (pu)
DFIG1	1.07	1.1	0.76
DFIG2	0.88	0.96	0.41

Figure 4-12 shows the comparison results of the transient responses for the detailed and aggregated model models (proposed and 'equivalent') for a 10 ms fault applied at 1.6 s.

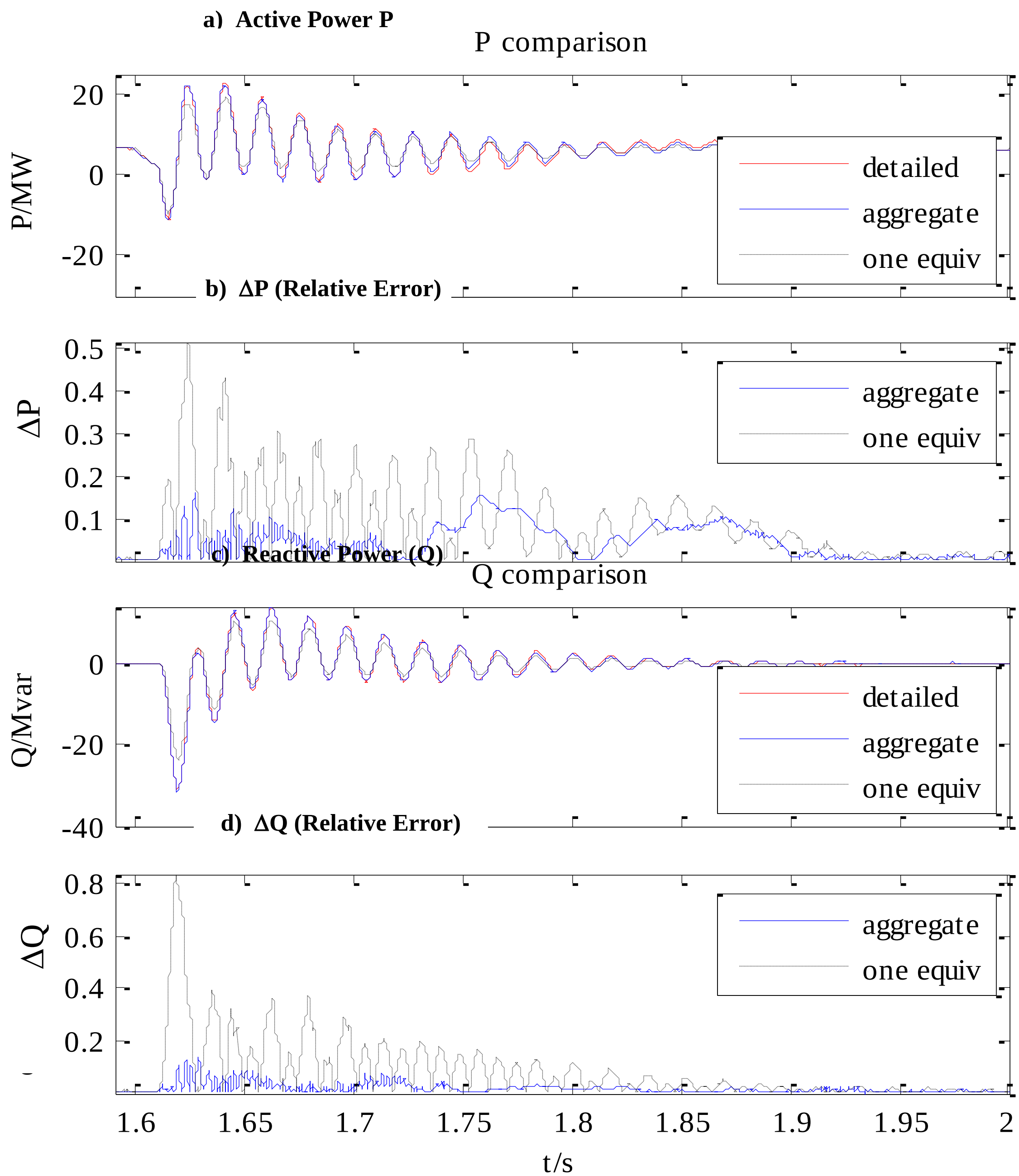

Figure 4-12 Comparison Simulation Results Between Detailed and Aggregated Model of 2 DFIGs of Different Rotor Speeds

Table 4-9 Errors due to Aggregation

	Active power P_RMSE	Reactive power Q_RMSE
Aggregate model	5.93%	2.7%
One equivalent model	13%	14.7%

Table 4-9 shows the corresponding root mean square errors (RMSE) between the detailed and aggregate models. Based on that, that the RMSE for P and Q of the proposed aggregate model are less than 6% and 2.7 % respectively for rotor speed variations of about 20%. The corresponding errors for the one-equivalent used in previous literature are significantly larger, at 13% and 14.7%. The close comparisons show that the aggregation method is capable of handling DFIGs with different individual loadings.

4.5.4 Performance of Aggregate Model with a Larger System

Further validation simulations for a wind farm consisting of 10 DFIGs are performed. The DFIGs have identical structures while having different incident wind speeds as shown in Table 4-10 due to effect of upwind turbines on downwind turbines' input wind speed which is called wake effect (explained in Chapter 2), again resulting in different state space matrices for each DFIG.

Table 4-10 Incident Wind Speed on Each Turbine

DFIG No.	1	2	3	4	5	6	7	8	9	10
$V_w\ (m/s)$	12.2	12	11.5	11.2	10.7	10.4	10.3	10.3	10.2	10.2

DFIG parameters and wind farm collector system impedances are given in Section 4.5. The parameters of the aggregate DFIG wind farm are obtained using the recursive procedure of Section 4.4.3 and yield the parameters for the single aggregate wind farm. Figure 4-13 shows the real and reactive powers and ac voltage and windfarm current following a temporary three-phase to ground fault at PCC bus with duration of 100 ms.

The results in Figure 4-13 indicate that the aggregated model maintains the same power flow into the PCC bus as the detailed model and has an essentially identical transient response. During the fault, a certain amount of reactive power is injected into the grid side from the wind farm with peak value of 19.6 Mvar and average value of 10.2 Mvar. It takes around 240 ms after fault clearance for the model to reach its new steady state. The computation time is also significantly reduced as will be shown in the next section. These examples validate that the aggregated model retains the major collective oscillation modes of the original detailed system in the transient process and has the same steady response. The comparison was limited to a 10-machine case due to the large simulation time for the EMT model of the detailed system required for the validation. However, any number of machines can be included in the aggregate. Note that in an actual windfarm the local conditions at each DFIG may be quite different, with the possibility that one or more DFIGs may even have disconnected due to violation of its operating limit, which is not represented in the aggregate. Hence the aggregate model is not intended for protection design of individual DFIGs, as the identity of individual DFIGs is not maintained. However, if required, it is also possible to preserve a limited amount of granularity in the model. For example, a windfarm with 100 DFIGs could be represented with say, 5 aggregate models of 20 machines each. This would still result in significant computational savings as compared with a full detailed model.

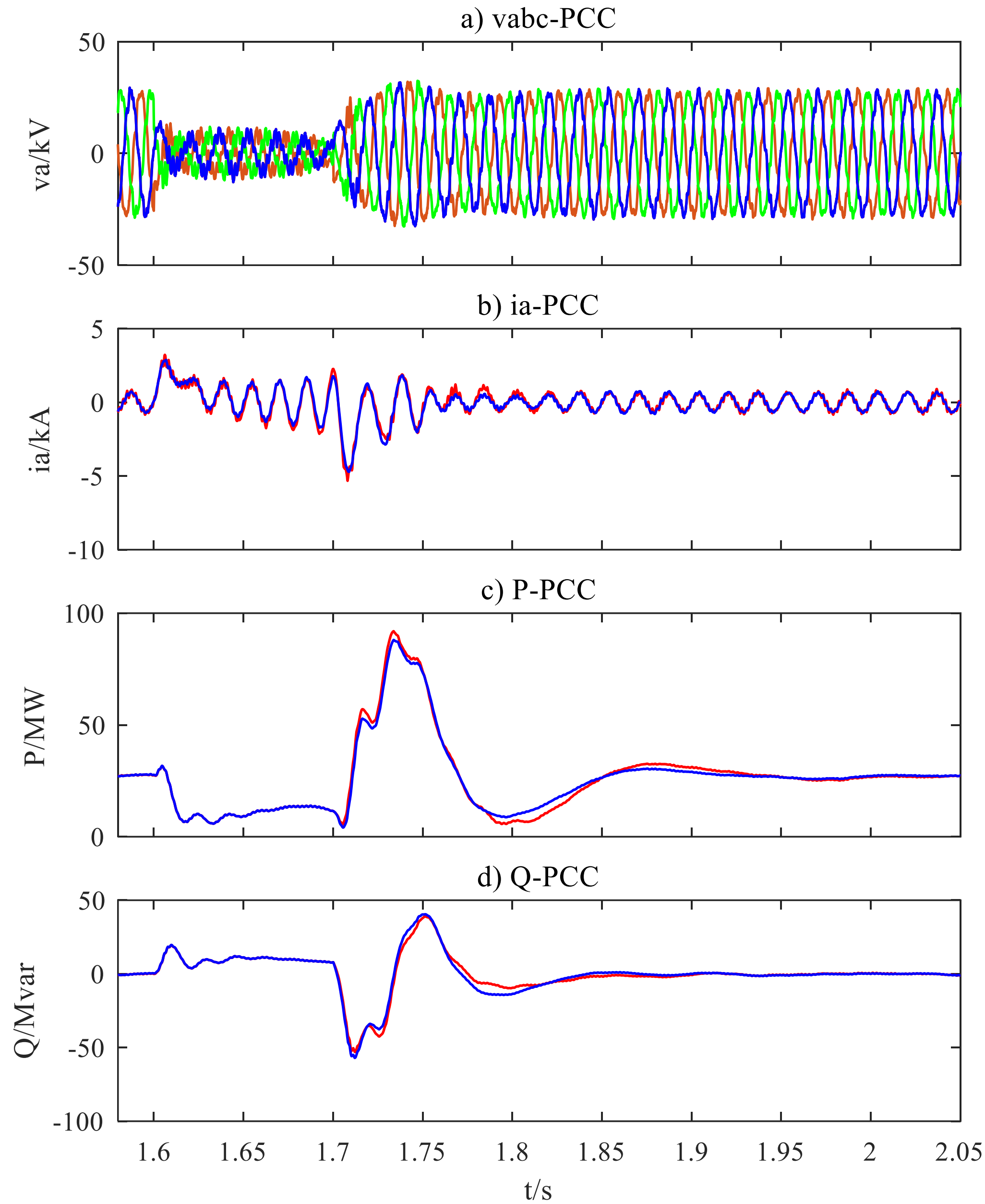

Figure 4-13 Comparison Simulation Results from PSCAD (Red Curves are from Detailed Model, Blue Ones are from Aggregate Model)

4.5.5 Computational Savings

As the multiple DFIGs are reduced to a single DFIG, there is a significant reduction in simulation times. Table 4-11 shows the simulation times for a windfarm with 2, 3 and 10 DFIGs on a PC with an Intel Core i5-6200U CPU running at 2.30 GHz. Note that although the simulation time increases significantly from 45 s for a single machine to 7235 s for a 10-machine windfarm. Of course, the simulation time for the single machine aggregate representation remains essentially constant in the range 45-48, which is to be expected due to the fact that the aggregate only contains one machine. The speedup factor for 2 machines is 7.8 and increases to over 150 with 10 machines. With hundreds of machines, the time savings will be significantly larger.

Table 4-11 Simulation Time Comparison

Model	Detailed model simulation time (s)	Aggregate model simulation time (s)	Speedup factor
1 DFIG system	45	45	1
2 DFIG system	351	45	7.8
3 DFIG system	879	48	18.3
10 DFIG system	7235	48	150.7

4.6 Comparison of Simulation Responses for a Case Study with 9 Wind Turbines

As previously discussed in Section 4.1, previous authors have introduced different methods for aggregating wind farms [10], [52], all with the aim of identifying an appropriate aggregated model. In this section, we compare the responses at the point of common coupling (PCC) for two commonly used aggregated models from [77] with the proposed aggregated model, as well as a detailed model for a 9 DFIG wind farm. The specifics for each DFIG, turbine model, and wind turbine mechanical power were explained in Section 4.5. The wind farm under study contains three groups, each with three WTs, all interconnected with the grid at the PCC, as illustrated in Figure 4-14. The turbines within a group are daisy-chained with underground cables spanning 800 ft, and finally connected to the PCC through an overhead line of varying length, as indicated in Figure 4-14. The standard data employed for calculating the resistance (R) and reactance (X) of the underground cables and overhead lines are sourced from [21] and detailed in Table 4-12.

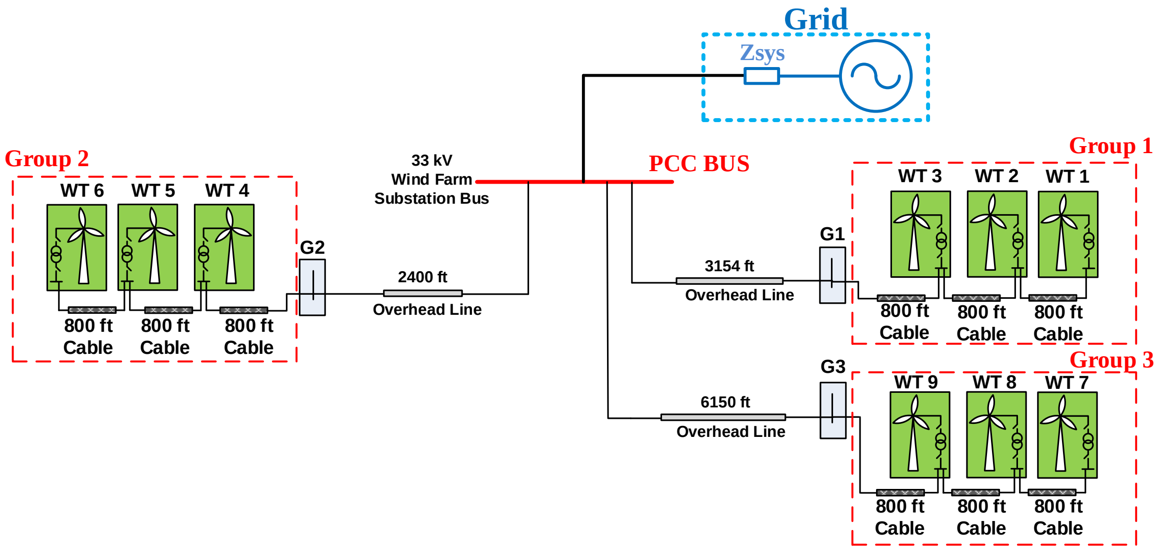

Figure 4-14 Detailed Model Wind Farm Layout with 9 DFIGs

Table 4-12 Data Used for Collector System Within Wind Farm

	R (pu/ft)	*X (pu/ft)*
Underground Cables	9.662×10^{-6}	7.729×10^{-6}
Overhead lines	1.865×10^{-6}	9.920×10^{-6}

To account for wind variations across different locations and the impact of wake effects on downwind turbines, distinct input wind speeds are attributed to each turbine. The corresponding output powers for each turbine are documented in Table 4-13.

Table 4-13 Turbine Output Power Within Wind Farm ($P_{rated} = 5\ MW$)

Turbine No.	*Active Power P (MW)*	*Active Power P (pu)*
WT 1	5	1
WT 2	4.2	0.84

WT 3	4	0.8
WT 4	4	0.8
WT 5	3.5	0.7
WT 6	3.5	0.7
WT 7	5	1
WT 8	4.2	0.84
WT 9	4	0.8

To conduct this comparison, two distinct aggregation methods described in [77] were chosen: i) Multi-machine model (MMM) representation and ii) Full aggregated model (FAM) representation. In the FAM representation, all wind turbines (WTs) within the wind farm, along with their internal electrical networks, are aggregated into a single equivalent WT with a corresponding internal electrical network. In contrast, the MMM approach allows the entire wind farm to be represented by multiple equivalent machines. Reference [21] proposed the MMM as a solution for taking into account the large diversity in WT types, wind speeds, impedances of the lines that connect a group of WTs to the PCC, step up transformer sizes and short circuit capacity levels for the WTs within the farm. WTs positioned in the same row within the farm experience similar incoming wind conditions, making MMM representation a practical means of aggregating each row together [77]. For this case study, the MMM and one equivalent WT (i.e., FAM) of the wind farm of Figure 4-14 are shown in Figure 4-16(a) and (b). The equivalent step-up transformer ($Z_{TS_{eq}}$) and collector system equivalent (Z_{Seq}) for the models also calculated using an analytical approach proposed by the national renewable energy laboratory (NREL) to aggregate the collector system given in [21]. The NREL method can be explained with help of the wind farm example in Figure 4-15 consisting of different types of turbines of different sizes or types; e.g., WTs 1 and 2 are identical and also WTs 3 and 4 are identical. The voltage drop across the impedance Z_m of the m^{th} line segment in Figure 4-15 is $\Delta V_{Zm} = I_m Z_m = \left(\frac{S_m}{V}\right) Z_m = \left(\frac{P_m}{V}\right) Z_m$ based on the assumption that most wind turbines are compensated to have a very close unity power factor and the apparent power S_m can be substituted by the rated power P_m of the m^{th} wind turbine. By calculating the power loss in each line segment (i.e., $S_{Loss_{Z_m}} = \Delta V_{Zm} I_m^* = \frac{P_{Z_m}^2 Z_m}{V^2}$) and equating the total loss with losses calculated for equivalent circuit representation (i.e., Figure 4-15(b), the equivalent collector impedance Z_{Seq} for the group becomes:

$$Z_{Seq} = \frac{\sum_{m=1}^{n} P_{Z_m}^2 Z_m}{P_{Z_n}^2} \tag{50}$$

where P_{Z_m} is the total power flow in the line segment represented by Z_m.

With this process the wind farm representation becomes as in Figure 4-16(a), where there are 3 groups of 3 WTGs each. The three parallel groups can be converted into a single “FAM” equivalent as in Figure 4-16(b). The equivalent transformer impedance $Z_{TS_{eq}}$ of the single WTG model (i.e., FAM) can be obtained as a weighted sum of the individual transformer impedances $Z_{TS_{eq_j}}$ based on the individual group powers [21]. The voltage drop across each transformer can be written as $\Delta V_{Z_{T_m}} = I_m Z_{T_m} = \left(\frac{S_m}{V}\right) Z_{T_m} = \left(\frac{P_m}{V}\right) Z_{T_m}$.

So, losses in individual transformer will be $S_{Z_{T_m}} = \Delta V_{Z_{T_m}} I_m^* = \frac{P_m^2 Z_{T_m}}{V^2}$. Similarly, by equating the total transformer loss with transformer losses calculated for wind farm equivalent representation (i.e., Figure 4-15(b)), the equivalent impedance $Z_{TS_{eq}}$ for the group becomes:

$$Z_{TS_{eq}} = \frac{\sum_{m=1}^{n} P_m^2 Z_{T_m}}{\left(\sum_{m=1}^{n} P_m\right)^2} \tag{51}$$

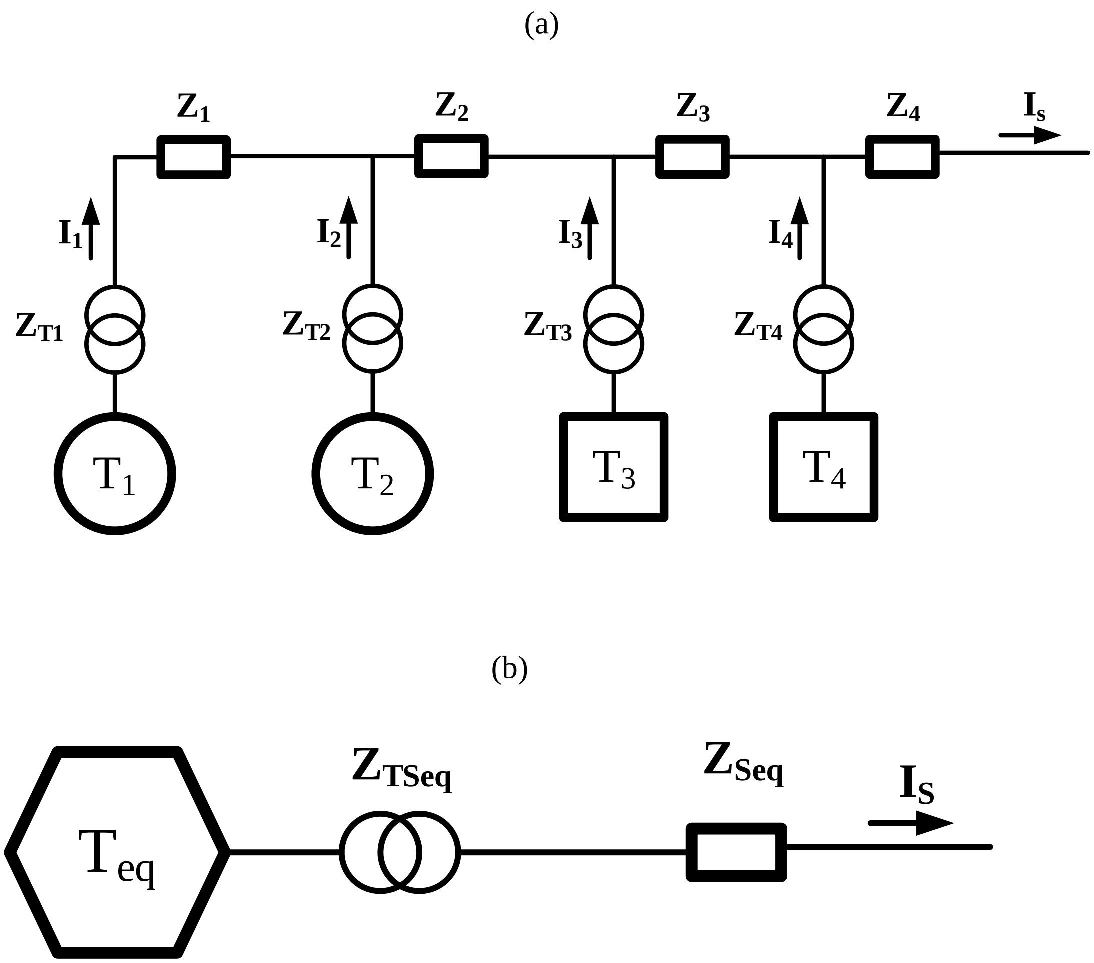

Figure 4-15 Equivalencing Four Turbines: (a) Daisy-chain Representation, (b) Equivalent Circuit Representation [21]

In the wind farm considered for this comparison described in Section 4.6, the equivalent impedance results were calculated and are shown in Figure 4-16. For the ac grid network, as system with SCR of 10 and X/R ratio of 7 was considered.

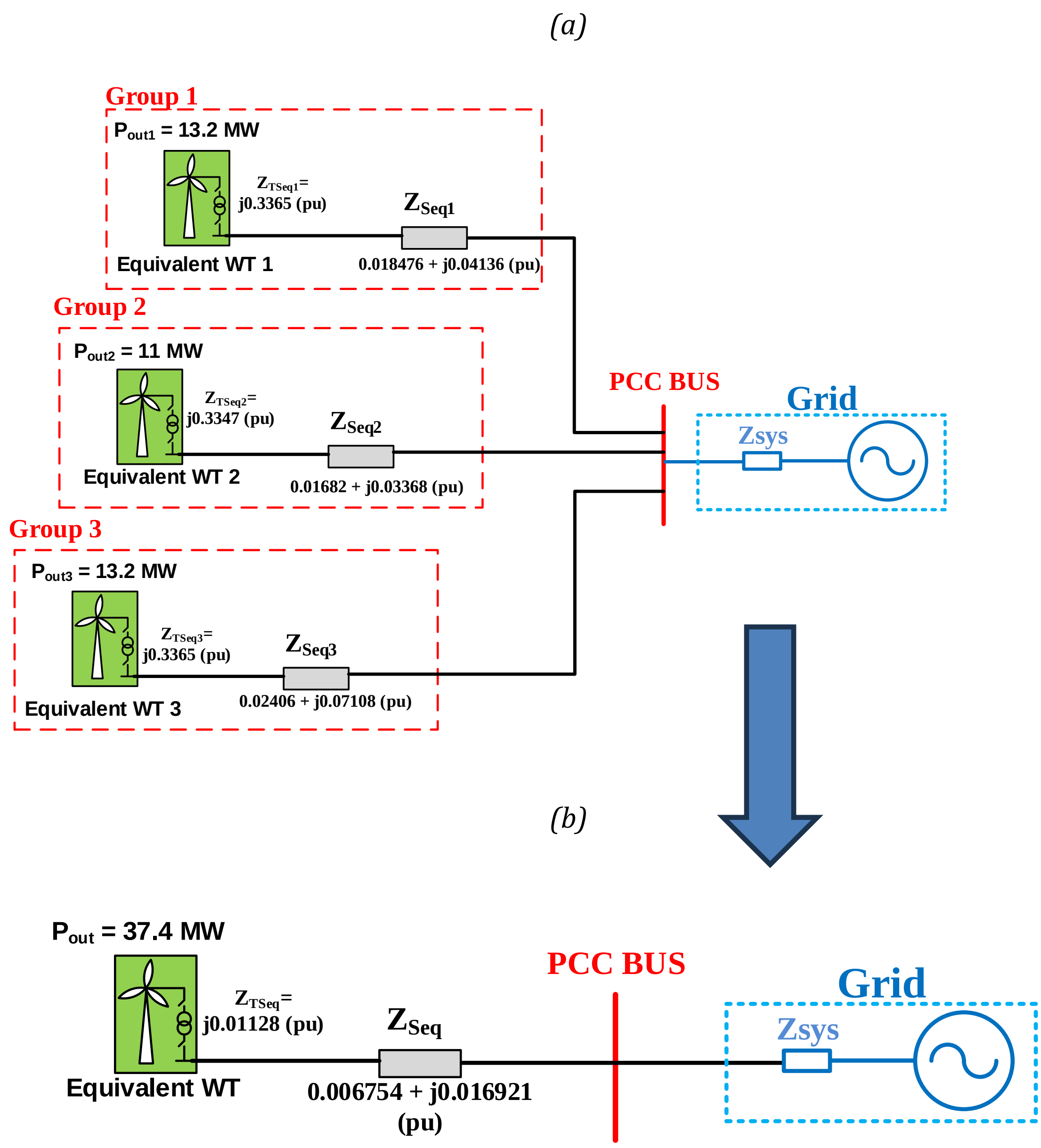

Figure 4-16 Aggregated Models Representation: a) Multi Machine Model (MMM), b) Single WTG Equivalent (FAM)

The active and reactive powers, and RMS voltage at PCC following a temporary single-phase to ground fault at 2 s at PCC bus with duration of 100 ms are shown in Figure 4-17 to Figure 4-20. Each figure shows the results for detailed model (DM), full aggregated model (FAM), multi machine model (MMM) representation. In addition, results for the proposed aggregated model (previously explained in Section 4.4) representing the whole wind farm with one equivalent machine or three equivalent machines are depicted to show a comparison between different models' response. The main differences between the proposed method and MMM are: i) in the proposed method, the model takes in the parameters of machines that are going to be aggregated and provides an aggregated model with equivalent parameters and input wind speed. However, in MMM only total output power of WTs are considered for getting same steady state results. ii) The method for equivalencing the collector system is also different. For the MMM, an analytical approach is described and in the equivalent derivation procedure, the equivalent collector circuit is calculated based on having the same apparent power losses (real power losses and reactive power losses) between detailed model and equivalent circuit representation as was explained in Section 4.6. Detailed methodology for the MMM can be found in [21]. For the proposed method explained in Section 4.4.1, it is based on the equivalent WTG having the same output power as the sum of the individual WTG powers, the same received power at the PCC bus and the same PCC bus voltage in the detailed and equivalent model.

The results depicted in Figure 4-17 showing the active power output reveals that the proposed aggregated model employing a representation of 3 machines closely mirrors the transient response of the detailed model, with a maximum relative error of 0.0763 pu. The proposed aggregated model with a single machine model exhibits a similarly shaped response, but has a larger relative error (0.3912 pu peak). Figure 4-18 compares the real powers for the detailed model and the equivalents obtained by the previously published approaches FAM and MMM [21], [77]. The MMM has a slightly smaller maximum error (0.3871 pu) as compared with the FAM (0.6273 pu), and they are comparable in magnitude with the maximum error for the proposed single machine aggregate (0.3912 pu), but much larger than that with the proposed method for getting a 3-machine representation (0.0763 pu). Figure 4-19 shows a comparison figure of detailed modelling and the two models with the proposed equivalencing technique (3-machine and 1-machine) as well as the FAM and MMM models on a single plot for visual comparison. Figure 4-20 shows the PCC rms voltages for the same 5 models. All models closely match the detailed model, though the FAM has a marginally lower voltage during the voltage dip.

Overall, the proposed aggregated model employing 3 machines demonstrates significantly precise transient response, outperforming all other models. However, the proposed model representing the WF with 1 equivalent machine still provides a reasonable level of accuracy which can reduce the computational time compared to using 3-machine equivalent model.

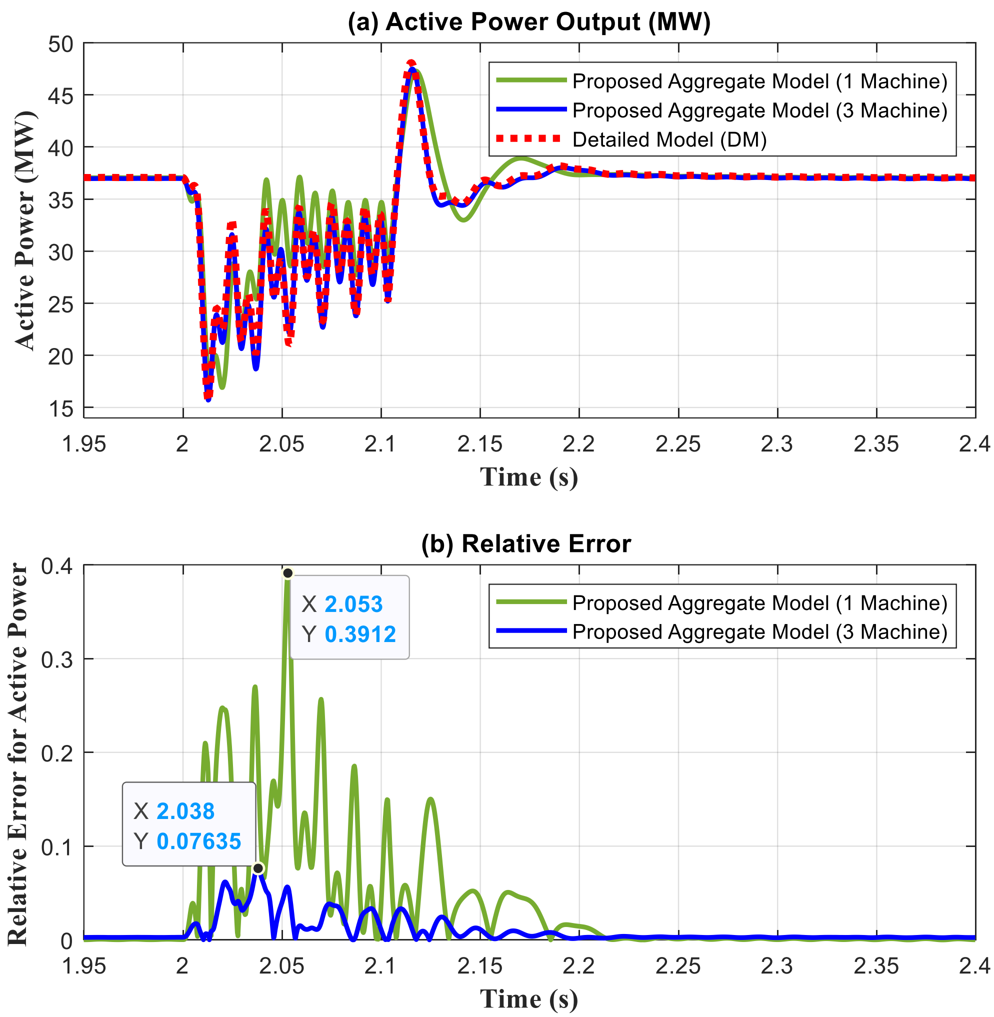

Figure 4-17 PSCAD Simulation Results Comparing Detailed Model and Proposed Aggregate Models for Active Power Output at PCC in Wind Farm Layout with 9 DFIGs (represented in Figure 4-14)

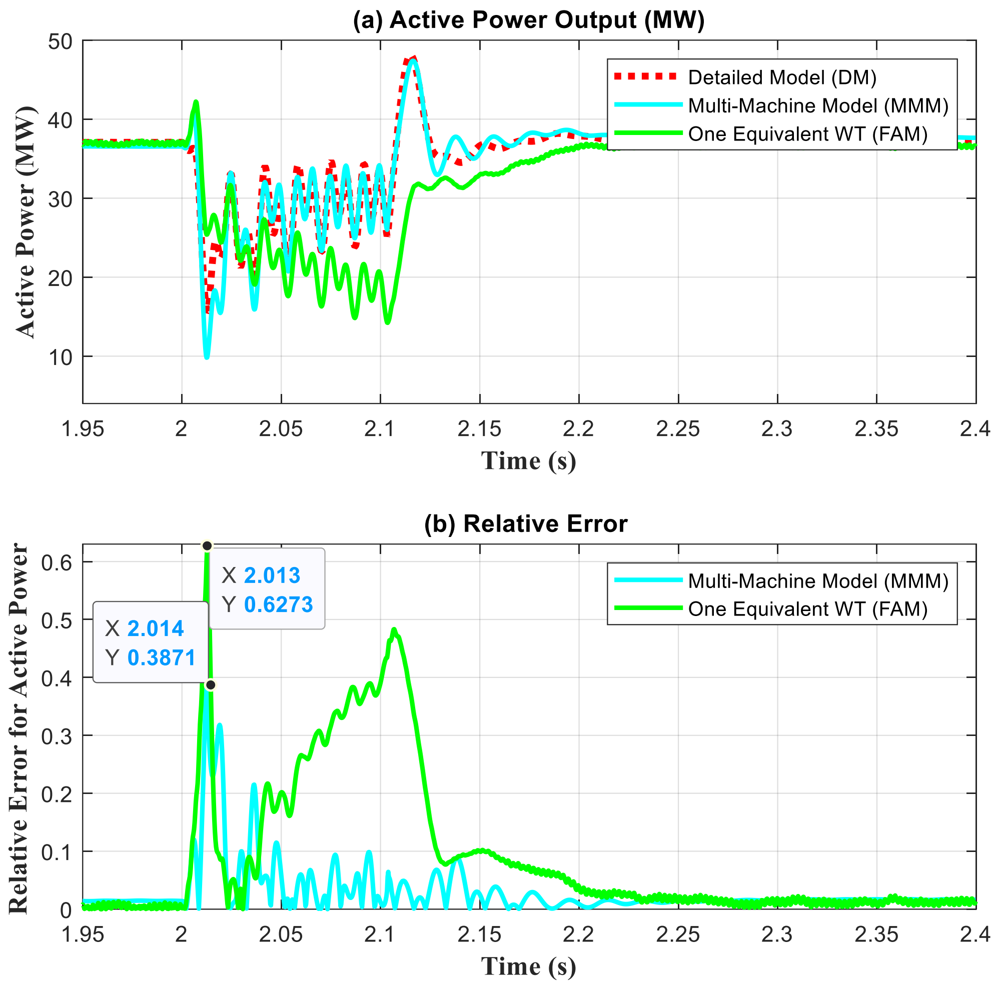

Figure 4-18 PSCAD Simulation Results Comparing Detailed Model, MMM and FAM for Active Power Output at PCC in Wind Farm Layout with 9 DFIGs (represented in Figure 4-14)

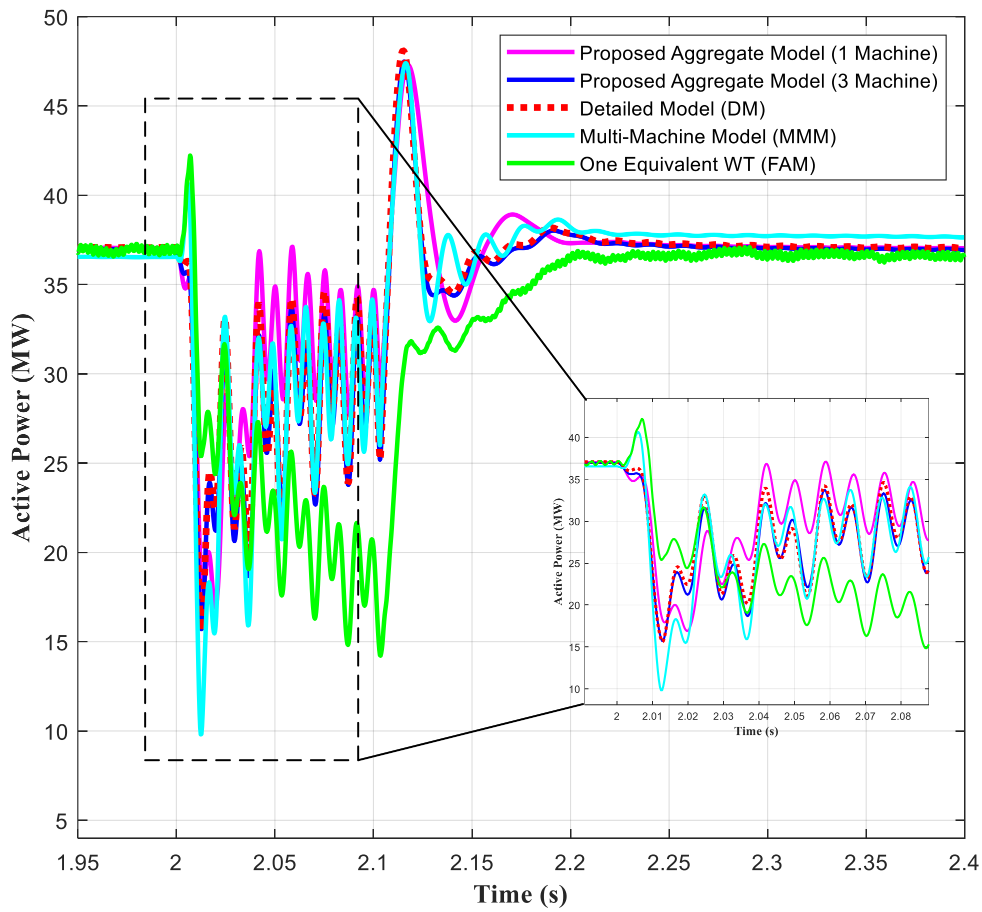

Figure 4-19 PSCAD Simulation Results for Comparing Results of All Models Investigated Overlaid Together for Active Power Output at PCC in Wind Farm Layout with 9 DFIGs (represented in Figure 4-14)

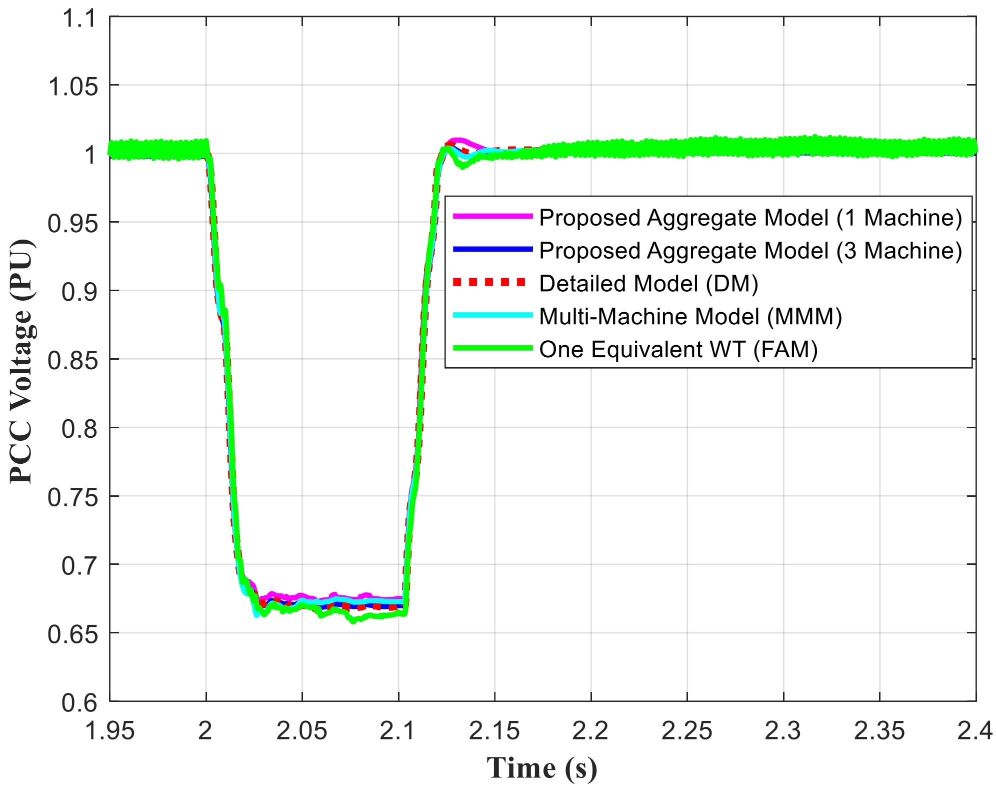

Figure 4-20 Comparison Simulation Results from PSCAD for RMS Voltage at PCC

4.7 Sensitivity Analysis for Proposed Aggregated Model

In order to investigate the accuracy of the proposed aggregation model against machine parameter differences, two DFIGs connected directly to PCC through $Z_1 = 0.1 + \mathrm{j}0.376\ \Omega$ *and* $Z_2 = 0.3 + \mathrm{j}1.131\ \Omega$ were considered as depicted in Figure 4-21. The equivalent impedance (Z_{eq}) and parameters for the aggregated DFIG are calculated using the proposed method explained in Section 4.4. For the ac network, it is assumed that short circuit ratio (SCR) is 5 and $Z_{sys} = 0.56 + j3.920\ \Omega$.

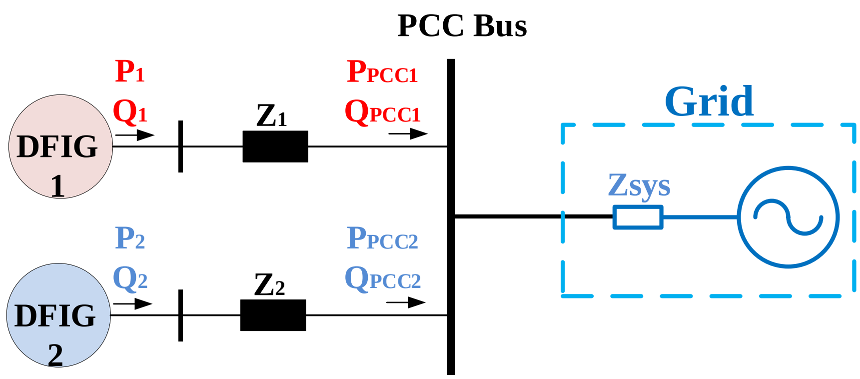

(a) Two DFIGs in parallel

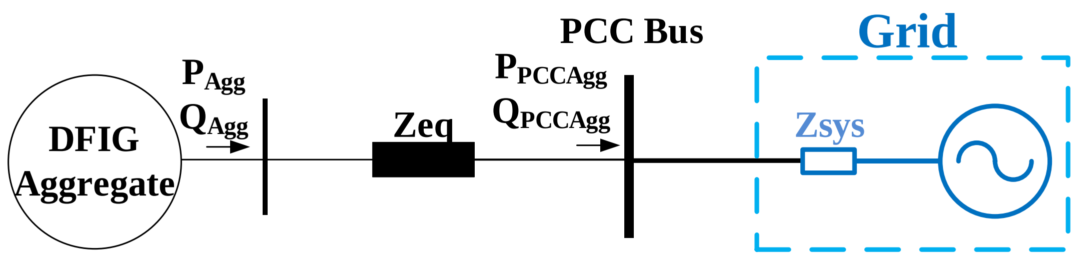

(b) Aggregate Model with Equivalent Impedance Z_{eq}

Figure 4-21 Two DFIG Model and Aggregated Model

The machines' parameters in this sensitivity analysis are considered as in Table 4-14. As reported, in the aggregation calculations, each DFIG has identical parameters. In conducting the sensitivity analysis one or more specific parameters of DFIG2 are scaled with a parameter k, selected in the interval [0.5, 1.5]. For instance, having k = 0.5 when investigating sensitivity to stator resistance (r_s), means considering r_s for DFIG1 to be 50 % of that of DFIG2, and having k = 1, means r_s for both DFIGs are the same.

Table 4-14 DFIGs Parameters and Operating Points (Base case, Identical DFIGs)

Base Case Parameters	*DFIG 1 and DFIG 2*	
Rating/MVA	5.5	
r_s (stator resistance)/p.u.	0.0054	
r_r (rotor resistance)/ p.u.	0.00607	
L_m (mutual inductance)/ p.u.	4.5	
L_{sl} (stator leakage inductance)/ p.u.	0.1	
L_{rl} (rotor leakage inductance)/ p.u.	0.11	
Operating Points	*DFIG 1*	*DFIG 2*
ω_r (rotor rotating velocity)/ p.u.	1.1	0.95
P_{DFIG} (Active Power_Operating Point)/MW	4.2	3.6
Q_{DFIG} (Reactive Power_Operating Point)/Mvar	0	0

There are three different errors that are used to compare the proposed aggregate model against simple model representation from references [16], [17] (referred to as "simple"). The definition of these errors for active (P) and reactive (Q) output powers are as follows.

1- Relative Error:

$$RelativeError_P = \left|\frac{P - P_{Detailed\ Model}}{S}\right|$$

$$RelativeError_Q = \left|\frac{Q - Q_{Detailed\ Model}}{S}\right|$$

2- Root Mean Square Relative Error (RMSE):

$$RMSE_P = \left[\frac{\int_{t_1}^{t_2}(\frac{P - P_{Detailed\ Model}}{S})}{t_2 - t_1}\right]^{\frac{1}{2}}$$

$$RMSE_Q = \left[\frac{\int_{t_1}^{t_2} (\frac{Q - Q_{Detailed\ Model}}{S})}{t_2 - t_1} \right]^{\frac{1}{2}}$$

3- Average Relative Error (AE):

$$AE_P = \frac{1}{t_2 - t_1} \int_{t_1}^{t_2} \left| \frac{P - P_{Detailed\ Model}}{S} \right| dt$$

$$AE_Q = \frac{1}{t_2 - t_1} \int_{t_1}^{t_2} \left| \frac{Q - Q_{Detailed\ Model}}{S} \right| dt$$

4- Maximum Error

where, t_1 is the beginning moment of transient, and t_2 is the end moment of transient to calculate error. In all cases, $t_1 = 1.60\ sec$ and $t_2 = 2.00\ sec$ and $S = \sqrt{P_{Steady-State}^2 + Q_{Steady-State}^2}$.

4.7.1 Stator Resistance Sensitivity

In order to investigate accuracy of the proposed aggregation model due to differences in stator resistance (r_s) parameter for two DFIGs shown in Figure 4-21, the stator resistance of DFIG 1 is maintained at r_s, whereas that of DFIG 2 is set to $r_{s2} = K\ r_s$. This factor K is varied in the range [0.5,1.5], in steps of 0.1.

The simulations results comparing output active power (P) and reactive power (Q) of the proposed aggregate model and simple model are displayed in Figure 4-22. The results for eleven different K values were recorded, and the Average Relative Error (AE) and Root Mean Square Relative Error (RMSE) were shown in Figure 4-22. Maximum error comparison for P and Q is shown in Figure 4-23.

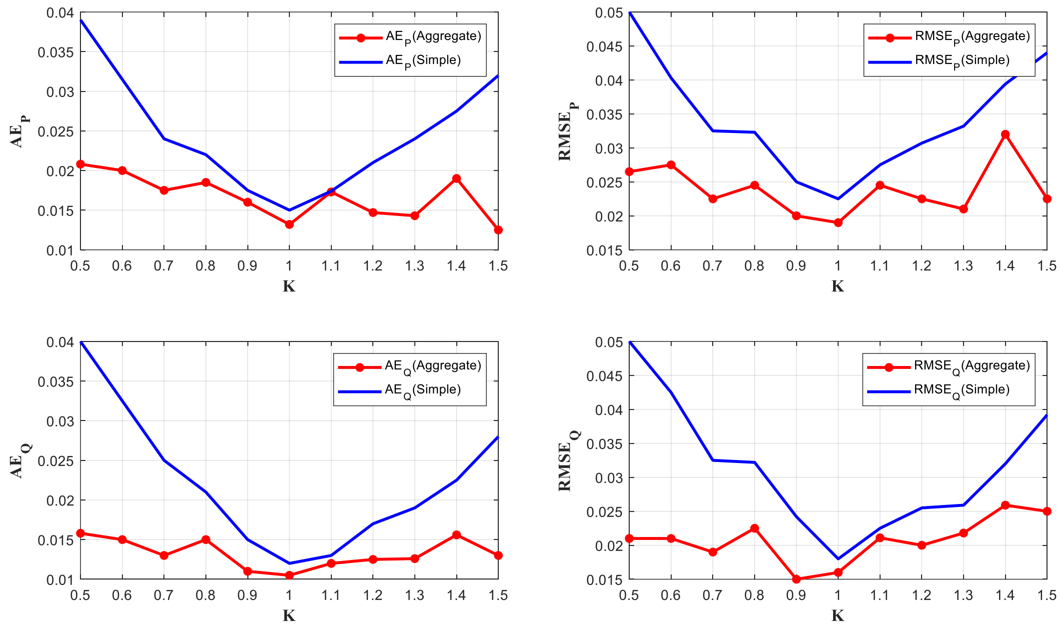

Figure 4-22 RMSE and AE Sensitivity Analysis Considering Different Stator Resistance for DFIG 2 (r_{s2}) by Changing K

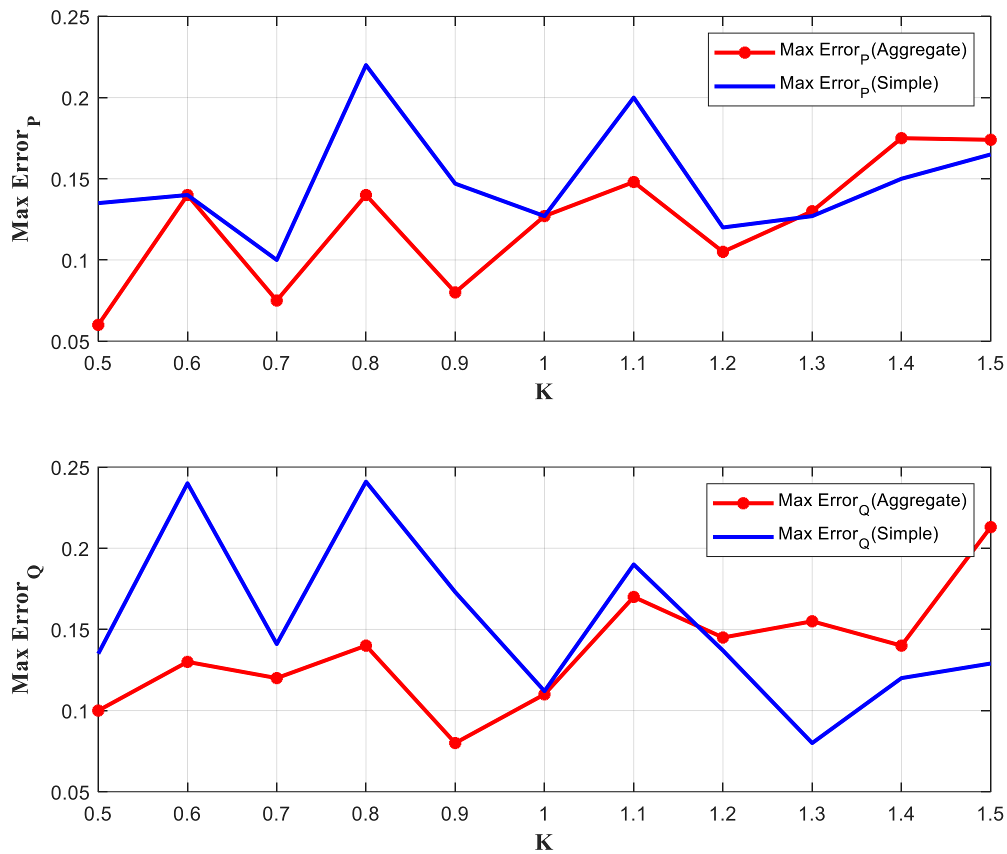

Figure 4-23 Maximum Error Comparison Considering Different Stator Resistance for DFIG 2 (r_{s2}) by Changing K

It could be seen that from results:

- Within the investigated range (i.e., changing r_{s2} by multiplying factor K), the aggregate model is more accurate than the simple model as the RMSE and AE values for P and Q of proposed aggregate model were lower compared to simple model.
- The maximum error of the proposed aggregate model for P and Q is getting larger with increasing K, and for k greater than 1.3, it is larger than the simple model. It

means using proposed aggregated model for aggregating 2 DFIGs with stator resistance parameter's difference more than 30 % will result in a large error and it is not recommended.

4.7.2 Stator Leakage Inductance Sensitivity

In order to investigate how accuracy of the proposed aggregation model change due to a difference in stator leakage inductances between the two DFIGs, the stator leakage inductance of DFIG 2 is set $L_{sl2} = K * L_{sl1}$ with the scaling factor $K \in \{0.5, 0.6 \ldots 1.5\}$. The corresponding outputs of active power (P) and reactive power (Q) as a function of K of the proposed aggregate and simple model representations are illustrated in Figure 4-24. The AE and RMSE are shown in Figure 4-24; and the Maximum error comparisons are shown in Figure 4-25.

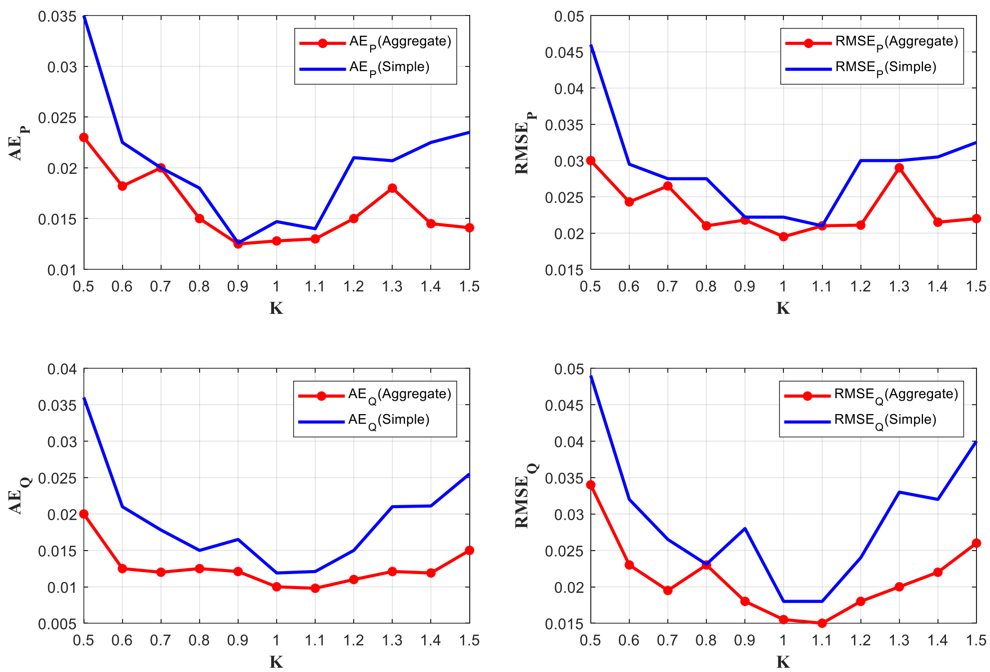

Figure 4-24 RMSE and AE Sensitivity Analysis Considering Stator Leakage Inductances for DFIG 2 (L_{sl2}) by Changing K

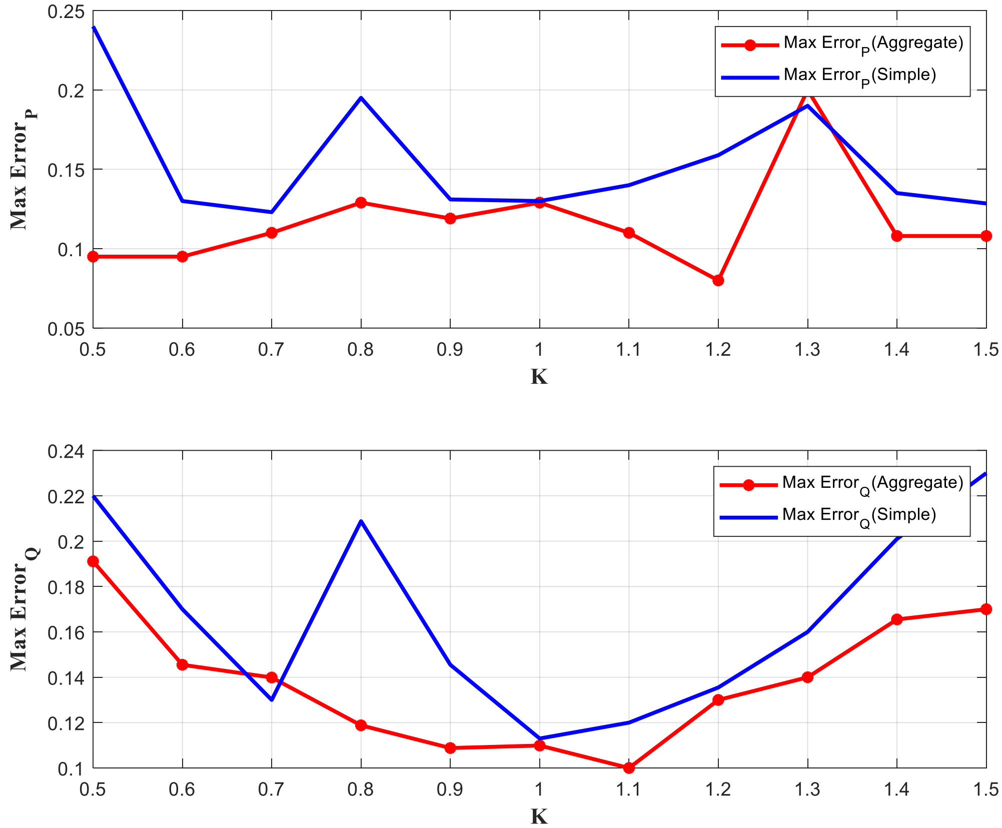

Figure 4-25 Maximum Error Comparison Considering Stator Leakage Inductances for DFIG 2 (L_{sl2}) by Changing K

It is evident from results that:

- Within the investigated range the aggregate model is more accurate than the simple model as the RMSE and AE values for P and Q of proposed aggregate model were lower compared to simple model.
- By looking at RMSE for P, it is observed that there is not a significant difference between the aggregate and simple model except for $K = 0.5$. However, the RMSE of Q gets larger in the simple model by deviating k from 1 (either increasing or decreasing K). That means for the simulation cases considering the

difference of stator leakage inductance (L_{sl}) parameter for two DIFGs to be larger, the Q error for the aggregated model is lower compared to simple model.

- The maximum error of the proposed aggregate model for P and Q is smaller than simple model through the whole range of K.

4.7.3 Rotor Leakage and Stator Leakage Inductances Sensitivity

In this section, two parameters are simultaneously changed in order to investigate how accuracy of the proposed aggregation model changes. Therefore, rotor leakage inductance (L_{rl}) and stator leakage inductance (L_{sl}) are selected, and it is assumed to vary both rotor and stator leakage inductances L_{rl2}, L_{sl2} for DFIG 2. Thus $L_{rl2} = K * L_{rl1}$ and L_{sl2} =$K * L_{sl1}$, with $K \in \{1, 1.1, 1.2 ... 1.5\}$. The simulations absolute and root mean square errors for active power (P) and reactive power (Q) of the proposed aggregate model and simple model representation are depicted in Figure 4-26. The Maximum errors are compared in Figure 4-27.

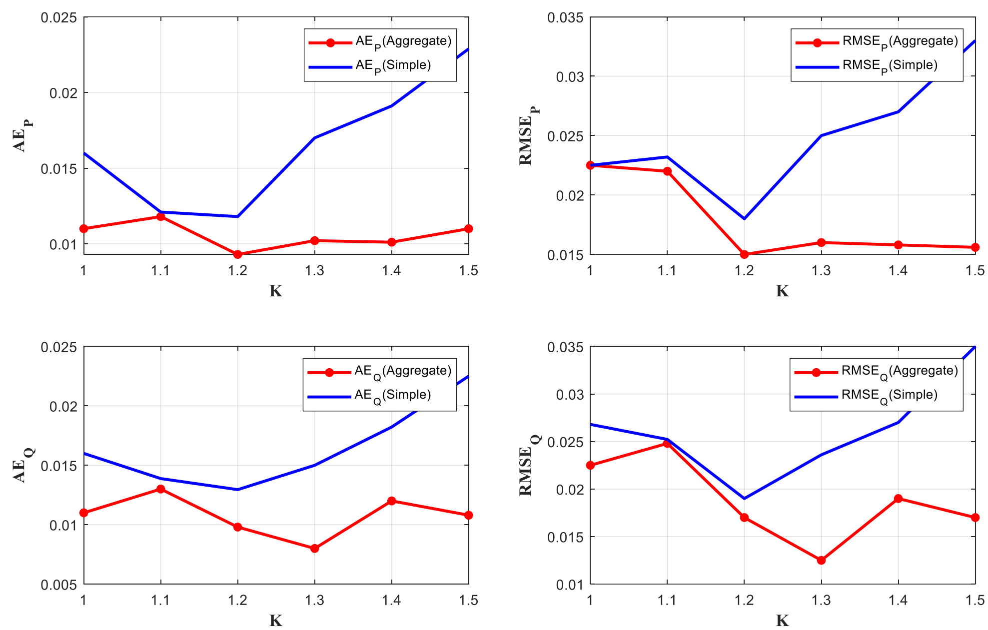

Figure 4-26 RMSE and AE Sensitivity Analysis Considering Different Rotor and Stator leakage Inductance for DFIG 2 (L_{rl2}, L_{sl2}) by Changing K

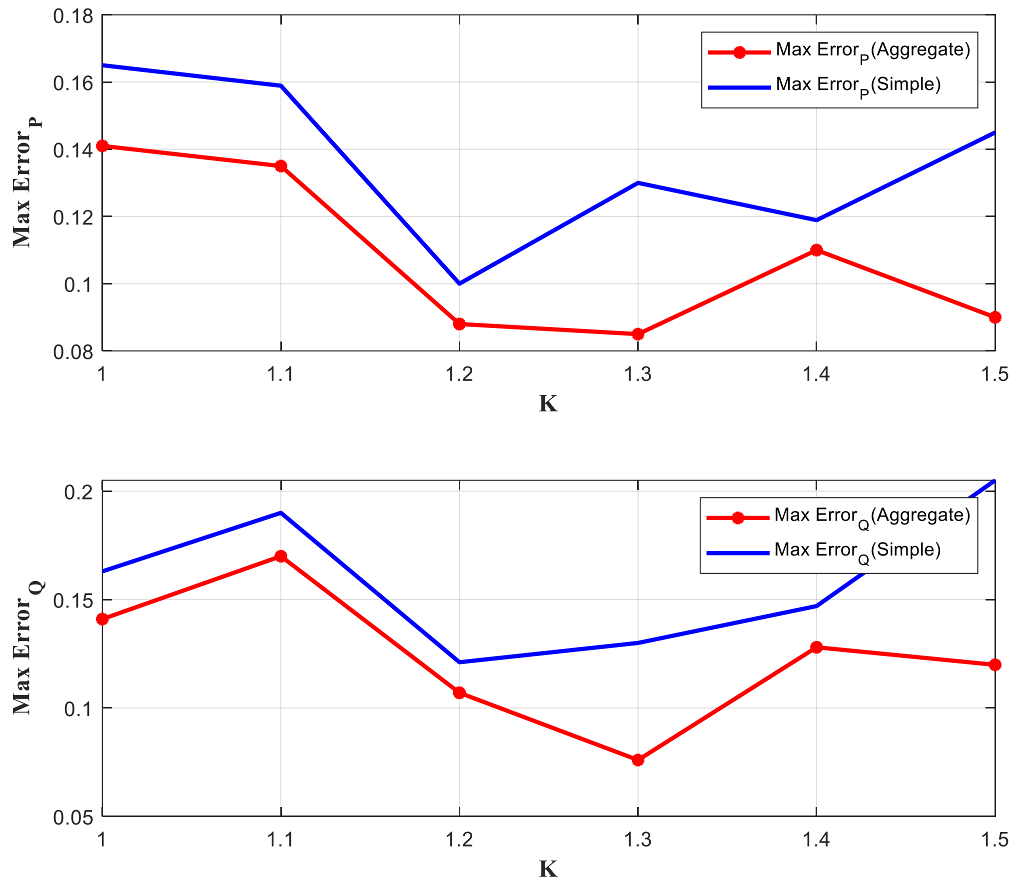

Figure 4-27 Maximum Error Comparison Considering Different Rotor and Stator leakage Inductance for DFIG 2 (L_{rl2}, L_{sl2}) by Changing K

It is observed from results that:

- Within the investigated range, the aggregate model is more accurate than the simple model as it results in lower RMSE and AE for both P and Q. Also, increasing K, the AE and RMSE errors increase, while in the aggregate model, they do not change significantly.
- The maximum error of the proposed aggregate model for P and Q is smaller than simple model through the whole range of K.

4.7.4 Rotational Speed Sensitivity

In this comparison, the rotational speed of DFIG 2 is set to $\omega_{r2} \in \{0.8, 0.9, 1, 1.1\}$ while the rotational speed of DFIG 1 is assumed to be fixed at $\omega_{r1} = 1.1\ pu$. It should be noted that for this WTG, nominal output power is achieved at ω_r equal to 1.1 pu.

The AE and RMSE errors in the output active power (P) and reactive power (Q) of the proposed aggregate model are illustrated in Figure 4-28; and the Maximum errors are shown in Figure 4-29.

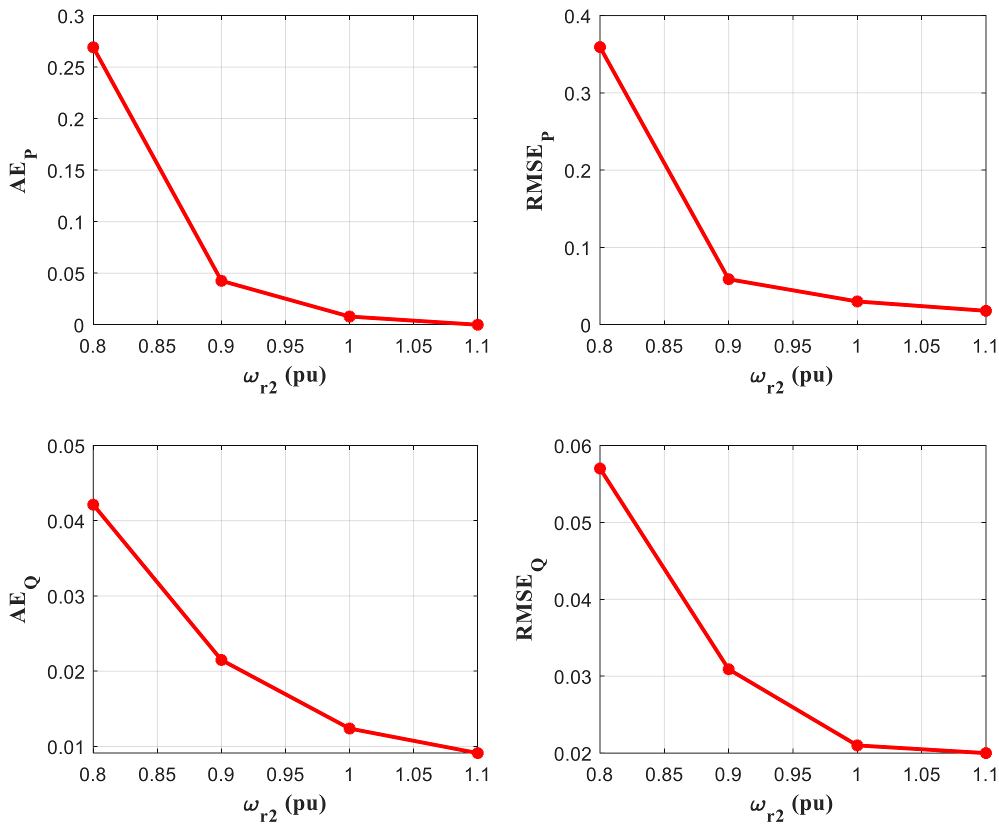

Figure 4-28 RMSE and AE Sensitivity Analysis Considering Different Rotational Speed (ω_r) for DFIG 2 (ω_{r2})

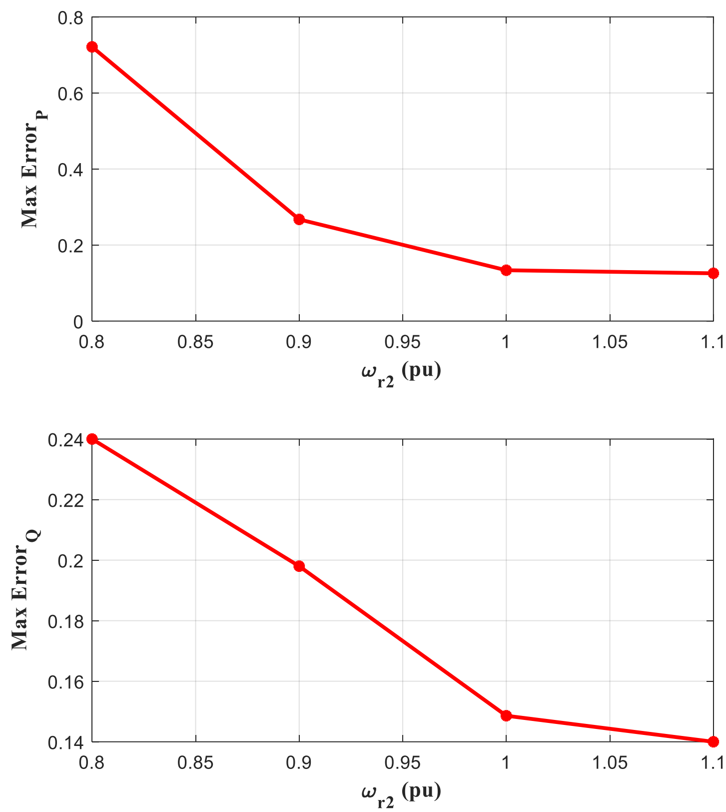

Figure 4-29 Maximum Error Comparison Considering Different Rotor Rotating Velocity (ω_r) for DFIG 2 (ω_{r2})

It can be seen from results that in the aggregate model:

- With $\boldsymbol{\omega_{r1}}$ is fixed at 1.1 pu, the error in P as well as in Q is largest when $\boldsymbol{\omega_{r1} - \omega_{r2}}$ is largest, which happens for $\omega_{r2} = 0.8$ pu. Lowering this difference between ω_{r1} and ω_{r2}, decreases the error, as expected, and the minimum error occurs when $\omega_{r1} = \omega_{r2} = 1.1$ pu, where AE_P is zero and AE_Q is under 1%. Similarly, the RMS error in both P and Q falls to less than 2%. Similar behaviour is observed for the maximum error as shown in Figure 4-29, although the magnitude is somewhat larger at around 14%. This is because the maximum error looks for the largest difference which may occur exactly at one point, whereas the average and RMS errors look at the whole waveform.

4.8 Chapter Summary

In this chapter, a new aggregation method for multiple DFIGs is proposed. The aggregation is achieved by recursively combining two structurally complete DFIG state space representations at a time and equivalencing this to the state space representation of a single DFIG ensuring that both have identical steady state responses. The parameters and incident wind speeds can be different for each DFIG in the aggregate. The features of the aggregated model are:

(1) It preserves the same block structure, i.e., the same outputs (injecting currents) and inputs (prime mover torque) and exactly matches the combined steady state outputs, while still giving a sufficiently accurate transient response.

(2) The aggregated model can be implemented as a single DFIG in any EMT simulation software. It is interfaced to the external system using a modified transformer representation that reflects the current scaling to multiple machines. It does not require modification of existing models in the software, merely an appropriate selection of the parameters.

(3) The aggregated model retains the same major collective oscillation modes of the original cluster of DFIGs with the external network. However, the representation of inter-machine transients within the windfarm is sacrificed due to the aggregation.

(4) The simplification of the detailed model is important for off-line as well as real-time simulation. For off-line simulation, it provides a significant speedup.

(5) For real-time simulation, it could also result in savings in hardware, because more DFIGs in the model would require harnessing more computing cores. Note that windfarm representation with 3 or 4 separate DFIGs are practical when simulating windfarms on real-time simulators [86]. The proposed approach is able to distill a multi-DFIG windfarm into an accurate representation with 3 DFIGs. This should make the proposed approach viable for real-time simulators.

(6) It should be noted that the model is not intended for designing the wind turbine or generator. Rather it is an aggregated representation that permits the study of how the windfarm interacts with the external network, which is modelled on an EMT program. Example applications could involve performance under network faults, power supply into the network as affected by wake conditions and wind speed changes as was shown in this chapter. It could also be used for studying interplant oscillations when multi-machine cluster representation is used.

In Chapter 5, the grid synchronization of a DFIG, which can be considered as an aggregated model of DFIG representing several turbines within a wind farm, is investigated for achieving robustness of stability in DFIGs connected to weak ac networks.

Chapter 5

Understanding the Loss of Synchronization Mechanism

5.1 Introduction

Loss of synchronization, also known as a loss of rotor synchronization, can occur between a wind farm and ac network. During a severe grid fault, the rotor speed deviates significantly from the synchronous speed of the power grid that would cause loss of synchronization and wind farm tripping.

In Chapter 4, an aggregation method is proposed which can be used to represent several DFIGs within a wind farm with only one aggregated model. In this section, a theoretical model of the grid synchronization of the DFIG is developed in the dq frame, which takes into account the system strength (i.e., reciprocal of ac network impedance) and phase locked loop (PLL) tracking. Of course, a small signal (SS) model could be developed to analyze the behaviour, but this is only true for small variations around an operating point. However, loss of synchronism is inherently a large signal behaviour, as it occurs following long duration faults. Hence, this is an attempt to discuss the mechanism using techniques similar to analyzing large signal instability in synchronous machines, using a procedure similar in concept to the equal area criterion. Using the theoretical model in a simple example, the mechanism of synchronization loss is identified, and stability characteristics analyzed. Subsequently, a detailed more realistic model of the DFIG is simulated on an EMT simulator (PSCAD) to show the impacts of PLL parameters and DFIG rotor speed on the grid synchronizing stability of DFIG for a short circuit fault applied to the point of common coupling (PCC).

According to reference [57] the rotor side voltage sourced converter (VSC) results in the DFIG being adversely affected by grid side undervoltage and short circuit faults. A phase-locked loop (PLL) is used for synchronizing with the grid voltage from which the firing signals for the VSC's switches are generated [58], and when the VSC is connected to a weak ac network (i.e., one with a low Short Circuit Ratio - SCR), the PCC voltage can change rapidly with disturbances, making the operation challenging [59], [60]. It has been found that the PLL plays a critical role in the stability of type 3 (DFIG) and type 4 wind turbines (permanent magnet synchronous generator -PMSG type), connected to a weak grid [61], [62]. The PLL parameters and structure have been shown to greatly influence the wind turbine's electromechanical response [63], and an improper choice can lead to excessive oscillations in the DFIG's terminal voltage and output power, which could precipitate a loss of synchronization and deteriorate the security of the bulk power system [64], [65]. With the rapid growth of wind energy penetration, it is getting more and more important to study the mechanism of loss of synchronizing of DFIG, and to find out the critical requirement of system strength to assure the stability of the power system.

With low SCR ac systems, loss of synchronization of the DFIG can be triggered during the fault ride through [66]-[68] interval, which is the period during which the DFIG remains connected from the grid during the fault, permitting it to resume normal operation on fault clearance. In [69], modal analysis is conducted using a small signal model of grid-connected DFIG based wind farm is used to investigate the impacts of power grid strength and PLL parameters on the system stability for a linearized system at its equilibrium point. However, small signal analysis has limited value because the system moves away from the operating point during the fault ride through. It also identifies instability by detecting positive plane eigenvalues but does not offer a physical explanation for the mechanism of stability loss. Therefore, in this research, rather than using the model at a specific operating point, it is assumed that the model is also applicable in a quasi-steady state manner when the DFIG undergoes terminal voltage changes during a fault.

Reference [70] discusses a frequency-adaptive synchronization method for grid-connected power converters that allows capturing sequence components at fundamental frequency and also other frequencies to improve the WTG's grid synchronizing performance during faults. However, the previous work has not investigated the impacts of PLL parameters and machine operating points on loss of synchronism and also the mechanism of the loss.

To fill this gap, in this chapter, a small-signal model is first developed in dq coordinates depicting the grid synchronization of DFIG consisting of grid impedance, PLL and induction generator model. Rather than using the model at a specific operating point, it is assumed that the model is also applicable in a quasi-steady state manner when the DFIG undergoes terminal voltage changes during a fault. Using this assumption, loci of system's eigenvalues are plotted as a function of terminal voltage to analyze the stability characteristics. Although the model cannot be entirely accurate, it does provide a means to understand the mechanism of DFIG's loss of grid synchronization in a qualitative manner. A semi-quantitative indicator index to evaluate degree of stability is introduced to investigate the influence of SCR and induction generator rotor speed. Based on the above, two measures to increase the degree of stability for DFIG are proposed. A detailed DFIG wind turbine is modelled in PSCAD, and simulations are conducted to validate the proposed measures.

5.2 DFIG Phase Synchronization Model

Aside from the turbine mechanical system, a DFIG wind energy conversion system consists of an induction generator, a back-to-back VSC arrangement of a grid side converter (GSC) and rotor side converter (RSC), and a step-up three-winding transformer (as shown in Figure 5-1). The RSC is tasked to produce the rotor terminal voltage in order to control the stator terminal voltage and active power of DFIG. A phase locked loop (PLL) is used to extract the phase of stator terminal voltage for synchronizing and control. The model of phase synchronizing schematic model of DFIG is developed in this section. The loss of synchronizing of DFIG is due to the failure of PLL to lock onto and track the induction generator's stator terminal voltage.

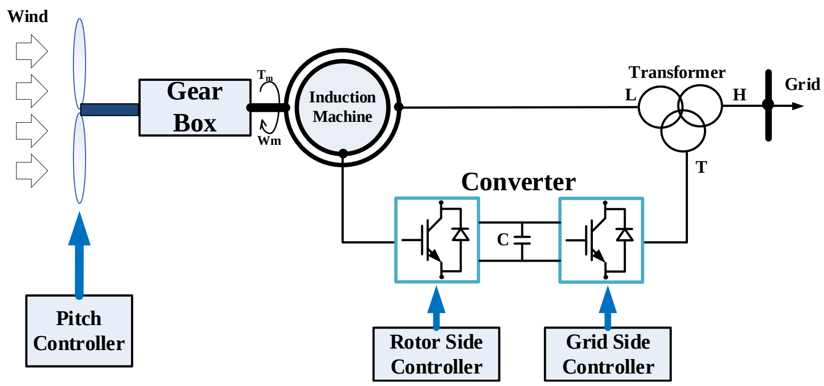

Figure 5-1 Schematic Structure of DFIG [51]

5.2.1 Induction Generator Impedance Model of DFIG

The voltage generated by RSC is directly applied to the rotor terminal of the induction generator. Firstly, the voltage source-impedance model of induction generator based on the widely used dq0 coordinates is used to derive the stator and rotor equations. The dq-axis circuits of induction generator are shown in Figure 5-2 [71].

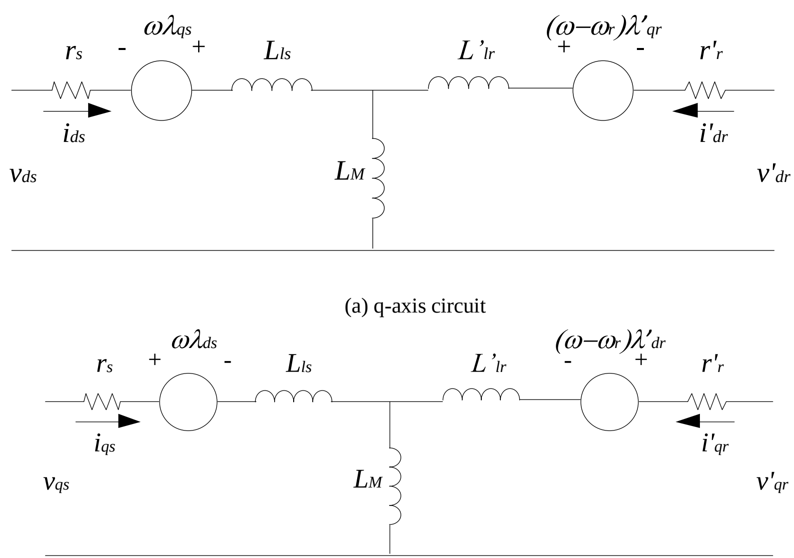

(a) q-axis circuit

(b) d-axis circuit

Figure 5-2 Dq-axis Circuits of Induction Generator

The stator voltage equations of induction generator in dq coordinates can be expressed as follows.

$$\begin{cases} V_{ds} = r_s i_{ds} - \omega_s \lambda_{qs} + \dot{\lambda_{ds}} \\ V_{qs} = r_s i_{qs} + \omega_s \lambda_{ds} + \dot{\lambda_{qs}} \end{cases} \tag{52}$$

And the rotor voltage equations are as follows.

$$\begin{cases} V'_{dr} = r'_r i_{dr} - (\omega_s - \lambda'_{qr} + \dot{\lambda_{dr}} \\ V'_{qr} = r'_r i_{qr} + (\omega_s - \lambda'_{dr} + \dot{\lambda_{qr}} \end{cases} \tag{53}$$

The flux linkages are expressed as below.

$$\begin{cases} \lambda_{ds} = L_{ls} i_{ds} + L_m (i_{ds} + i'_{dr}) \\ \lambda_{qs} = L_{ls} i_{qs} + L_m \left(i_{qs} + i'_{qr}\right) \\ \lambda'_{dr} = L'_{lr} i'_{dr} + L_m (i_{ds} + i'_{dr}) \\ \lambda'_{qr} = L'_{lr} i'_{qr} + L_m \left(i_{qs} + i'_{qr}\right) \end{cases} \tag{54}$$

where, ω is the nominal angular speed, and ω_r is the rotor angular speed. Variables with apostrophe e.g., i'_{dr}, indicate rotor side variables transferred to the stator side.

5.2.1.1. Development of a (quasi-steady state) Small Signal Model

A small signal model is now developed from the above differential equations of the DFIG. The reason it is called a “quasi-steady-state” model is due to the way in which it is used. It is assumed that when the fault occurs, the terminal voltage is depressed, and a locus can be derived to see how the eigenvalues move with the changing voltage magnitude. Although this is not mathematically strict, as will be shown, it can provide an understanding of the loss of synchronization mechanism.

Substituting the corresponding flux linkages from (54), into (52) and (53), gives (55) and (56) yielding the rotor and stator terminal voltage vectors v_r', v_s in the Laplace (s) domain.

$$v_r'(s) = v_{dr}'(s) + jv_{qr}'(s)$$
$$= \left[r_r{}' + \left(s + j(\omega - \omega_r)\right)\left(L_{lr}' + L_M\right)\right]i_r'(s) + L_M(s + j(\omega - \omega_r))i_s'(s) \tag{55}$$

$$v_s(s) = r_s i_s(s) + (s + j\omega)[(L_{ls} + L_M)i_s(s) + L_M i_r(s)] \tag{56}$$

Eliminating rotor current $i_r(s)$ in (56) using (55) gives (57).

$$v_s(s) = \left\{r_s + (s + j\omega)\left[L_{ss} - \frac{L_M^2\left(s + j(\omega - \omega_r)\right)}{r_r' + (s + j(\omega - \omega_r)L_{rr})}\right]\right\} i_s(s) + \frac{(s + j\omega)L_M}{r_r' + (s + j(\omega - \omega_r)L_{rr})} v_r'(s) \tag{57}$$

where $L_{rr} = L_{lr}' + L_M$ and $L_{ss} = L_{ls} + L_M$.

For three-phase systems, abc voltages and currents can be expressed as space vectors. Since the space vector v is rotating with the nominal angular speed ω, the relationship between v and a static dq vector of machine's voltages (v_{dq}) is as follows [71].

$$v = v_{dq} e^{j\omega t} \tag{58}$$

where $v_{dq} = v_d + jv_q, v = v_a + e^{j\frac{2\pi}{3}}v_b + e^{j\frac{4\pi}{3}}v_c$. Transforming this relationship from (58) into Laplace domain leads to

$$v(s) = v_{dq}(s - j\omega) \tag{59}$$

Hence, substituting s by $(s - j\omega)$ in (57) to transform the voltage equation of induction generator into space vector in Laplace domain gives (60).

$$v_s(s) = \left[r_s + s\left(L_{ss} - \frac{L_M^2(s - j\omega_r)}{r_r^{'} + (s - j\omega_r)L_{rr}} \right) \right] i_s(s) + \frac{sL_M}{r_r^{'} + (s - j\omega_r)L_{rr}} v_r^{'} \qquad (60)$$

To convert to a per-unit representation with base frequency $\omega_b = 2 \times \pi \times f_s$, s is replaced by s/ω_b in (60). Note that (60) has the form of a Thevenin impedance Z_m and Thevenin Source E, which represents the internal voltage of the RSC. The values of E and internal impedance Z_m are as in (61).

$$\begin{cases} Z_m = r_s + s\left(L_{ss} - \dfrac{L_M^2(s - j\omega_r)}{r_r^{'} + (s - j\omega_r)L_{rr}} \right) \\ E = (\dfrac{sL_M}{r_r^{'} + (s - j\omega_r)L_{rr}}) v_r^{'}\ (s) = a \times v_r^{'}\ (s) \end{cases} \qquad (61)$$

5.2.2 Theoretical Model for Synchronization of DFIG

The purpose of the RSC side PLL is to provide an angle reference for the RSC's control system to generate firing pulses to produce the rotor terminal voltage. Based on the voltage source-impedance model of induction generator mentioned above, the schematic configuration of phase locking model of a simplified DFIG integrated to a power system can be constructed as in Figure 5-3. The Thevenin impedance Z_s of the ac network comprises the step-up transformer impedance (Z_T) and the network impedance (Z_{net}).

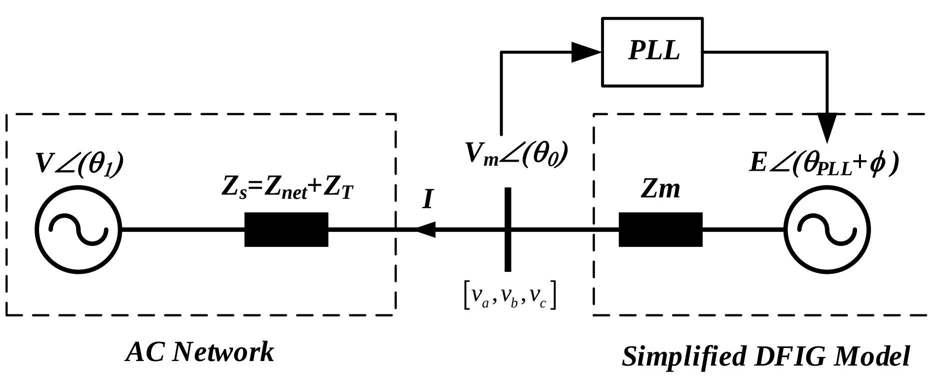

Figure 5-3 Schematic Model of Phase Locking of a simplified DFIG

Numerous PLL topologies have been developed recently for three-phase grid-connected power converters. These include the decoupled double synchronous reference frame PLL (DDSRF-PLL), multiple reference frame-based PLL (MRF-PLL), and dual second-order generalized integrator-based PLL (DSOGI-PLL). Among these, the synchronous reference frame PLL (SRF-PLL) stands out as the most popular choice due to its advantageous features, such as ease of implementation and robust performance [80], particularly in three phase systems. Hence, this thesis uses the widely used synchronous reference frame PLL, as in Figure 5-4 [72], [79], [80] and uses this model in the EMT software for simulation purposes.

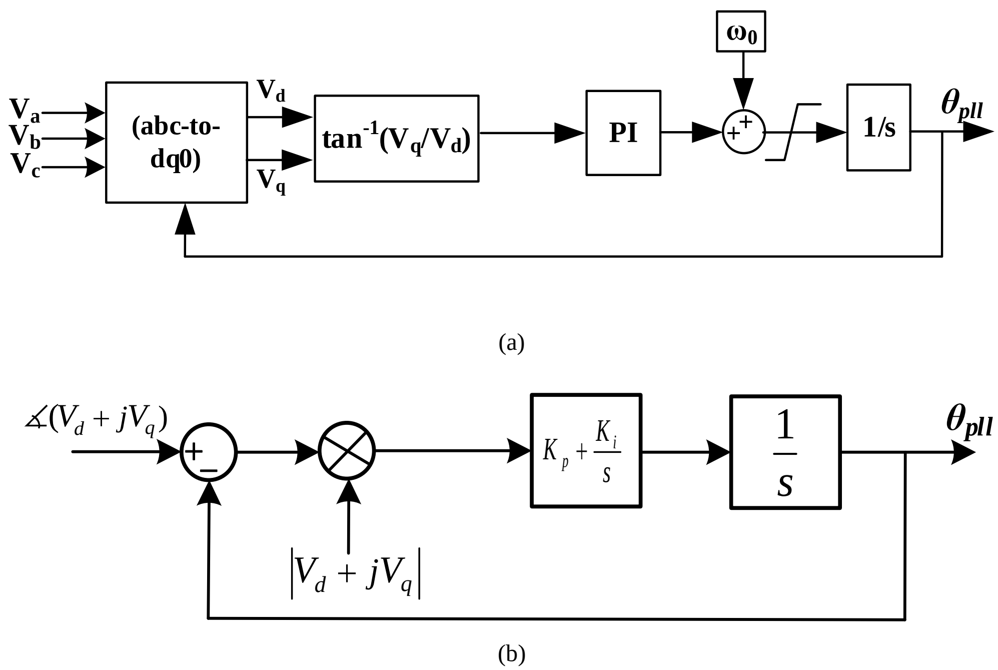

Figure 5-4 PLL Schematic: (a) Model in Stationary (a,b,c) Coordinates, (b) Model in Phasor Representation

The instantaneous phase voltages $[v_a, v_b, v_c]$ in Figure 5-3 are extracted from the stator terminal for phase locking. Let V_m be the phasor of phase ”a” voltage at the point of common coupling, and V is the ac network's Thevenin voltage and E the internal voltage of the simplified DFIG model. Then, we can write (62) as follows.

$$V_m = V + Z_s \frac{E - V}{Z_s + Z_m} = \frac{Z_m}{Z_s + Z_m} V + \frac{Z_s}{Z_s + Z_m} E \tag{62}$$

The PLL tracks the phase angle of V_m. For small signal, the angle can directly be represented by V_q. Using this as reference, the RSC controller issues firing pulses at the appropriate angles to generate the internal voltage E at an angle $(\theta_{pll} + \phi)$ where θ_{pll} is the angle output of the PLL and ϕ is the offset angle generated by the RSC control system to achieve the desired output power. The control system generating offset angle ϕ is represented in Figure 5-5, where P_g, Q_g, and V_g are wind turbine active power, reactive power, and voltage at the point of interconnection to grid, respectively.

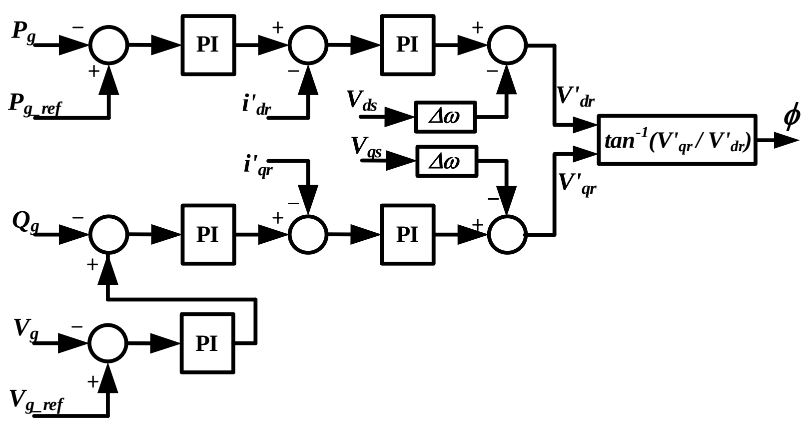

Figure 5-5 Schematic Control System to Generate Offset Angle ϕ

Hence, in polar form, i.e., writing $E = |E|e^{j(\theta_{pll}+\phi)}$ and $V = |V|e^{j(\theta_1)}$, the voltage V_m is as in (63).

$$V_m = \frac{Z_s}{Z_s+Z_m}E + \frac{Z_m}{Z_s+Z_m}V = \frac{Z_s}{Z_s+Z_m}|E|e^{j(\theta_{pll}+\phi)} + \frac{Z_m}{Z_s+Z_m}|V|e^{j(\theta_1)} \qquad (63)$$

The abc-to-dq block in the PLL transforms the voltage V_m to dq variables as in (64).

$$V_{m_{dq}} = \left|\frac{Z_s}{Z_s+Z_m}\right| |E| e^{j(\theta_{pll}+\phi+p_1-\theta_{pll})} + \left|\frac{Z_m}{Z_s+Z_m}\right| |V| e^{j(\theta_1+p_2-\theta_{pll})} \qquad (64)$$

where,

$p_1 = \angle\left(\frac{Z_s}{Z_s+Z_m}\right), p_2 = \angle\left(\frac{Z_m}{Z_s+Z_m}\right)$

From (64), V_{m_q} and V_{m_d} are given out as in (65) and (66). To reach steady state, PLL changes θ_{pll} to make V_{m_q} zero which is discussed in section 5.3.

$$V_{m_q} = \left|\frac{Z_s}{Z_s+Z_m}\right| |E| \sin(\phi + p_1) + \left|\frac{Z_m}{Z_s+Z_m}\right| |V| \sin(\theta_1 + p_2 - \theta_{pll}) \qquad (65)$$

$$V_{m_d} = \left|\frac{Z_s}{Z_s+Z_m}\right| |E| \cos(\phi + p_1) + \left|\frac{Z_m}{Z_s+Z_m}\right| |V| \cos(\theta_1 + p_2 - \theta_{pll}) \qquad (66)$$

In order to find small signal expression for PLL in Figure 5-3, the input of PLL is considered to be $tan(\theta_0 - \theta_{pll})$ to be the same as PLL model available in PSCAD simulation software for comparison. Moreover, θ_1 is considered to be zero for the sake of simplicity. Therefore, (67) is the small signal expression of PLL used in schematic model of a DFIG and AC network in Figure 5-3.

$$
\begin{aligned}
\Delta(\theta_0-\theta_{pll}) \approx \Delta tan(\theta_0-\theta_{pll}) \\
&= \left(\frac{a\times cos(\phi+p_1)}{a\times cos(\phi+p_1)+\mathrm{b}\times\cos\,(p_2-\theta_{pll})}\right. \\
&\left.+\frac{a\times sin(\phi+p_1)+\mathrm{b}\times\sin\,(p_2-\theta_{pll})}{\left(a\times cos(\phi+p_1)+\mathrm{b}\times\cos\,(p_2-\theta_{pll})\right)^2}\times a\times sin(\phi+p_1)\right)\Delta\phi \\
&+\left(\frac{m\times a\times cos(\phi+p_1)+n\times b\times cos(p_2-\theta_{pll})}{a\times cos(\phi+p_1)+\mathrm{b}\times\cos\,(p_2-\theta_{pll})}\right. \\
&+\frac{a\times sin(\phi+p_1)+\mathrm{b}\times\sin\,(p_2-\theta_{pll})}{\left(a\times cos(\phi+p_1)+\mathrm{b}\times\cos\,(p_2-\theta_{pll})\right)^2}\times m\times a\times sin(\phi+p_1) \\
&+\frac{a\times sin(\phi+p_1)+\mathrm{b}\times\sin\,(p_2-\theta_{pll})}{\left(a\times cos(\phi+p_1)+\mathrm{b}\times\cos\,(p_2-\theta_{pll})\right)^2}\times n\times b \\
&\left.\times\, sin(p_2-\theta_{pll})\right)\Delta\omega \\
&-\left(\frac{b\times cos(p_2-\theta_{pll})}{a\times cos(\phi+p_1)+\mathrm{b}\times\cos\,(p_2-\theta_{pll})}\right. \\
&\left.+\frac{a\times sin(\phi+p_1)+\mathrm{b}\times\sin\,(p_2-\theta_{pll})}{\left(a.cos(\phi+p_1)+\mathrm{b}.\cos\,(p_2-\theta_{pll})\right)^2}\times b\times sin(p_2-\theta_{pll})\right)\Delta\theta_{pll}
\end{aligned}
\tag{67}
$$

where,

$$m=\frac{1}{1+\left(\frac{\omega L_s}{R_s}\right)^2}\left(\frac{L_s}{R_s}\right)-\frac{1}{1+\left(\frac{\omega(L_s+L_m)}{R_s+R_m}\right)^2}\left(\frac{L_s+L_m}{R_s+R_m}\right),$$

$$n=\frac{1}{1+\left(\frac{\omega L_m}{R_m}\right)^2}\left(\frac{L_m}{R_m}\right)-\frac{1}{1+\left(\frac{\omega(L_s+L_m)}{R_s+R_m}\right)^2}\left(\frac{L_s+L_m}{R_s+R_m}\right),$$

$$a=\left|\frac{Z_s}{Z_s+Z_m}\right||E|,\quad b=\left|\frac{Z_m}{Z_s+Z_m}\right||V|$$

Also, R_s and L_s are the resistance and inductance of grid side impedance Z_s, while R_m and L_m are the resistance and inductance of induction generator internal impedance Z_m.

Equation (67) is in the form of (68):

$$\Delta\left(\theta_0 - \theta_{pll}\right) \approx \Delta tan\left(\theta_0 - \theta_{pll}\right) = K_1 \times \Delta\phi + K_2 \times \Delta\omega - K_3 \times \Delta\theta_{pll}$$

where

$$K_1 = \left(\frac{a\times cos(\phi+p_1)}{a\times cos(\phi+p_1)+\mathrm{b}\times\cos\,(p_2-\theta_{pll})} + \frac{a\times sin(\phi+p_1)+\mathrm{b}\times\sin\,(p_2-\theta_{pll})}{\left(a\times cos(\phi+p_1)+\mathrm{b}\times\cos\,(p_2-\theta_{pll})\right)^2} \times a \times sin(\phi+p_1)\right),$$

$$K_2 = \left(\frac{m\times a\times cos(\phi+p_1)+n\times b\times\cos\,(p_2-\theta_{pll})}{a\times cos(\phi+p_1)+\mathrm{b}\times\cos\,(p_2-\theta_{pll})} + \frac{a\times sin(\phi+p_1)+\mathrm{b}\times\sin\,(p_2-\theta_{pll})}{\left(a\times cos(\phi+p_1)+\mathrm{b}\times\cos\,(p_2-\theta_{pll})\right)^2} \times m \times a \times sin(\phi+p_1) + \frac{a\times sin(\phi+p_1)+\mathrm{b}\times\sin\,(p_2-\theta_{pll})}{\left(a\times cos(\phi+p_1)+\mathrm{b}\times\cos\,(p_2-\theta_{pll})\right)^2} \times n \times b \times sin\left(p_2-\theta_{pll}\right)\right), \quad (68)$$

$$K_3 = \left(\frac{b\times cos\left(p_2-\theta_{pll}\right)}{a\times cos(\phi+p_1)+\mathrm{b}\times\cos\,(p_2-\theta_{pll})} + \frac{a\times sin(\phi+p_1)+\mathrm{b}\times\sin\,(p_2-\theta_{pll})}{\left(a.cos(\phi+p_1)+\mathrm{b}.\cos\,(p_2-\theta_{pll})\right)^2} \times b \times sin\left(p_2-\theta_{pll}\right)\right)$$

This gives an equivalent control representation as shown in Figure 5-6.

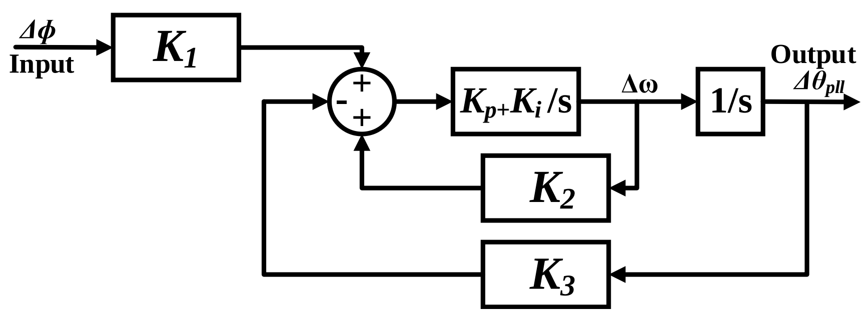

Figure 5-6 Small Signal Model of Schematic Controlled Voltage Source with PLL Represented in Figure 5-3

A step change in the DFIG's angle ϕ (see Figure 5-3) was applied to the EMT model (simulated using PSCAD) and the response θ_{pll} was observed as seen in Figure 5-7. This was compared with the small signal model differential equations and the two results overlap almost perfectly and confirm the validity of the small signal model.

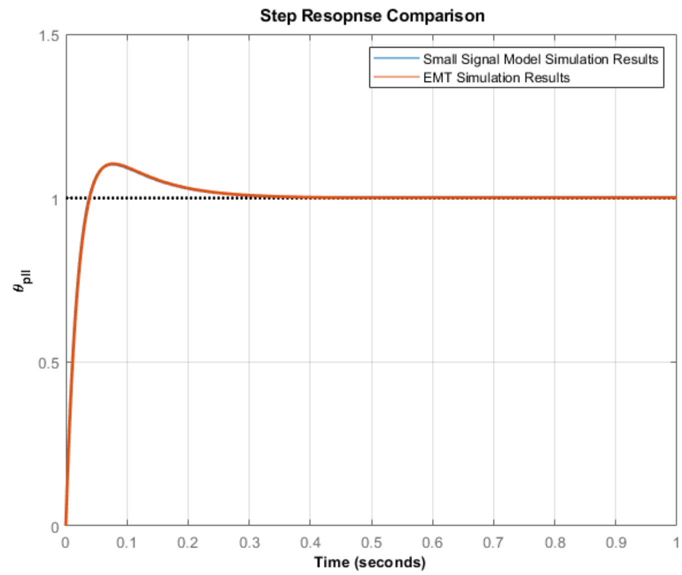

Figure 5-7 Step Response Comparison Between EMT Simulation and Small Signal Model Results (It should be noted that PLL gains, $K_i = 2000, K_p = 200,$ *and SCR for the AC Network is equal to* 4)

The gains of paths in Figure 5-6 are dependent on the circuit parameters and operating point. The model suggests that besides the negative feedback for the angle $\Delta\theta_{pll}$, there is also a positive feedback path for angular frequency $\Delta\omega$ which creates a destabilizing effect on the phase locking system [73]. The stability is related to many factors including the grid side impedance Z_s, grid Thevenin voltage magnitude ($|V|$) and the internal voltage source (E), etc. For a typical fault scenario such as an ac fault, e.g., a voltage reduction in $|V|$, the positive feedback in Figure 5-6 may dominate over the negative feedback, resulting in an increase in the phase $\Delta\theta$ and frequency $\Delta\omega$ in the PLL. Over-frequency of the internal voltage source is the common scenario of the loss of synchronizing for DFIG. The Laplace transfer function (TF) of the linearized PLL model in Figure 5-6 is shown as (69).

$$TF(s) = \frac{K_1K_ps + K_1K_i}{(1 - K_2K_p)s^2 + (K_3K_p - K_2K_i)s + K_3K_i} \tag{69}$$

So far, the theoretical model for analyzing the stability of DFIG synchronization has been developed. The next section investigates the stability features of the proposed model.

5.3 Stable Operation Constraints and PLL Impacts

The arrangement of the DFIG as in Figure 5-3 can experience synchronous instability at certain operating points, as will be shown in this section. Using the model of Figure 5-3, the mechanism of loss of synchronization is explained and an indicator F_s is proposed to investigate the stability margin of synchronizing for a DFIG.

5.3.1 Stable Operation Constraints of Inverter Based VSC

In Figure 5-3, the angle reference for measurement can be set as the initial angle θ_1 for the grid side Thevenin voltage source, so that $\theta_1 = 0$. The angle difference between the two voltage sources ($|V|$ and $|E|$) i.e., ($\theta_{pll} + \phi$) must be smaller than 90 degrees to for a stable power flow to exist. For small angles, V_{m_q} in (65) is essentially proportional to the phase angle difference between the angle θ_0 of the PCC voltage (V_m) and the PLL output angle θ_{pll} . As a result, for the locked PLL in the steady state, V_{m_q} becomes zero. With V_{m_q} = 0, and ac network source angle taken as reference, i.e., $\theta_1 = 0$, (65) gives (70) below:

$$\left|\frac{Z_s}{Z_m}\right|\left|\frac{E}{V}\right|\sin(\phi + p_1) = \sin(\theta_{pll} - p_2) \tag{70}$$

As the right side of (70) is a sine function with magnitude less than unity, for (70) to be satisfied requires the stable operating range of angle ϕ to satisfy (71). So, the maximum angle ϕ (ϕ_{max}) can be calculated from (72).

$$\left|\left|\frac{Z_s}{Z_m}\right|\left|\frac{E}{V}\right| \sin(\phi + p_1)\right| \leq 1 \tag{71}$$

$$\phi_{max} = \sin^{-1}\left(\left|\frac{Z_m}{Z_s}\right|\left|\frac{V}{E}\right|\right) - p_1 \tag{72}$$

Expression (71) is more easily satisfied if $|Z_s|$ is sufficiently small, i.e., the connected grid is strong.

In Figure 5-3, the active power (P) from the DFIG into the ac network is given by (73):

$$P = \frac{E \times V}{X} sin\left(\theta_{pll} + \phi\right) \tag{73}$$

where $X = X_s + X_m$, and considering the steady state condition (i.e., $\theta_{pll} = \theta_0$), the active power generated by the DFIG's voltage source E can be controlled using its angle ϕ since the other parameters are fixed. Hence, ϕ_{max} in (71) sets the angle limit of the internal voltage source E in Figure 5-3. To maintain stability, a smaller ϕ_{max} means a smaller range for the angle ϕ and consequently the amount of power that can be controlled.

Equation (71) shows that a smaller $|V|$ will lead to a smaller ϕ_{max} and bring the system closer to instability. Similarly, (70) also indicates that as the voltage magnitude of the ac system equivalent becomes small, the inequality equation (70) also comes closer to being violated.

In order to validate (70), a schematic system represented in Figure 5-3 is modeled in PSCAD with the parameters in Table 5-1. Resistance and inductance of the equivalent network impedance (Z_s) and magnitude of AC system's Thevenin voltage ($|V|$) are shown in Table 5-1 for a SCR of 4 and X/R ratio of 7. The internal impedance of the induction machine (Z_m) is calculated as in (61) using the induction machine parameters in Table 4-1 to Table 4-5 and rotor angular speed (ω_r) of 1.2 pu. The rated voltage for the DFIG is assumed to be 0.9 kV since the three-winding step-up transformer (33/0.9/0.69 kV) impedance (Z_T) is considered as part of the network impedance (Z_{net}) shown in Figure 5-3.

Table 5-1 Parameters of PSCAD model

	Source	
Component	Voltage/kV	Frequency/Hz
Thevenin Voltage ($\|V\|$)	0.9	60
Controlled Voltage Source (E)	0.9	60
	Impedance	
Component	Resistance (Ω)	Inductance (H)
System Impedance ($Z_s = R_s + jX_s$)	R_s= 0.006	L_s= 1.06e-4
Internal Impedance ($Z_m = R_m + jX_m$)	R_m = 0.0008	L_m = 5.01e-5

The PLL gains were selected by trial as K_p = 200, and K_i = 2000 for EMT simulations. This gave a sufficiently fast response for the PLL. For the example system with data as in Table 5-1, (71) gives the maximum angle (ϕ_{max}) as 28.2 degrees. The PSCAD simulation results for power and ac terminal voltage comparing changes in ϕ at 3 seconds to $\phi = 27^o$ and $\phi = 30^o$, are shown in Figure 5-8. It can be seen that system is stable for $\phi = 27^o$ and unstable for $\phi = 30^o$, validating the $\phi_{max} = 28.2^o$ limit obtained theoretically from (71).

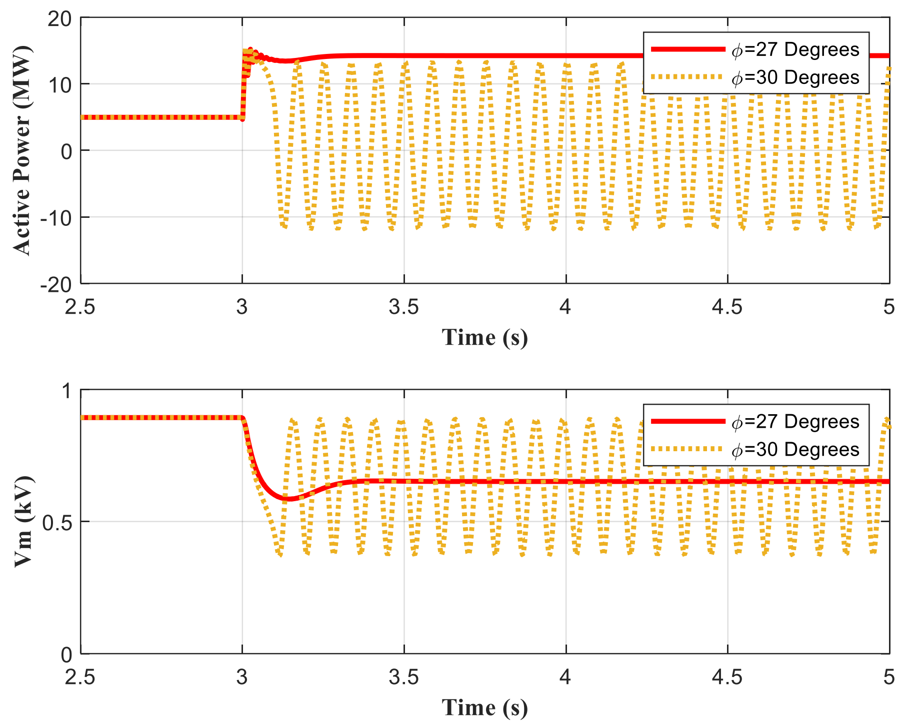

Figure 5-8 EMT Simulation Results of DFIG Active Power Output and Terminal Voltage V_m to Validate the Maximum Initial Angle ϕ

Consider a DFIG connected to a network with parameters given in Table 5-1. At the operating point the DFIG's internal voltage (see Figure 5-3) is 0.9 kV (or 1 pu) and the ac system's Thevenin voltage is also $|V|$ = 0.9 kV. The initial angle ϕ of the internal voltage source is 6.8 degrees which gives the rated 5 MW active power with a rated terminal voltage V_m = 0.9 kV. Using equation (71), the minimum voltage $|V|$ required for stability comes out as $|V|_{min} = \left|\left|\frac{Z_s}{Z_m}\right| |E| \sin(\phi + p_1)\right| =$ 0.19 kV. Figure 5-9 shows plots of active power and terminal voltage V_m for a Thevenin voltage reduction to i) $|V|$ = 0.18 kV and ii) $|V|$= 0.2 pu respectively. Note that for $|V|$ = 0.2 kV, the system remains stable, but instability sets in for $|V|$ = 0.18 kV which confirms the critical voltage limit of 0.19 pu obtained theoretically.

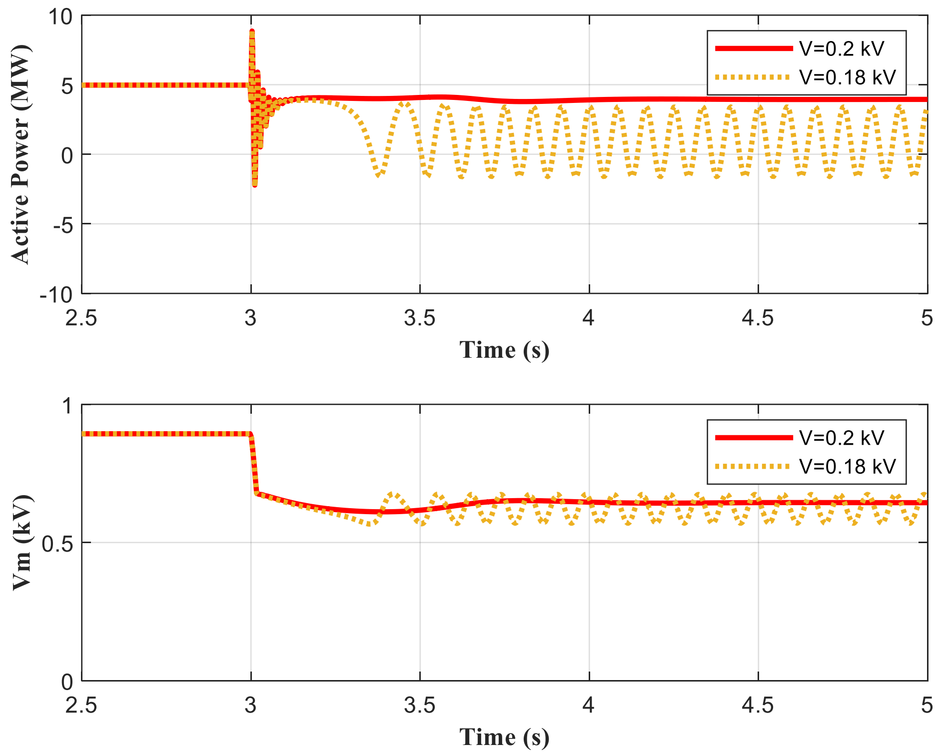

Figure 5-9 EMT Simulation Results of DFIG Active Power Output and Terminal Voltage V_m to Validate the Minimum Thevenin Voltage Magnitude $|V|$

5.3.2 Small Signal Analysis using Root Locus

Using equations (63) to (72), the root locus plot of the dominant roots as a function of grid Thevenin voltage ($|V|$) is plotted in Figure 5-10. The system parameters are as in Table 5-1 and PLL parameters are K_p = 200 and K_i= 2000. There is no instability when the converter operates close to its normal operating voltage of 0.9 kV as the system eigenvalues are all in the left-hand plane for any $|V|$ > 0.44 kV.

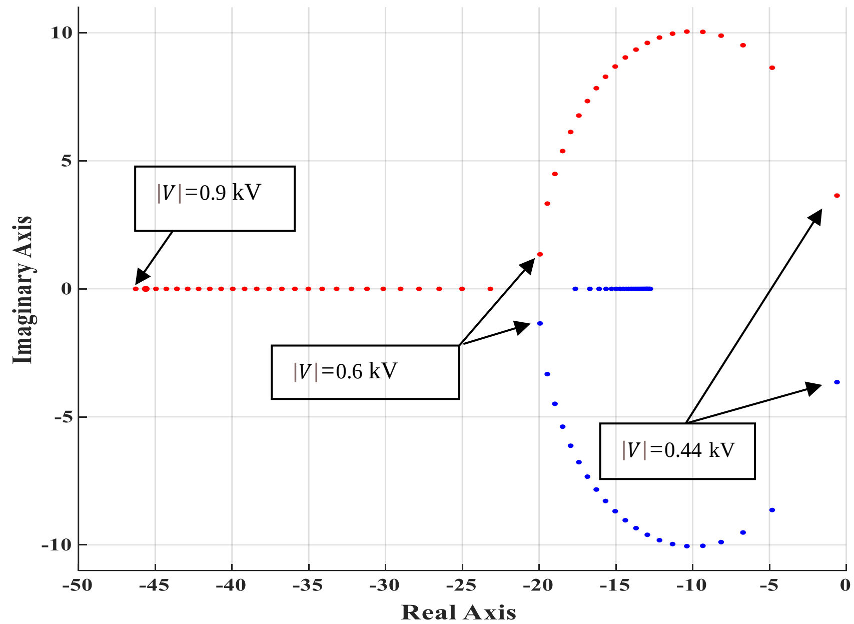

Figure 5-10 Loci of Phase Locking Small Signal Model for Changing Grid Voltage ($|V|$) from 0.9 kV to 0.44 kV

5.3.3 Impacts of PLL Parameters

This subsection is devoted to investigating how PLL gains impact the output response of PLL. Equation (71) only defines the maximum limit on ϕ which is a necessary condition for stability. PLL parameters K_p and K_i also affect the oscillatory response. To show this impact, the step response of PLL considering a schematic system in Figure 5-3 with parameters as in Table 5-1 using (62) to (69) is shown in Figure 5-11. With the system operating at nominal ac voltage of 0.9 kV, a step change is applied to the phase ϕ of the DFIG equivalent, and the output angle θ_{pll} is observed. In Figure 5-11(a), response with different K_i values is shown while K_p is fixed to 200 and grid voltage magnitude is at its rated value of 0.9 kV. The system with smaller value of K_i has larger damping coefficient which results in smaller overshoot compared to the one with larger value of K_i. In addition, in Figure 5-11(b), the PLL response with different K_p values is shown while K_i is fixed to 2000 and grid Thevenin voltage magnitude is normal (i.e., 0.9 kV). The system with larger value of K_p has larger damping coefficient which results in smaller overshoot compared to the one with smaller value of K_p. Finally, Figure 5-12 shows the PLL step response for a fixed PLL gains (K_p = 200 and K_i = 2000) while changing Thevenin voltage magnitude $|V|$.

From the above analysis, parameters should be selected according to system parameters to give fast settling time and not too large an overshoot. For this case study, gains were selected heuristically and K_p = 200 and K_i = 2000 were found to provide overall good response for steady state as well as transient operation.

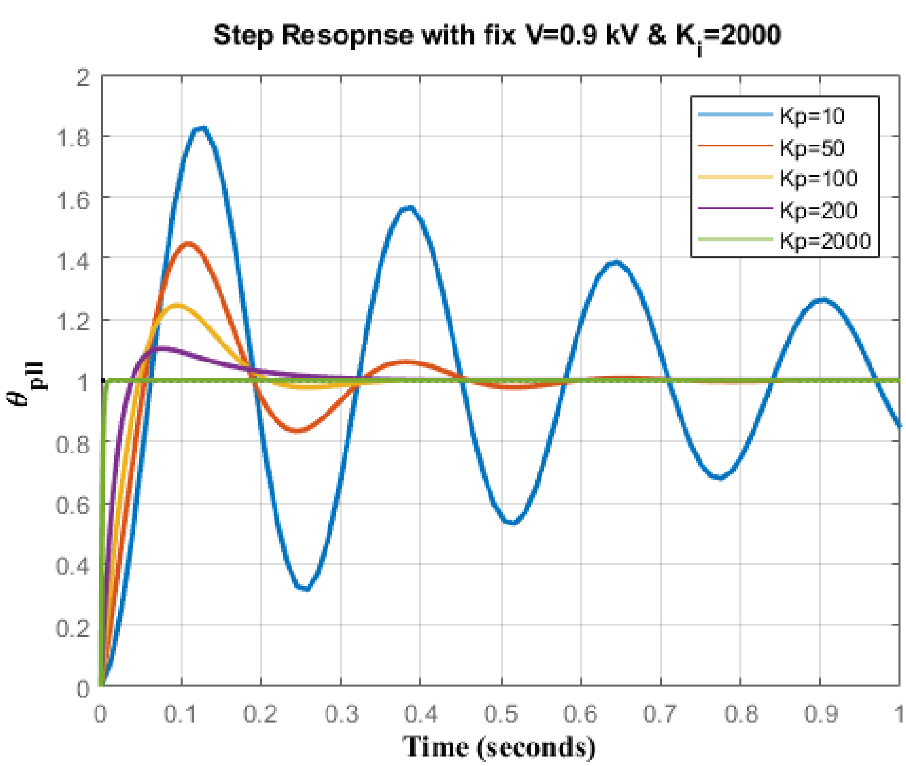

a) Step Response with Fix $|V|$=0.9 kV & K_i = 2000

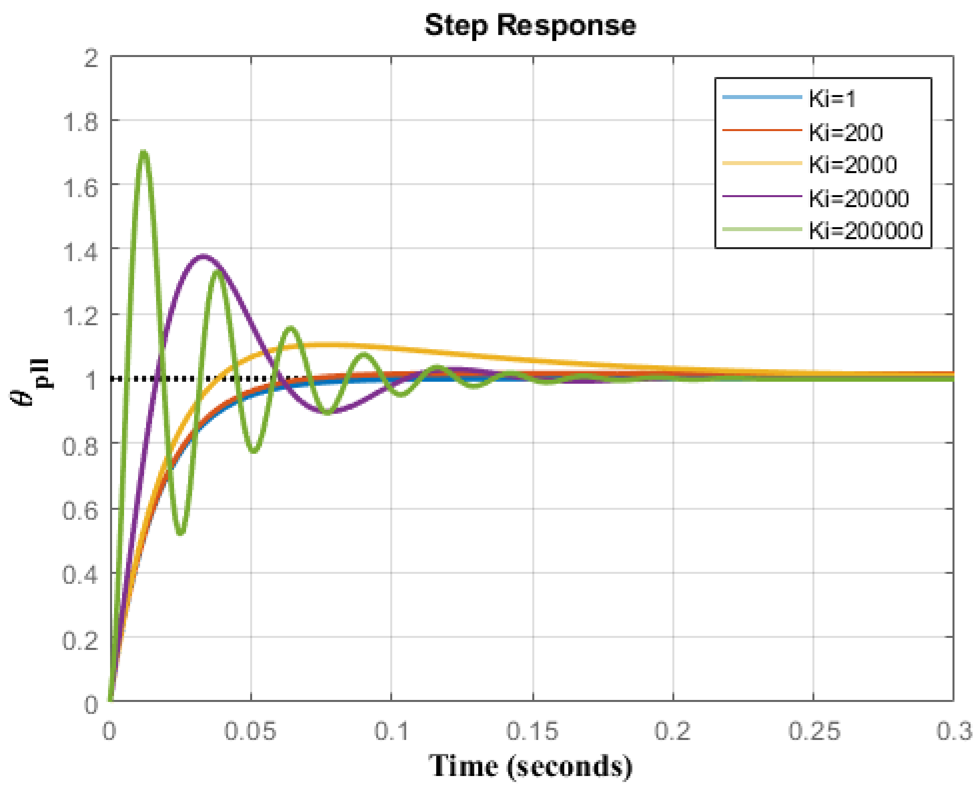

b) Step Response with Fix $|V|$=0.9 kV & $K_p = 200$

Figure 5-11 PLL Step Response Comparison with Different PLL Parameters

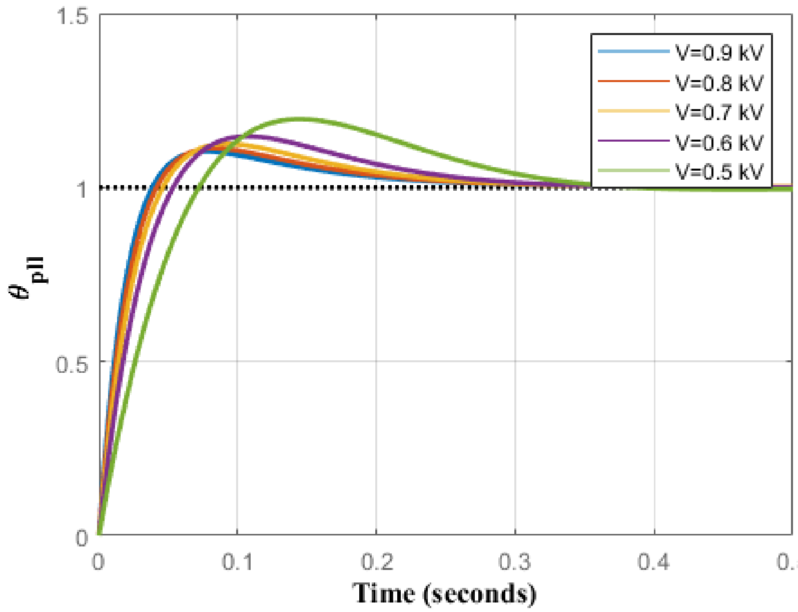

Figure 5-12 PLL Step Response Comparison with Different Thevenin Voltage Magnitude $|V|$ (PLL gains are $K_i = 2000$, $K_p = 200$)

5.4 Stability Analysis of Synchronizing DFIG

The DFIG may operate over a wide range of wind speeds. However, the range of system strengths (SCR) over which it may operate depends on the ability of the PLL's to synchronize (i.e., to achieve a phase lock) to the grid voltage. This section presents investigation on the required system strength when connecting a DFIG considering different operating points of DFIG.

5.4.1 Internal Voltage and Impedance of DFIG

From (61), the DFIG's internal voltage E and impedance Z_m are operating point dependent and according to (71) and (72) can affect the stability of the phase locking. The parameters of a typical DFIG as listed in Chapter 4 are used in this discussion. The magnitude and angle of internal impedance of induction generator (Z_m) and DFIG's internal voltage E as a function of rotor speed (ω_r) at rated power loading at the fundamental frequency (60 Hz) are plotted in Figure 5-13 as a function of rotor speed.

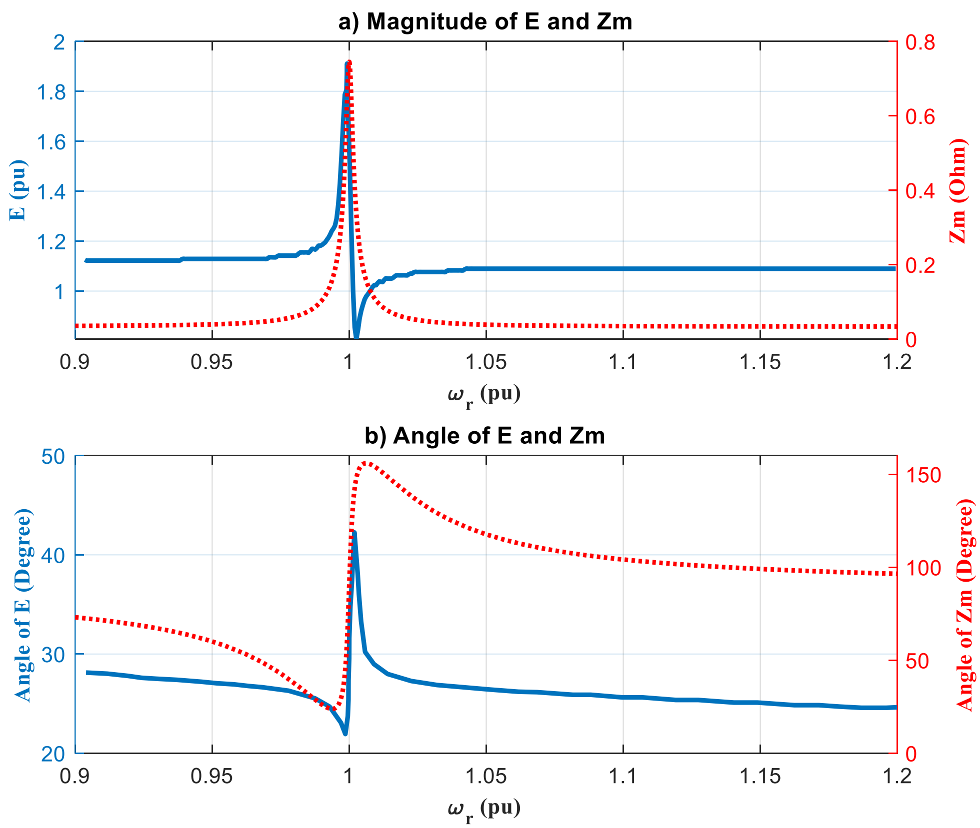

Figure 5-13 Induction Generator Impedance (Z_m) and Internal Voltage $|E|$ at Fundamental Frequency (60 Hz)

The plots show that the impedance is significantly dependent on the rotor speed. The resistance of the generator is negative when rotating at super-synchronous speed, and the magnitude reaches its maximum at synchronous speed [74], [75]. Also, Figure 5-13 illustrates that the magnitude and angle of internal voltage E, changes drastically at a rotor speed of 1.0 pu.

5.4.2 Stability Analysis

As previously discussed in Section 5.3, (70) to (72) indicate that the stability margin will be larger for: a) smaller values of internal voltage offset angle ϕ, b) smaller values of internal voltage magnitude $|E|$, c) larger values of internal impedance magnitude Z_m, and d) larger values of grid side Thevenin voltage magnitude $|V|$. From (65) define a function $VMQ(\theta_{pll} - p_2)$ as given in (74). This equation can be used to characterize the PLL behavior during a voltage dip.

$$VMQ(\theta_{pll} - p_2) = \left[\frac{(Z_s + Z_m)}{|V|Z_m}\right] V_{mq}$$

$$= [\left|\frac{Z_s}{Z_m}\right| \left|\frac{E}{V}\right| sin(\phi + p_1)] \tag{74}$$

$$- sin(\theta_{pll} - p_2) = F_s - sin(\theta_{pll} - p_2)$$

where

$$F_s = \left|\frac{Z_s}{Z_m}\right| \left|\frac{E}{V}\right| \sin(\phi + p_1) \tag{75}$$

Figure 5-14 shows a plot of $VMQ(\theta_{pll} - p_2)$ for the system considered previously in Section 5.3 with the parameters in Table 5-1 for the nominal operating condition (i.e., $|V|$ = 0.9 kV blue curve) and during voltage dip conditions (i.e., red and yellow curves). A fault in the system will result in a voltage dip, which can be considered as drop in the Thevenin voltage ($|V|$) of the system equivalent. Let us say it drops to a smaller value, say $|V|$ = 0.6 kV. As a result, the value of F_s will increase as $|V|$ occurs in the denominator in (72). In Figure 5-14, this change can be shown as an abrupt change in the operating point from point A to B. At point B, the input V_{m_q} of the PLL (which is a measure of phase error) is transiently positive, so the output angle θ_{pll} increases attempting to make the error V_{m_q} =

0; making the operating point move in the direction of point C. As explained in Figure 5-11, the step response of PLL shows an overshoot depending on PLL parameters and grid Thevenin voltage magnitude ($|V|$), before settling down with a damping constant. Due to this, the operating point can overshoot point C toward D, before moving back towards C. The operating point would oscillate around and finally settle at C depending on the damping constant of the oscillation. If it goes beyond point D, the system will lose synchronization with the grid. Figure 5-14 shows F_s for three operating condition, i,e, $|V|$ = 0.9 kV, 0.6 kV and 0.4 kV, respectively. F_{s1}, F_{s2}, and F_{s3} are the y-intercepts for the three VMQ curves, which occur when $\left(\theta_{pll} - p_2\right) = 0$. There is no zero crossing for VMQ when $|V|$ is less than 0.4 kV which means no equilibrium point exists and the PLL cannot lock phase at all. Therefore, the index F_s is proposed in (75) as an indicator of stability for DFIG's phase synchronizing and having lower F_s value for a DFIG means a greater stability margin. Based on the VMQ curve in Figure 5-14, it is not possible to determine with certainty that a particular F_s value will precipitate instability, as the swing of VMQ also depends on the overshoot of $\left(\theta_{pll} - p_2\right)$. However, it can be concluded that F_s serves as a relative index, where a higher value indicates an increased likelihood of instability in the DFIG due to post-fault synchronization failure.

Combining (75) and (61) results in (76) which is showing index F_s expressed as a function of rotor speed (ω_r), and is plotted in Figure 5-15 for an ac network with SCR of 4 and X/R=7.

$$F_s = \left| \frac{Z_s}{r_s + s\left(L_{ss} - \frac{L_M^2 (s - j\omega_r)}{r_r' + (s - j\omega_r) L_{rr}}\right)} \right| \left| \frac{\left(\frac{sL_M}{r_r' + (s - j\omega_r) L_{rr}}\right) v_r'(s)}{V} \right| \sin(\phi + p_1) \qquad (76)$$

The indicator index F_s shows that the stability margin reduces (i.e., F_s increases), and is worst when $\omega_r = 1.11$ pu since index F_s value is largest for this wind speed.

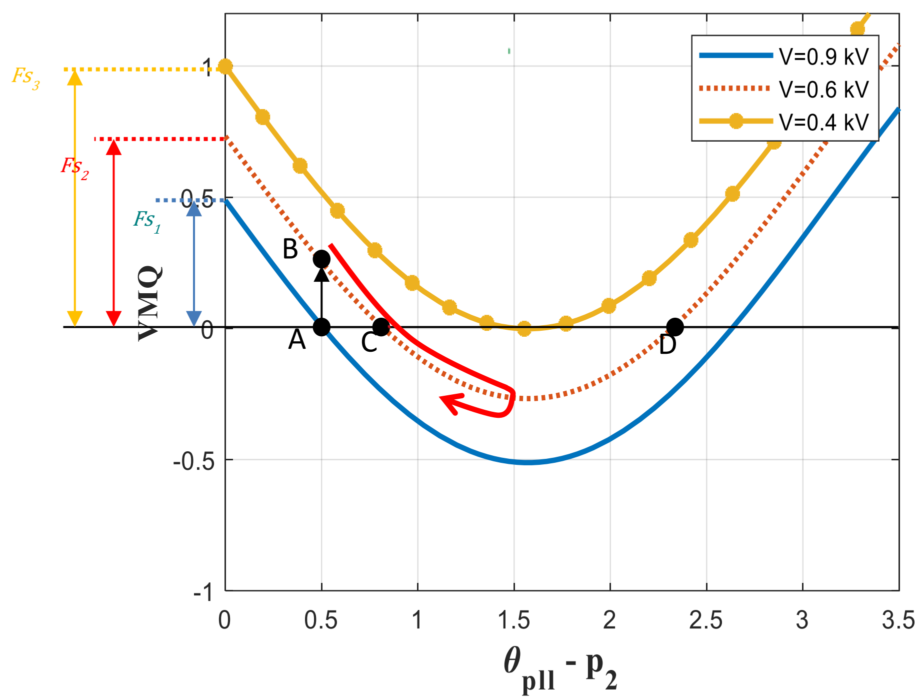

Figure 5-14 VMQ vs ($\theta_{pll} - p_2$) to Represent the Behavior of PLL During a Sudden Voltage Dip of 33 % and 50 %.

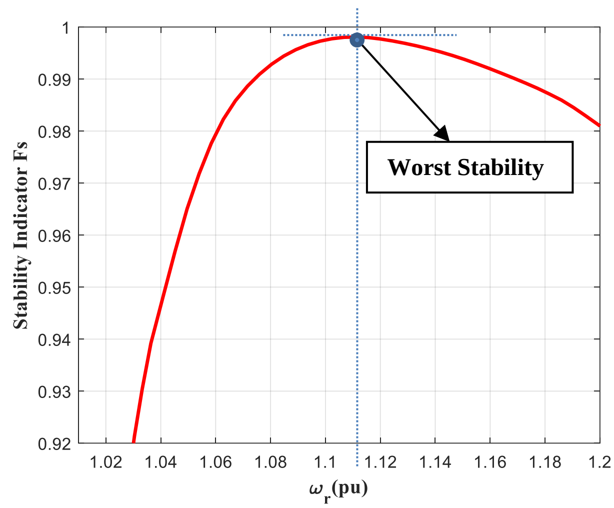

Figure 5-15 Stability Indicator F_s vs Rotor Speed (ω_r) for the Case Study DFIG Connected to an AC System with SCR= 4 and X/R= 7.

5.4.3 Validation using EMT Simulation

The synchronizing stability is validated by EMT simulation using the PSCAD software. As shown in Figure 5-16, a detailed generic DFIG wind turbine generator rated at 5 MW including induction machine, converter, step-up transformer connected to an ac network was modelled. The WTG parameters of the WTG are given in Chapter 4, Table 4-1 to Table 4-4. Two fault scenarios including: (i) A remote three-phase-to-ground fault, (ii) A 6-cycle three-phase-to-ground fault considered to be applied at 3 seconds to investigate impact of network strength, wind turbine rotor speed, and PLL parameters on the synchronization stability of the DFIG system. The network strength is represented in pu as a short circuit ratio, i.e., the ratio of short circuit MVA to the WTG power rating.

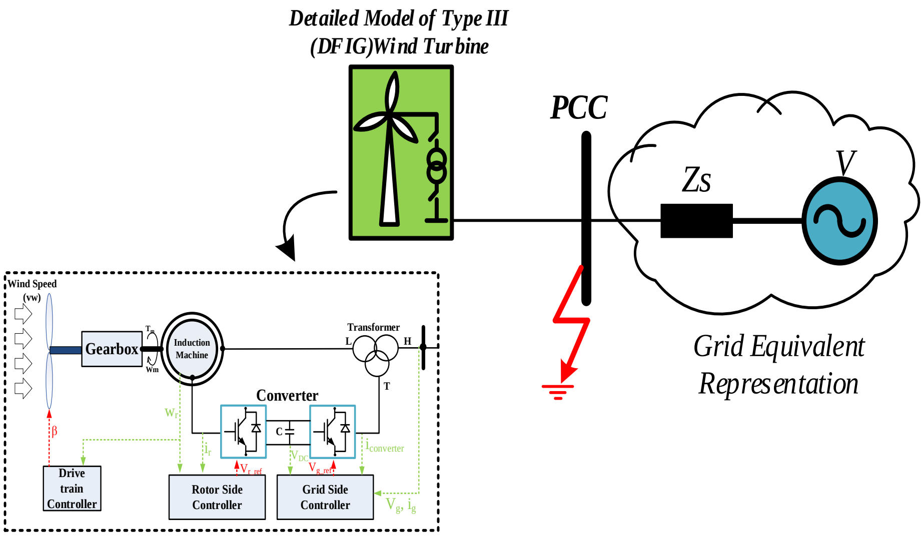

Figure 5-16 Schematic of Detailed DFIG Model and Network Represented in PSCAD

5.4.3.1 Results for Considering a Remote Fault

The analysis approach of Section 5.4.2 can be used to qualitatively examine the mechanism for loss of DFIG synchronizing. The reason that it is qualitative, is that the voltage depression is caused by faults, that not only change the Thevenin voltage but also the Thevenin impedance, so the equations of section 5.2.1 are not exactly accurate. Also, the amount of overshoot in Figure 5-14 is not easy to determine analytically. Nevertheless, the analysis approach does demonstrate the general trend on how system strength (SCR), rotor operating speed ω_r and PLL gains affect the stability of the DFIG.

As was mentioned in Section 5.3.1, expression (19), which is a necessary condition for stable synchronization, is more readily satisfied if $|Z_s|$ is small, i.e., the connected grid is strong. As mentioned earlier in the previous section, the system stability margin is higher when F_s is smaller and from (75), the calculated index F_s for a DFIG connected to an ac network with SCR = 4 is lower compared to a network with SCR = 3, since $|Z_s|$ occurs in the numerator of F_s (introduced in (75)) and other parameters of this index are identical for same DFIGs. To demonstrate this, Figure 5-17 shows the simulated rms voltage at PCC and output active power for the wind turbine in Figure 5-1 when there is a remote fault which drops $|V|$ to 0.6 pu. Two different networks, with SCRs of 3 and 4 respectively with X/R = 7 are considered. As seen Figure 5-20, the network with SCR = 3 experiences instability, whereas that with SCR = 4 does not.

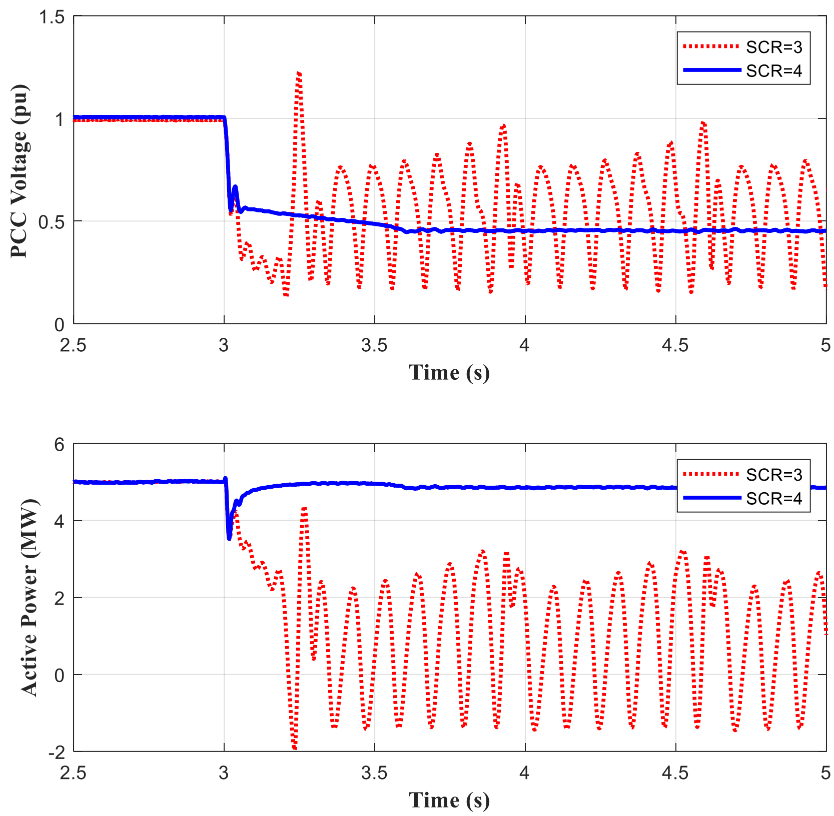

Figure 5-17 Time Domain Responses of PCC Voltage (rms) and Active Power of DFIG at PCC with Different Network Short Circuit Ratio-SCR = 3 and SCR = 4 with $\omega_r = 1.12$ pu When There is a Remote Fault Which Drops $|V|$ to 0.6 pu.

Based on the analysis of PLL parameters in Section 5.3.2, it is evident that the PLL's angle overshoot following a disturbance is smaller with a smaller integral gain value, K_i.

Consequently, a reduced K_i value minimizes the possibility of the operating point in Figure 5-14 surpassing point D, thus lowering the risk of instability. This conclusion is further supported by the data illustrated in Figure 5-18, which demonstrates that reducing K_i from 2000 to 1000 successfully stabilized the system, despite the reduced SCR.

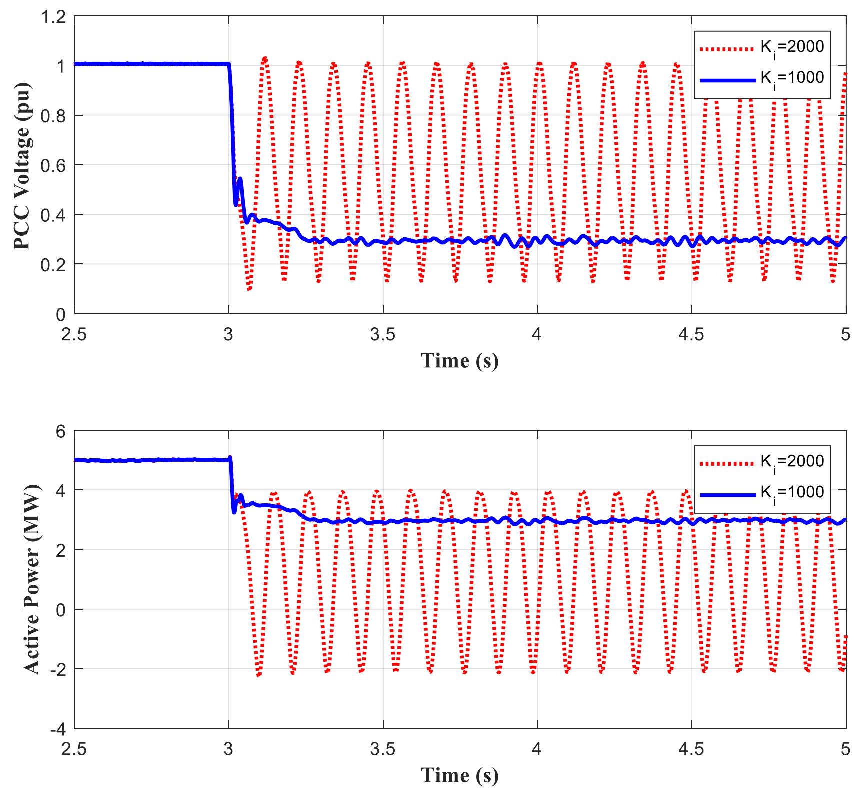

Figure 5-18 Time Domain Responses of PCC Voltage (rms) and Active Power of DFIG at PCC with Different PLL Parameter-$K_i = 2000$ and $K_i = 1000$ (K_p fixed at 200 for both) with $\omega_r = 1.12$ pu and network SCR = 4 When There is a Remote Fault Which Drops $|V|$ to 0.5 pu.

As previously discussed in Section 5.4.2, Figure 5-19 indicates that increasing/decreasing rotor speed of the DFIG from ω_r = 1.12 pu to ω_r = 1.2 pu/ω_r = 1.05 pu in this example can maintain stability of the DFIG connected to a network with SCR of

3. That means the system stability can also be maintained by avoiding the vulnerable rotor speed (i.e., ω_r = 1.11 for this case study) without curtailing the generated wind power.

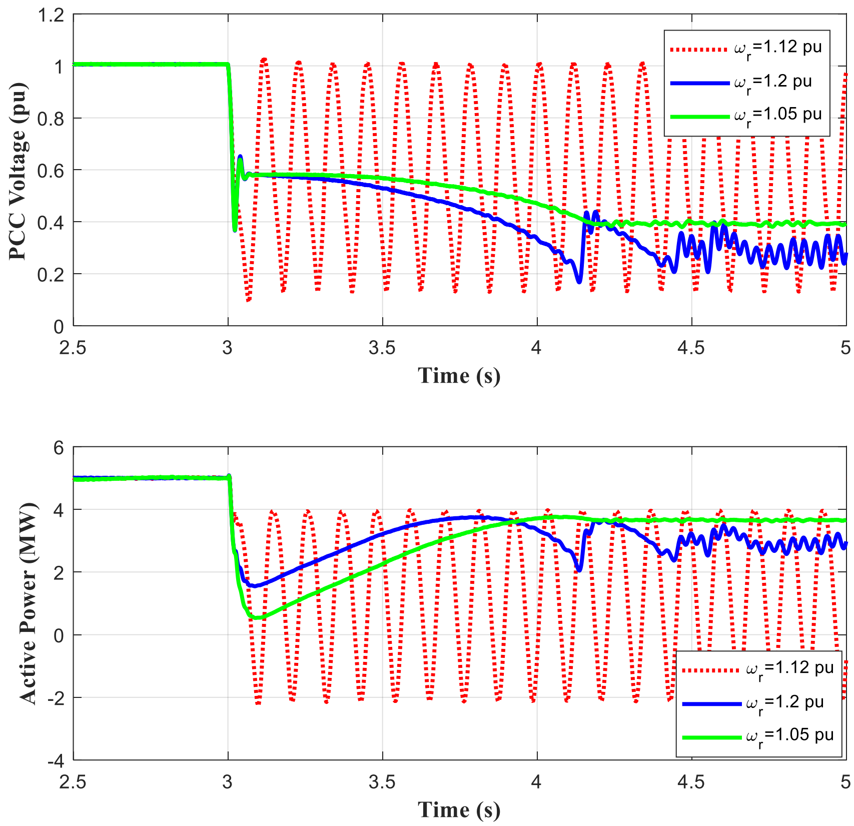

Figure 5-19 Time Domain Responses of PCC Voltage (rms) and Active Power of DFIG at PCC with Different Rotor Speed-ω_r = 1.12, ω_r = 1.2 and ω_r = 1.05 with SCR = 4 When There is a Remote Fault Which Drops $|V|$ to 0.5 pu.

5.4.3.2 Results for a Solid 3-Phase Fault

A 6-cycle three-phase-to-ground fault is applied at 3 seconds to investigate impact of network strength, wind turbine rotor speed, and PLL parameters on the synchronization stability of the DFIG system. Note that unlike the remote fault, a bolted short circuit is much severer, and so the theoretical explanation given previously is not strictly rigorous. The simulation results for same conditions, as previously considered for a remote fault, i.e., different SCRs, reduction of PLL gain (K_i) and increasing/decreasing rotor speed (ω_r) are illustrated in Figure 5-20, Figure 5-21, and Figure 5-22, respectively. Nevertheless, as can be seen DFIG loss of synchronization still follows the general trends as with the remote fault. Figure 5-20 shows loss of synchronization after 3-phase fault for the DFIG connected to weaker network (with SCR=3). In Figure 5-21, it was shown that PLL integral gain reduction from 2000 to 1000 can help DFIG to get back to stability. Finally, Figure 5-22 illustrates that vulnerable rotor speed, i.e., $\omega_r = 1.12\ pu$ in this example, can be avoided to help DFIG ride through the fault without experiencing loss of synchronization.

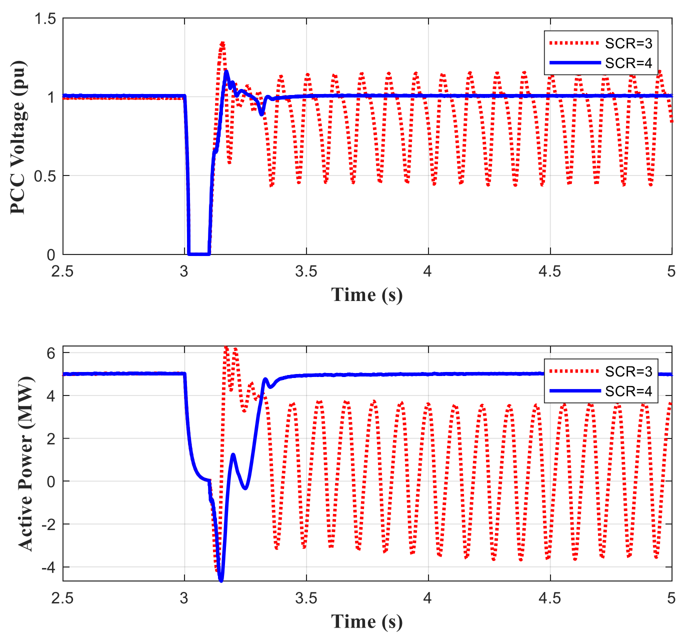

Figure 5-20 Time Domain Responses of PCC Voltage (rms) and Active Power of DFIG at PCC with Different Network Short Circuit Ratio-SCR = 3 and SCR = 4 with $\omega_r = 1.12$ pu for a 3-Phase Solid Fault.

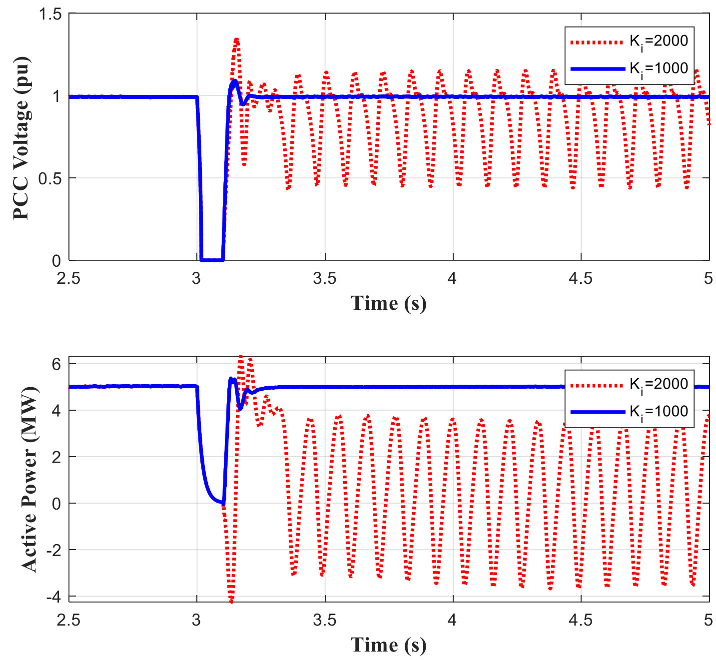

Figure 5-21 Time Domain Responses of PCC Voltage (rms) and Active Power of DFIG at PCC with Different PLL Parameter-$K_i = 2000$ and $K_i = 1000$ (K_p fixed at 200 for both) with $\omega_r = 1.12$ pu and network SCR = 3 for a 3-Phase Solid Fault.

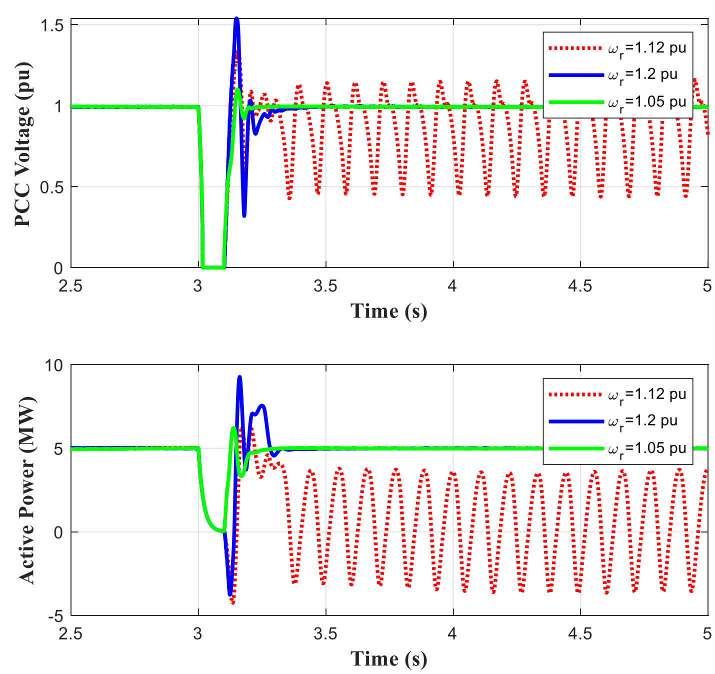

Figure 5-22 Time Domain Responses of PCC Voltage (rms) and Active Power of DFIG at PCC with Different Rotor Speed-ω_r = 1.12, ω_r = 1.2 and ω_r = 1.05 with SCR = 3 for a 3-Phase Solid Fault.

5.5 Chapter Summary

The chapter proposes a mathematical model of a phase-locked loop and DFIG for investigating synchronization to the grid following an ac fault. The model reveals the mechanism of loss of synchronization caused by ac voltage dips resulting from remote faults. Small signal analysis identifies a positive feedback path from the transient angular frequency $\Delta\omega$ in the PLL model, in addition to a negative damping path coming from the phase output. If the positive feedback dominates, synchronizing stability can be lost.

Although the small signal model is not strictly valid for large disturbances such as faults, it can still provide insight into the mechanism of loss of synchronism, if we assume it can be applied in a quasi-steady state manner. This can provide a qualitative understanding of what parameters affect the DFIG stability and is useful for analyzing trends. With this assumption, a large signal plot of the synchronizing signal (proportional to measured q axis voltage V_{m_q}) and a signal dependent on the PLL's output phase angle is put forward to show how large the swing of V_{m_q} can be before it reaches beyond a point of no-return. The zero-crossing points of this curve represent possible operating points in steady state since the error in PLL input is equal to zero and PLL phase is locked to grid frequency. There is no operating point for curves without zero-crossing points. A new stability indicator index F_s is introduced to quantify the tendency of the DFIG to lose synchronism. It is shown that decreasing the rotor side converter PLL integration gain and changing rotor speed can help increase the stability degree.

PSCAD simulation results are presented to show the impacts of PLL parameters and DFIG rotor speed on the grid synchronizing stability of DFIG for a remote fault and three-phase-to-ground fault happened at PCC. Below conclusions were made according to this study:

1. During a voltage dip at the PCC, the output frequency of the PLL may reach its upper limit and can no longer track the phase of the PCC voltage. Synchronization is lost and the output power oscillates. This loss of synchronization can be prevented by adjusting PLL parameters to balance overshoot and settling time of the PLL’s response.

2. Simulation results suggest that avoiding vulnerable operating rotor speed or decreasing the integration gain of PLL in case of grid side short circuit fault will potentially increase the stability of wind turbine.

Chapter 6

Conclusions, Contributions, and Recommendation for Future Work

This thesis has introduced a novel aggregation method based on state-space equations. The proposed aggregation method benefits from applying different wind speeds as the system input for each wind turbine that can be very useful for considering wind variation within a wind farm. Generally, detailed simulations that represent electromagnetic effects in the power grid are time-consuming, especially when dealing with networks with a large number of generators. In the future, bigger wind farms are expected to consist of numerous wind turbines that will lead to very large simulation times if each turbine is to be modeled separately. This problem can be solved by the use of the proposed aggregation techniques that can reduce the complexity of a wind farm model while maintaining an acceptable level of accuracy.

6.1 Main Contributions of the Thesis

This thesis has contributed to the development of a new aggregation method maintaining collective behavior of DFIG wind turbines in a wind farm. The performance of the proposed model is examined under different operating conditions, various input wind speed, and turbines with different parameters. It is validated against detailed wind turbines modeled in EMT-based software.

6.1.1 Improved Aggregation Technique

The aggregation is achieved by recursively combining two structurally complete DFIG state space representations at a time and equivalencing this to the state space representation of a single DFIG ensuring that both have identical steady state responses. The parameters and incident wind speeds can be different for each DFIG in the aggregate. The features of the aggregated model are:

(1) It preserves the same block structure, i.e., the same outputs (injecting currents) and inputs (prime mover torque) and exactly matches the combined steady state outputs, while still giving a sufficiently accurate transient response.

(2) The aggregated model can be implemented as a single DFIG in any EMT simulation software. It is interfaced to the external system using a modified transformer representation that reflects the current scaling to multiple machines. It does not require modification of existing models in the software, merely an appropriate selection of the parameters.

(3) The aggregated model retains the same major collective oscillation modes of the original cluster of DFIGs with the external network. However, the representation of inter-machine transients within the windfarm is sacrificed due to the aggregation.

(4) The simplification of the detailed model is important for off-line as well as real-time simulation. For off-line simulation, it provides a significant speedup. For real-time

simulation, it could result in savings in hardware, because more DFIGs in the model would require harnessing more computing cores.

(5) It should be noted that the model is not intended for designing the wind turbine or generator. Rather it is an aggregated representation that permits the study of how the windfarm interacts with the external network, which is modelled on an EMT program. Example applications could involve performance under network faults, power supply into the network as affected by wake conditions and wind speed changes as was shown in Chapter 4. It could also be used for studying interplant oscillations when multi-machine cluster representation is used.

6.1.2 Considering Several Aggregate Models in More Complex Wind Farm Layouts

It was shown in Section 4.6 that for a wind farm with a more complex layout and different input wind speed for turbines, the behaviour could be better reproduced if the aggregate model contained several aggregated WTs as opposed to a single aggregated WT. The proposed aggregated model employing 3 machines demonstrates a very precise transient response, outperforming all other models. However, the proposed model representing the WF with 1 equivalent machine still provides a reasonable level of accuracy which can reduce the computational time compared to using 3-machine equivalent model.

6.1.3 Investigation of the Causes of Loss of Phase Locked Loop Synchronization Stability

The thesis identified that a root cause of loss of stability of the DFIG was the inability of the Phase Locked Loop (PLL) to stay in synchronism with the grid voltage. The thesis proposed a mathematical model of the PLL and DFIG for investigating this phenomenon. A new stability indicator index F_S is introduced to quantify the tendency of the DFIG to lose synchronism. The relative index F_S is proposed as an indicator of stability for DFIG's phase synchronizing and having lower F_S value for a DFIG means a greater stability margin.

A theoretical model of the grid synchronization mechanism of the DFIG is developed in the dq frame, which takes into account the system strength and phase locked loop (PLL) parameters. The approach starts out with a small signal model and assumes that it can be applied in a qualitive manner for large disturbances if the operating point change is treated in a quasi-steady state manner. This is an attempt to discuss the mechanism using techniques similar to analyzing large signal instability in synchronous machines, using a procedure similar in concept to the equal area criterion. Using the theoretical model in a simple example, the mechanism of synchronization loss is identified, and stability characteristics analyzed using a locus of the operating point.

The model reveals the mechanism of loss of synchronization during an ac voltage dip. It is shown that decreasing the rotor side converter PLL integration gain and changing rotor speed can help increase the stability degree. Below conclusions were made according to this study:

(1) During a voltage dip at the PCC, the output frequency of the PLL may reach its upper limit and can no longer track the phase of the PCC voltage and loses synchronization is lost. This loss of synchronization can be prevented by adjusting PLL gain to balance overshoot and settling time of the PLL's response.

(2) Calculation of the index F_S suggests that avoiding vulnerable operating rotor speed can results in a decrease in F_S, thereby reducing the likelihood of instability. Similarly decreasing the integration gain of PLL in case of grid side short circuit, reduces the overshoot of the PLL response VMQ and also helps in stabilization. EMT simulation confirmed that taking these measures did indeed improve stability.

6.2 Future Work

This research has laid the foundations for continuing this work in the following areas.

1) Applying the same aggregation procedure for other common wind turbine types such as the permanent magnet synchronous generator (PMSG) in order to cover different type of wind turbine in wind farms. To do so, ones need to consider differential algebraic equation for PMSG and implement the combination process to find the aggregate model recursively.
2) Implementing the proposed aggregation model for large wind farms having both DFIG and PMSG type wind generators and comparing results with the detailed model to evaluate the accuracy of the aggregated model for transient analysis.

3) Creating a user defined component in EMT software that can be used simply by any user and provide parameters for proposed aggregate model with having different wind speed and parameter of each turbine as an input to the component.
4) Considering stochastically changing behaviour of wind speed to find exact wind speed at each turbine at each moment and then modify the aggregation model in a way that it could be able to provide equivalent model using these continuously changing inputs.

6.3 Thesis Publications

The contributions from this thesis have led to the following publications.

- I. Kaffashan, W. Li, A. M. Gole, “The Loss of Synchronization Mechanism for Doubly-fed Induction Generator Integration to Weak Networks” (Accepted for 2024 IEEE Power & Energy Society General Meeting)
- W. Li, I. Kaffashan, A. M. Gole and Y. Zhang, "Structure Preserving Aggregation Method for Doubly-fed Induction Generators in Wind Power Conversion," in *IEEE Transactions on Energy Conversion*, doi: 10.1109/TEC.2021.3126571
- W. Li, A. M. Gole, M. K. Das, I. Kaffashan, “Research on Wind Farms Aggregation Method for Electromagnetic Simulation Based on FDNE”, *2019 IEEE PES Innovative Smart Grid Technologies Europe (ISGT-Europe)*, September 2019

Bibliography

[1] “Global wind report: annual market update,” 2019.

[2] Y. Song and F. Blaabjerg, “Overview of DFIG-Based Wind Power System Resonances under Weak Networks,” *IEEE Trans. Power Electron.*, vol. 32, no. 6, pp. 4370–4394, 2017.

[3] V. Yaramasu, B. Wu, P. C. Sen, S. Kouro, and M. Narimani, “High-power wind energy conversion systems: State-of-the-art and emerging technologies,” *Proc. IEEE*, vol. 103, no. 5, pp. 740–788, 2015.

[4] H. Nian, P. Cheng, and Z. Q. Zhu, “Independent operation of DFIG-based WECS using resonant feedback compensators under unbalanced grid voltage conditions,” *IEEE Trans. Power Electron.*, vol. 30, no. 7, pp. 3650–3661, 2015.

[5] A. Gonzalo Abad, Jesus Lopez, Miguel Rodriguez, Luis Marroyo and G. Iwanski, *Doubly Fed Induction Machine: Modeling and Control for Wind Energy Generation*. IEEE Press, 2011.

[6] R. R.-C. Edgar N. Sanchez, *Doubly Fed Induction Generators Control for Wind Energy*. CRC Press, 2016.

[7] K. Ma, L. Tutelea, I. Boldea, D. M. Ionel, and F. Blaabjerg, “Power Electronic Drives, Controls, and Electric Generators for Large Wind Turbines-An Overview,” *Electr. Power Components Syst.*, vol. 43, no. 12, pp. 1406–1421, 2015.

[8] R. Zhu, Z. Chen, Y. Tang, F. Deng, and X. Wu, “Dual-loop control strategy for DFIG-based wind turbines under grid voltage disturbances,” *IEEE Trans. Power Electron.*, vol. 31, no. 3, pp. 2239–2253, 2016.

[9] M. Yamamoto and O. Motoyoshi, “Active and reactive power control for doubly-fed wound rotor induction generator,” vol. 6, no. 4, pp. 624–629, 1991.

[10] H. R. Ali, L. P. Kunjumuhammed, B. C. Pal, A. G. Adamczyk, and K. Vershinin, “Model order reduction of wind farms: Linear approach,” *IEEE Trans. Sustain. Energy*, vol. 10, no. 3, pp. 1194–1205, 2019.

[11] W. R. J. Conroy, “Aggregate modelling of wind farms containing full-converter wind turbine generators with permanent magnet synchronous machines: transient stability studies,” *IET Renew. Power Gener.*, vol. 3, no. 1, pp. 1-39–52, 2009.

[12] R. J. T. Ahmed M. Gallai, “Coherency identification for large electric power systems,” *IEEE Trans. Circuit Syst.*, 1982.

[13] F. F. Wu and N. Narasimhamurthi, “Coherency Identification for Power System Dynamic Equivalents,” *IEEE Trans. Circuits Syst.*, vol. 30, no. 3, pp. 140–147, 1983.

[14] R. P. A. J. Germond, “Dynamic aggregation of generating unit models,” *IEEE Trans. Power App. Syst.*, no. 4, pp. 1060–1069, 1978.

[15] W. S. M. H. K. Lauw, “Universal machine modeling for the presentation of rotating electric machinery in an electromagnetic transients program,” *IEEE Trans. Power App. Syst.*, vol. PAS-101, pp. 1342–1352, 1982.

[16] J. G. Slootweg and W. L. Kling, “Aggregated modelling of wind parks in power system dynamics simulations,” *2003 IEEE Bol. PowerTech - Conf. Proc.*, vol. 3, pp. 626–631, 2003.

[17] M. Ali, I. Ilie, Milanovic Jovica, and G. Chicco, “Wind Farm Model Aggregation Using Probabilistic Clustering,” *IEEE Trans. Power Syst.*, vol. 28, no. 1, pp. 309–316, 2013.

[18] J. Zou, C. Peng, H. Xu, and Y. Yan, “A Fuzzy Clustering Algorithm-Based Dynamic Equivalent Modeling Method for Wind Farm with DFIG,” *IEEE Trans. Energy Convers.*, vol. 30, no. 4, pp. 1329–1337, 2015.

[19] E. Muljadi *et al.*, “Equivalencing the collector system of a large wind power plant,” *2006 IEEE Power Eng. Soc. Gen. Meet. PES*, 2006.

[20] J. Brochu, C. Larose, and R. Gagnon, “Validation of single- and multiple-machine equivalents for modeling wind power plants,” *IEEE Trans. Energy Convers.*, vol. 26, no. 2, pp. 532–541, 2011.

[21] E. Muljadi, S. Pasupulati, A. Ellis, and D. Kosterov, “Method of equivalencing for a large wind power plant with multiple turbine representation,”

IEEE Power Energy Soc. 2008 Gen. Meet. Convers. Deliv. Electr. Energy 21st Century, PES, vol. 3, 2008.

[22] L. M. Fernández, C. A. García, J. R. Saenz, and F. Jurado, "Equivalent models of wind farms by using aggregated wind turbines and equivalent winds," *Energy Convers. Manag.*, vol. 50, no. 3, pp. 691–704, 2009.

[23] L. P. Kunjumuhammed, B. C. Pal, C. Oates, and K. J. Dyke, "The Adequacy of the Present Practice in Dynamic Aggregated Modeling of Wind Farm Systems," *IEEE Trans. Sustain. Energy*, vol. 8, no. 1, pp. 23–32, 2017.

[24] D. E. Kim and M. A. El-Sharkawi, "Dynamic equivalent model of wind power plant using an aggregation technique," *IEEE Trans. Energy Convers.*, vol. 30, no. 4, pp. 1639–1649, 2015.

[25] M. Ali, J. Matevosyan, J. V Milanović, and L. Söder, "Effect of wake consideration on estimated cost of wind energy curtailments," *8th Int. Work. Large Scale Integr. Wind Power, Bremen*, no. October, pp. 14–15, 2009.

[26] T. Burton, *Wind Energy Handbook*. Chichester: John Wiley & Sons, Ltd, 2001.

[27] L. J. Vermeer, J. N. Sørensen, and A. Crespo, "Wind turbine wake aerodynamics," *Prog. Aerosp. Sci.*, vol. 39, no. 6–7, pp. 467–510, 2003.

[28] L. M. Fernández, F. Jurado, and J. R. Saenz, "Aggregated dynamic model for wind farms with doubly fed induction generator wind turbines," *Renew. Energy*, vol. 33, no. 1, pp. 129–140, 2008.

[29] P. Gardner, L. M. Craig, and G. J. Smith, "Electrical Systems for Offshore Wind Farms," *Switch Onto Wind Power 20th*, pp. 309–317, 1998.

[30] R. Shakoor, M. Y. Hassan, A. Raheem, and Y. K. Wu, "Wake effect modeling: A review of wind farm layout optimization using Jensen's model," *Renew. Sustain. Energy Rev.*, vol. 58, pp. 1048–1059, 2016.

[31] M. E. Bechly and P. D. Clausen, "Structural design of a composite wind turbine blade using finite element analysis," Comput. Struct., vol. 63, no. 3, pp. 639–646, 1997.

[32] J. F. Ainslie, “Journal of Wind Engineering and Industrial Aerodynamics, 27 (1988) 213-224,” *J. Wind Eng.*, vol. 27, no. 1–3, pp. 213–224, 1988.

[33] J. F. Wendt, *Computational Fluid Dynamics: An introduction (3rd edition)*. Springer-Verlag Berlin Heidelberg, 2009.

[34] N. O. Jensen, “A note on wind generator interaction,” *Risø-M-2411 Risø Natl. Lab. Roskilde*, pp. 1–16, 1983.

[35] J. N. O. Katic I., Højstrup J., “A Simple Model for Cluster Efficiency,” *Proc. Eur. Wind Energy Conf.*, vol. 1, 1987.

[36] “WAsP - the Wind Atlas Analysis and Application Program, ‘Wake effect model,’” 2010. [Online]. Available: http://www.wasp.dk/Products/WAsP/WakeEffectModel.html.

[37] “EMD International A/S, WindPRO”, 2009. [Online]. Available: http://www.emd.dk/WindPRO/Modules/.

[38] M. Ali, “Probabilistic Modelling Techniques and a Robust Design Methodology for Offshore Wind Farms,” 2012.

[39] F. González-Longatt, P. P. Wall, and V. Terzija, “Wake effect in wind farm performance: Steady-state and dynamic behavior,” *Renew. Energy*, vol. 39, no. 1, pp. 329–338, 2012.

[40] “Horns Rev Offshore Wind Farm.pdf”, [Online]. Available: https://www.solaripedia.com/files/283.pdf

[41] R. J. Barthelmie *et al.*, *Flow and wakes in large wind farms : Risø-R-Report*, no. November 2015. 2011.

[42] WECC, “WECC Wind Plant Dynamic Modeling Guidelines,” vol. 2010, no. November 2010, pp. 1–14, 2014.

[43] S. K. Bin Wu, Yongqiang Lang, Navid Zargari, *Power conversion and Control of Wind Energy Systems*. IEEE Press.

[44] S. D. S. Paul C. Krause, Oleg Wasynczuk, *Analysis of Electric Machinery and Drive Systems*. IEEE Press.

[45] R. Pena, J. C. Clare, and G. M. Asher, “Doubly fed induction generator using back-to-back PWM converters and its application to variablespeed wind-energy generation,” *IEE Proc. Electr. Power Appl.*, vol. 143, no. 3, pp. 231–241, 1996.

[46] H. Nikkhajoei and R. Iravani, “Dynamic model and control of AC-DC-AC voltage-sourced converter system for distributed resources,” *IEEE Trans. Power Deliv.*, vol. 22, no. 2, pp. 1169–1178, 2007.

[47] Panos M. Pardalos, S. Rebennack, M. V. F. Pereira, N. A. Iliadis, V. Pappu. Handbooks of Wind Power Systems. Springer Press, 2013.

[48] H. Nikkhajoei, A. Tabesh, and R. Iravani, “Dynamic model of a matrix converter for controller design and system studies,” *IEEE Trans. Power Deliv.*, vol. 21, no. 2, pp. 744–754, 2006.

[49] M. Aoki, “Control of Large-Scale Dynamic Systems by Aggregation,” *IEEE TRANISACTIONS Autom. Control*, 1968.

[50] M. A. Chowdhury, N. Hosseinzadeh, M. M. Billah, and S. A. Haque, “Dynamic DFIG wind farm model with an aggregation technique,” *ICECE 2010 - 6th Int. Conf. Electr. Comput. Eng.*, no. December, pp. 330–333, 2010.

[51] W. Li, I. Kaffashan, A. M. Gole and Y. Zhang, "Structure Preserving Aggregation Method for Doubly-Fed Induction Generators in Wind Power Conversion," in IEEE Transactions on Energy Conversion, vol. 37, no. 2, pp. 935-946, June 2022, doi: 10.1109/TEC.2021.3126571.

[52] W. Li, A. M. Gole, M. K. Das and I. Kaffashan, "Research on Wind Farms Aggregation Method for Electromagnetic Simulation Based on FDNE," 2019 IEEE PES Innovative Smart Grid Technologies Europe (ISGT-Europe), 2019, pp. 1-5, doi: 10.1109/ISGTEurope.2019.8905666.

[53] D. A. Woodford, A. M. Gole and R. W. Menzies, "Digital Simulation of DC Links and AC Machines," *IEEE Trans. Power Apparatus and Systems*, vol. PAS-102, no. 6, pp. 1616-1623, June 1983.

[54] Bruce C. Moore, “Principal component analysis in linear systems: controllability, observability, and model reduction,” IEEE Trans. Automatic Control, vol. AC-26, no. 1, pp. 17-32, Feb. 1981.

[55] Masanao Aoki. “Control of large-scale dynamic systems by aggregation,” IEEE Trans. Automatic Control, vol. AC-13, no.3, pp. 246-253, June 1968.

[56] A. Y. Goharrizi, J. C. Garcia Alonso, E. Borisova, F. Mosallat and D. Muthumuni, "Benchmark Model of Type-III Wind Turbine for Research and Development Applications," 2018 IEEE Canadian Conference on Electrical & Computer Engineering (CCECE), Quebec City, QC, 2018, pp. 1-6.

[57] O. Abdel-Baqi and A. Nasiri, "A Dynamic LVRT Solution for Doubly Fed Induction Generators," in IEEE Transactions on Power Electronics, vol. 25, no. 1, pp. 193-196, Jan. 2010, doi: 10.1109/TPEL.2009.2026578.

[58] J. Z. Zhou, H. Ding, S. Fan, Y. Zhang and A. M. Gole, "Impact of Short-Circuit Ratio and Phase-Locked-Loop Parameters on the Small-Signal Behavior of a VSC-HVDC Converter," in IEEE Transactions on Power Delivery, vol. 29, no. 5, pp. 2287-2296, Oct. 2014.

[59] H. Konishi, C. Takahashi, H. Kishibe, and H. Sato, “A consideration of stable operating power limits in VSC-HVDC systems,” presented at the 7th Int. Conf. AC-DC Power Transm., London, U.K., 2001.

[60] L. Zhang, L. Harnefors, and H.-P. Nee, “Interconnection of two very weak AC systems by VSC-HVDC links using power-synchronization control,” IEEE Trans. Power Syst., vol. 26, no. 1, pp. 344–355, Feb. 2011.

[61] L. Fan and Z. Miao, "Wind in Weak Grids: 4 Hz or 30 Hz Oscillations?," in IEEE Transactions on Power Systems, vol. 33, no. 5, pp. 5803-5804, Sept. 2018.

[62] L. Fan, "Modeling Type-4 Wind in Weak Grids," in IEEE Transactions on Sustainable Energy, vol. 10, no. 2, pp. 853-864, April 2019.

[63] D. Zhang, Y. Wang, J. Hu, S. Ma, Q. He and Q. Guo, "Impacts of PLL on the DFIG-based WTG's electromechanical response under transient conditions: analysis and modeling," in CSEE Journal of Power and Energy Systems, vol. 2, no. 2, pp. 30-39, June 2016.

[64] K. Narendra et al., "New microprocessor based relay to monitor and protect power systems against sub-harmonics," 2011 IEEE Electrical Power and Energy Conference, 2011, pp. 438-443.

[65] I. Hr, R. J. Best and D. J. Morrow, "Inter-area power oscillation frequency mode with wind turbine generator in Irish power system using PMU data," 2013 48th International Universities' Power Engineering Conference (UPEC), 2013, pp. 1-5.

[66] Ö. Göksu, R. Teodorescu, C. L. Bak, F. Iov and P. C. Kjær, "Instability of Wind Turbine Converters During Current Injection to Low Voltage Grid Faults and PLL Frequency Based Stability Solution," in IEEE Transactions on Power Systems, vol. 29, no. 4, pp. 1683-1691, July 2014.

[67] J. Hu, Q. Hu, B. Wang, H. Tang and Y. Chi, "Small Signal Instability of PLL-Synchronized Type-4 Wind Turbines Connected to High-Impedance AC Grid During LVRT," in IEEE Transactions on Energy Conversion, vol. 31, no. 4, pp. 1676-1687, Dec. 2016.

[68] J. Hu, Y. Huang, D. Wang, H. Yuan and X. Yuan, "Modeling of Grid-Connected DFIG-Based Wind Turbines for DC-Link Voltage Stability Analysis," in IEEE Transactions on Sustainable Energy, vol. 6, no. 4, pp. 1325-1336, Oct. 2015.

[69] J. Liu et al., "Impact of Power Grid Strength and PLL Parameters on Stability of Grid-Connected DFIG Wind Farm," in IEEE Transactions on Sustainable Energy, vol. 11, no. 1, pp. 545-557, Jan. 2020.

[70] P. Rodríguez, A. Luna, I. Candela, R. Mujal, R. Teodorescu and F. Blaabjerg, "Multiresonant Frequency-Locked Loop for Grid Synchronization of Power Converters Under Distorted Grid Conditions," in IEEE Transactions on Industrial Electronics, vol. 58, no. 1, pp. 127-138, Jan. 2011.

[71] Z. Miao, "Impedance-Model-Based SSR Analysis for Type 3 Wind Generator and Series-Compensated Network," in IEEE Transactions on Energy Conversion, vol. 27, no. 4, pp. 984-991, Dec. 2012.

[72] D. Jovcic, "Phase locked loop system for FACTS," in IEEE Transactions on Power Systems, vol. 18, no. 3, pp. 1116-1124, Aug. 2003.

[73] D. Dong, J. Li, D. Boroyevich, P. Mattavelli, I. Cvetkovic and Y. Xue, "Frequency behavior and its stability of grid-interface converter in distributed

generation systems," 2012 Twenty-Seventh Annual IEEE Applied Power Electronics Conference and Exposition (APEC), 2012, pp. 1887-1893.

[74] Y. Song and F. Blaabjerg, "Overview of DFIG-Based Wind Power System Resonances Under Weak Networks," in IEEE Transactions on Power Electronics, vol. 32, no. 6, pp. 4370-4394, June 2017.

[75] L. Piyasinghe, Z. Miao, J. Khazaei and L. Fan, "Impedance Model-Based SSR Analysis for TCSC Compensated Type-3 Wind Energy Delivery Systems," in IEEE Transactions on Sustainable Energy, vol. 6, no. 1, pp. 179-187, Jan. 2015.

[76] M. Ali, "Probabilistic Modelling Techniques And A Robust Design Methodology For Offshore Wind Farms", PhD Thesis, University of Manchester, 2012.

[77] A. M. S. Al-bayati, F. Mancilla-David and J. L. Domínguez-Garcíal, "Aggregated models of wind farms: Current methods and future trends," 2016 North American Power Symposium (NAPS), Denver, CO, USA, 2016, pp. 1-6, doi: 10.1109/NAPS.2016.7747954.

[78] Technical Specification, "Type 3 Wind Turbine Model (PSCAD v4.6)", Manitoba Hydro International, Revision 3, 2018.

[79] A. Gole, V. K. Sood, and L. Mootoosamy, "Validation and analysisof a grid control system using D-Q-Z transformation for static compensator systems," in Proc. Can. Conf. Elect. Comput. Eng., Montreal,QC, Canada, Sep. 1989, pp. 745-748.

[80] S. Golestan, M. Monfared and F. D. Freijedo, "Design-Oriented Study of Advanced Synchronous Reference Frame Phase-Locked Loops," in IEEE Transactions on Power Electronics, vol. 28, no. 2, pp. 765-778, Feb. 2013, doi: 10.1109/TPEL.2012.2204276.

[81] A. P. Gupta, A. Mitra, A. Mohapatra and S. N. Singh, "A Multi-Machine Equivalent Model of a Wind Farm Considering LVRT Characteristic and Wake Effect," in IEEE Transactions on Sustainable Energy, vol. 13, no. 3, pp. 1396-1407, July 2022, doi: 10.1109/TSTE.2022.3159307.

[82] M. Liu, W. Pan, Y. Zhang, K. Zhao, S. Zhang, and T. Liu, “A dynamic equivalent model for DFIG-based wind farms,” IEEE Access, vol. 7, pp. 74 931–74 940, 2019.

[83] P. Wang, Z. Zhang, Q. Huang, N. Wang, X. Zhang, and W.-J. Lee, “Improved wind farm aggregated modeling method for large-scale power system stability studies,” IEEE Trans. Power Syst., vol. 33, no. 6, pp. 6332–6342, Nov. 2018.

[84] Y. Jin, D. Wu, P. Ju, C. Rehtanz, F. Wu, and X. Pan, “Modeling of wind speeds inside a wind farm with application to wind farm aggregate modeling onsidering LVRT characteristic,” IEEE Trans. Energy Convers., vol. 35, no. 1, pp. 508–519, Mar. 2020.

[85] P. Chao, W. Li, X. Liang, S. Xu, and Y. Shuai, “An analytical two-machine equivalentmethod ofDFIG-basedwind power plants considering complete FRT processes,” IEEE Trans. Power Syst., vol. 36, no. 4, pp. 3657–3667, Jul. 2021.

[86] B. Hoseinzadeh, M. H. Amini, K. G. Boroojeni and C. L. Bak, "RTDS Demonstration of Harmonic Amplification in Under Sea/Ground Cables of Offshore Wind Farms," 2018 IEEE International Conference on Environment and Electrical Engineering and 2018 IEEE Industrial and Commercial Power Systems Europe (EEEIC / I&CPS Europe), Palermo, Italy, 2018, pp. 1-5, doi: 10.1109/EEEIC.2018.8494343.